



NAVAL POSTGRADUATE SCHOOL

MONTEREY, CALIFORNIA

THESIS

**PRESSURE DISTRIBUTION AND PERFORMANCE
IMPACTS OF AEROSPIKE NOZZLES ON ROTATING
DETONATION ENGINES**

by

Mark C. Schnabel

June 2017

Thesis Advisor:
Second Reader:

Christopher M. Brophy
David F. Dausen

Approved for public release. Distribution is unlimited.

THIS PAGE INTENTIONALLY LEFT BLANK

REPORT DOCUMENTATION PAGE			<i>Form Approved OMB No. 0704-0188</i>	
Public reporting burden for this collection of information is estimated to average 1 hour per response, including the time for reviewing instruction, searching existing data sources, gathering and maintaining the data needed, and completing and reviewing the collection of information. Send comments regarding this burden estimate or any other aspect of this collection of information, including suggestions for reducing this burden, to Washington headquarters Services, Directorate for Information Operations and Reports, 1215 Jefferson Davis Highway, Suite 1204, Arlington, VA 22202-4302, and to the Office of Management and Budget, Paperwork Reduction Project (0704-0188) W, DC 20503.				
1. AGENCY USE ONLY		2. REPORT DATE June 2017	3. REPORT TYPE AND DATES COVERED Master's thesis	
4. TITLE AND SUBTITLE PRESSURE DISTRIBUTION AND PERFORMANCE IMPACTS OF AEROSPIKE NOZZLES ON ROTATING DETONATION ENGINES			5. FUNDING NUMBERS	
6. AUTHOR(S) Mark C. Schnabel				
7. PERFORMING ORGANIZATION NAME(S) AND ADDRESS(ES) Naval Postgraduate School Monterey, CA 93943-5000			8. PERFORMING ORGANIZATION REPORT NUMBER	
9. SPONSORING / MONITORING AGENCY NAME(S) AND ADDRESS(ES) N/A			10. SPONSORING / MONITORING AGENCY REPORT NUMBER	
11. SUPPLEMENTARY NOTES The views expressed in this thesis are those of the author and do not reflect the official policy or position of the Department of Defense or the U.S. Government. IRB number ____N/A____.				
12a. DISTRIBUTION / AVAILABILITY STATEMENT Approved for public release. Distribution is unlimited.			12b. DISTRIBUTION CODE	
13. ABSTRACT (maximum 200 words) <p>Rotating detonation engines (RDEs) have the potential to further increase the performance of air-breathing propulsion devices and are currently being explored as an option for missions with wide altitude and flight Mach number ranges. Aerospike nozzles lend themselves well to this type of application because they possess altitude-compensating characteristics. However, the effects of the unsteady nozzle inlet dynamics associated with RDEs on aerospike nozzle performance have not been fully determined. Consequently, aerospike nozzle design has not yet been optimized for RDE applications.</p> <p>A contoured aerospike nozzle was designed for implementation on a RDE to examine the effect of ideal aerospike profiles on RDE performance. Currently, no nozzle design technique accounts for transient throat conditions inherent in RDE operation. Therefore, the nozzle contour was designed using a traditional, steady-state design methodology at both on- and off-design conditions anticipated throughout the combustion cycle. Steady-state, non-reacting computational fluid dynamics (CFD) simulations were performed on various nozzle geometries over multiple pressure ratios to investigate the flow field structure along the nozzle contour and justify design tradeoffs. Future work is needed to implement this nozzle design to investigate the effect of RDE-specific flow fields on nozzle performance.</p>				
14. SUBJECT TERMS rotating detonation engine, continuous detonation engine, pressure gain combustion, aerospike nozzle, plug nozzle, computational fluid dynamics			15. NUMBER OF PAGES 127	
			16. PRICE CODE	
17. SECURITY CLASSIFICATION OF REPORT Unclassified	18. SECURITY CLASSIFICATION OF THIS PAGE Unclassified	19. SECURITY CLASSIFICATION OF ABSTRACT Unclassified	20. LIMITATION OF ABSTRACT UU	

THIS PAGE INTENTIONALLY LEFT BLANK

Approved for public release. Distribution is unlimited.

**PRESSURE DISTRIBUTION AND PERFORMANCE IMPACTS OF
AEROSPIKE NOZZLES ON ROTATING DETONATION ENGINES**

Mark C. Schnabel
Ensign, United States Navy
B.S., United States Naval Academy, 2016

Submitted in partial fulfillment of the
requirements for the degree of

MASTER OF SCIENCE IN MECHANICAL ENGINEERING

from the

**NAVAL POSTGRADUATE SCHOOL
June 2017**

Approved by: Christopher M. Brophy
Thesis Advisor

David F. Dausen
Second Reader

Garth V. Hobson
Chair, Department of Mechanical and Aerospace Engineering

THIS PAGE INTENTIONALLY LEFT BLANK

ABSTRACT

Rotating detonation engines (RDEs) have the potential to further increase the performance of air-breathing propulsion devices and are currently being explored as an option for missions with wide altitude and flight Mach number ranges. Aerospike nozzles lend themselves well to this type of application because they possess altitude-compensating characteristics. However, the effects of the unsteady nozzle inlet dynamics associated with RDEs on aerospike nozzle performance have not been fully determined. Consequently, aerospike nozzle design has not yet been optimized for RDE applications.

A contoured aerospike nozzle was designed for implementation on a RDE to examine the effect of ideal aerospike profiles on RDE performance. Currently, no nozzle design technique accounts for transient throat conditions inherent in RDE operation. Therefore, the nozzle contour was designed using a traditional, steady-state design methodology at both on- and off-design conditions anticipated throughout the combustion cycle. Steady-state, non-reacting computational fluid dynamics (CFD) simulations were performed on various nozzle geometries over multiple pressure ratios to investigate the flow field structure along the nozzle contour and justify design tradeoffs. Future work is needed to implement this nozzle design to investigate the effect of RDE-specific flow fields on nozzle performance.

THIS PAGE INTENTIONALLY LEFT BLANK

TABLE OF CONTENTS

I.	INTRODUCTION.....	1
A.	OVERVIEW.....	1
B.	MOTIVATION.....	4
C.	OBJECTIVES AND APPROACH.....	4
II.	BACKGROUND.....	7
A.	THRUST.....	7
B.	NOZZLES.....	10
1.	Basic Design.....	10
2.	Shortcomings of Conventional Nozzles.....	10
3.	Altitude Compensation: An Alternative to Conventional Nozzles.....	13
C.	INTRODUCTION TO AEROSPIKE NOZZLES.....	14
D.	CLASSIFICATION OF AEROSPIKE NOZZLES.....	16
1.	Annular Aerospike Nozzles.....	16
2.	Linear Aerospike Nozzles.....	18
3.	Truncation of Aerospike Nozzles.....	19
E.	FLOW PHYSICS OF PLUG NOZZLES.....	20
1.	Flow Features in Quiescent Air.....	21
2.	Flow Features in a Supersonic Free Stream.....	25
F.	FLOW PHYSICS OF THE NOZZLE BASE.....	27
1.	The Open Wake Regime.....	27
2.	The Closed Wake Regime.....	28
3.	Open/Closed Transition.....	28
4.	Base Pressure Prediction.....	32
III.	NOZZLE DESIGN METHOD.....	35
A.	INTRODUCTION.....	35
B.	DESIGN APPROACH: THE SIMPLE APPROXIMATE METHOD.....	36
C.	DERIVATION.....	37
IV.	NOZZLE DESIGN FOR THE RDE.....	43
A.	NOZZLE DESIGN ASSUMPTIONS.....	43
1.	Assumption of Purely Axial Flow.....	43
2.	Nonuniform Throat Conditions.....	44
3.	Expected Pressure Ratio.....	46

4.	Ideal Design Pressure Ratio	47
B.	APPLICATION TO THE CURRENT RDE	48
1.	Determination of Input Parameters	48
2.	Computed Results	49
C.	SOLIDWORKS DESIGN	53
V.	CFD ANALYSIS	57
A.	OVERVIEW	57
B.	FLUID DOMAIN	57
C.	COMPUTATIONAL MESH PARAMETERS	58
1.	Common Mesh Settings	59
2.	Face Sizing and Meshing	60
D.	CFD ASSUMPTIONS	61
1.	Non-Reacting Flow Modeled as Combustion Products	61
2.	Uniform Inlet Flow in the Radial and Circumferential Directions	63
E.	SOLVER DEFINITION AND BOUNDARY CONDITIONS	64
F.	TEST MATRIX	68
VI.	CFD RESULTS	69
A.	QUIESCENT AIR	69
1.	Nondimensional Wall Distance and Turbulence Modeling	69
2.	Validation of the Experimental Nozzle Design	70
3.	Steady-State Pressure Distribution along the Aerospike	72
4.	Steady-State Base Pressure Distribution	74
5.	Steady-State Thrust Computation	75
6.	Steady-State Thrust Coefficient	79
B.	SUPERSONIC FREE-STREAM	81
C.	MESH SENSITIVITY AND TURBULENCE MODELING	83
VII.	SUMMARY	85
A.	DESIGN GUIDELINES	85
B.	FUTURE WORK	85
APPENDIX A. MATLAB CODE		87
APPENDIX B. CEA DETONATION ANALYSIS		91
APPENDIX C. TRANSITION PRESSURE RATIO ANALYSIS		95

APPENDIX D. CEA DEFLAGRATION ANALYSIS.....	97
LIST OF REFERENCES.....	101
INITIAL DISTRIBUTION LIST	105

THIS PAGE INTENTIONALLY LEFT BLANK

LIST OF FIGURES

Figure 1.	Numerical Simulation of a Generic RDE. Source: [1].	2
Figure 2.	Unrolled Numerical Simulation of a Hydrogen-Air RDE. Source: [2].	3
Figure 3.	Engine Diagram—Exploded View. Source: [1].	5
Figure 4.	Pressure Distribution on a Simplified Rocket Casing. Adapted from [11].	7
Figure 5.	Internal Total Pressure and Thrust Distribution in a Turbojet Engine. Adapted from [11].	8
Figure 6.	Well-Prescribed Control Volume for a Simplified Rocket Geometry. Source: [11].	9
Figure 7.	Nozzle Configurations. Source: [14].	11
Figure 8.	Bell Nozzle Exhaust Plume Comparison. Adapted from [14].	13
Figure 9.	Annular Aerospike Nozzle. Source: [18].	14
Figure 10.	Aerospike Exhaust Plume Comparison. Adapted from [14].	15
Figure 11.	Completely External Aerospike. Adapted from [20].	16
Figure 12.	Internal-External Aerospike. Adapted from [20].	17
Figure 13.	Completely Internal Aerospike. Adapted from [20].	17
Figure 14.	Alternate Combustion Chamber Arrangement. Source: [24].	18
Figure 15.	Linear Aerospike Nozzle. Source: [26].	19
Figure 16.	Aerospike Terminology. Adapted from: [27].	21
Figure 17.	Flow Features of a Plug Nozzle. Adapted from [29].	22
Figure 18.	Mach Isolines and Jet Boundary in a Linear Full-Length Plug. Source: [27].	24
Figure 19.	Plug Nozzle Flow Field at Various Jet Pressures. Adapted from [15].	25

Figure 20.	Schematic View of the Interaction Between Exhaust and External Supersonic Jets Behind the Primary Nozzle External Shroud. Source: [27].	26
Figure 21.	Schematic View of Closed Wake Operation. Source: [37].	29
Figure 22.	Closed-Open Wake Transition. Source: [37].	29
Figure 23.	Schematic of Characteristic Lines at Closed-Open Wake Transition. Source: [37].	30
Figure 24.	Expansion Characteristic Lines	36
Figure 25.	Throat Angle Orientation with Respect to Contour Geometry	37
Figure 26.	Local Characteristic Line Geometry	38
Figure 27.	Approximate Method Contour Geometry	39
Figure 28.	Inlet (Solid) and Outlet (Dashed) Velocities as a Function of Azimuthal Location for a Generic RDE Simulation. Source: [49].	44
Figure 29.	Inlet (Solid) and Outlet (Dashed) Pressures and Temperatures as a Function of Azimuthal Location for a Generic RDE Simulation. Source: [49].	45
Figure 30.	Expected Nonuniform Throat Conditions	46
Figure 31.	Aerospike Contour for $PR_{\text{design}} = 10:1$	50
Figure 32.	Cowl Contour for $PR_{\text{design}} = 10:1$	50
Figure 33.	Spike and Cowl Configuration for $PR_{\text{design}} = 10:1$	51
Figure 34.	Spike and Cowl Configuration for $PR_{\text{design}} = 25:1$	52
Figure 35.	Spike and Cowl Configuration for $PR_{\text{design}} = 40:1$	52
Figure 36.	Aerospike SolidWorks Model	53
Figure 37.	Cowl SolidWorks Model	54
Figure 38.	Center Body SolidWorks Model	54
Figure 39.	Integration with Current RDE Hardware	55
Figure 40.	Experimental Fluid Domain Geometry for $PR_{\text{design}} = 10:1$	58

Figure 41.	ANSYS Domain Mesh for $PR_{\text{design}} = 10:1$	60
Figure 42.	Variability of Properties with Ratio of Specific Heats. Source: [10].	62
Figure 43.	Boundary Conditions for the $PR_{\text{design}} = 10:1$ Case.....	64
Figure 44.	Mach Number Distribution along the Nozzle Exit Plane at Various Pressure Ratios for the Quiescent Air Hydrogen Fuel Case, $PR_{\text{design}} = 10:1$	71
Figure 45.	Steady-State Nozzle Pressure Distribution at Various Pressure Ratios for the Quiescent Air Hydrogen Fuel Case, $PR_{\text{design}} = 10:1$	72
Figure 46.	Steady-State Nozzle Pressure Distribution at Various Pressure Ratios for the Quiescent Air Hydrogen Fuel Case, $PR_{\text{design}} = 25:1$	73
Figure 47.	Steady-State Nozzle Pressure Distribution at Various Pressure Ratios for the Quiescent Air Hydrogen Fuel Case, $PR_{\text{design}} = 40:1$	74
Figure 48.	Steady-State Base Pressure Distribution at Various Pressure Ratios for the Quiescent Air Hydrogen Fuel Case, $PR_{\text{design}} = 10:1$	75
Figure 49.	Designation of the RDE Control Volume	76
Figure 50.	Control Surfaces Over Which ANSYS Force Function Was Applied in the X-Direction, $PR_{\text{design}} = 10:1$	77
Figure 51.	Thrust Contribution for Control Surfaces 1, 2, and 6 for the Quiescent Air Hydrogen and Ethylene Fuel Cases, $PR_{\text{design}} = 10:1$	78
Figure 52.	Gross Thrust vs Pressure Ratio for H_2 Fuel Case	79
Figure 53.	Thrust Coefficient vs Pressure Ratio for H_2 Fuel Case.....	80
Figure 54.	Plot of Mach Numbers for Supersonic Free-Stream Case, No Base Bleed	81
Figure 55.	Mach Number Distribution along the Nozzle Exit Plane at Various Pressure Ratios for the Supersonic Free-Stream Hydrogen-Air Case	82
Figure 56.	Steady-State Nozzle Pressure Distribution at Various Pressure Ratios for the Supersonic Free-Stream Hydrogen-Air Case, $PR_{\text{design}} = 10:1$	82
Figure 57.	Effect of Base Bleed on Base Pressure Distribution, $PR_{\text{design}} = 10:1$, H_2 Fuel Case	83
Figure 58.	Mesh Sensitivity and Turbulence Model Analysis	84

THIS PAGE INTENTIONALLY LEFT BLANK

LIST OF TABLES

Table 1.	Input Parameters and Calculated Transition Pressure Ratio.....	49
Table 2.	Common Mesh Settings.....	59
Table 3.	CEA Results and ANSYS Approximations.....	63
Table 4.	Solver Parameters	65
Table 5.	Test Matrix.....	68

THIS PAGE INTENTIONALLY LEFT BLANK

LIST OF ACRONYMS AND ABBREVIATIONS

CAD	computer aided design
CEA	chemical equilibrium with applications code
CFD	computational fluid dynamics
CTAP	continuous tube average pressure
Isp	specific impulse [sec]
MOC	method of characteristics
NPS	Naval Postgraduate School
NRL	Naval Research Laboratory
ODWE	oblique detonation wave engine
PDE	pulsed detonation engine
PGC	pressure gain combustion
PR	pressure ratio
RDE	rotating detonation engine
RPCL	rocket propulsion and combustion laboratory
SST	shear stress transport
SSTO	single stage to orbit
TVC	thrust vector control

THIS PAGE INTENTIONALLY LEFT BLANK

ACKNOWLEDGMENTS

I would like to thank Dr. Chris Brophy for providing me the opportunity to perform this research at the rocket lab and for his continuous support and guidance throughout the year.

Thank you to Dave Dausen, Robert Wright, Andrew Chaves, Lee VanHoutte, and Captain Kai Grohe for assisting me in my research this year. You truly made my experience at NPS a memorable one.

Lastly, thank you to my family and friends, especially Mom, Dad, Matt, Ryan, and Mike. Your support and encouragement mean the world to me and helped me get to where I am today.

THIS PAGE INTENTIONALLY LEFT BLANK

I. INTRODUCTION

A. OVERVIEW

Long-range Navy aircraft and missiles are heavily dependent on gas turbine engines for propulsion. The prospect that power requirements and range of these systems are expected to increase over time, coupled with today's rising fuel costs and national budget constraints, have spurred engineers to focus on improving the specific fuel consumption of these engines. One technology that promises improvements over gas turbine engines in terms of thermodynamic efficiency is pressure gain combustion (PGC).

Detonation-based combustion is a type of PGC that offers better performance than traditional constant-pressure, or deflagration-based, combustion systems. Classic deflagration-based Brayton cycle engines are asymptotically approaching maximum combustion efficiency [1] by relying on advanced and costly multistage compressors to increase atmospheric air pressure. On the other hand, detonations naturally generate higher pressures across the combustion wave, resulting in a lower entropy rise for the same amount of heat addition and, subsequently, more available work at the same fuel cost. This eliminates or at least minimizes the need for compressors to generate increasingly higher pressures required by the engine to further improve efficiency [2]. Detonation-based combustion systems have been found to yield theoretical efficiency gains between 20% and 30% over traditional deflagration-based cycles [2], [3].

Pulsed detonation engines (PDEs) became the first practical, experimentally-tested detonation engines in the 1990s [1], [4]. A PDE contains a tube-shaped combustion chamber in which reactants are cyclically filled and detonated 20–100 times per second to produce thrust [5]. While they operate with the thermodynamic advantage of detonation-based combustion, PDEs were plagued by engineering challenges involving practical valving, adequate thermal management, and inherently intermittent thrust profiles [1], [6].

By the late 2000s, the fundamental shortcomings of PDEs had shifted focus toward an alternative form of detonation wave combustion known as the rotating

detonation engine (RDE). A conventional RDE consists of an annular combustion chamber created by two concentric cylindrical bodies [6]. An unreacted, detonable mixture is injected at the forward-end of the chamber and a detonation wave propagates circumferentially around the combustion chamber as it consumes the reactants [6]. The chamber geometry forces the products to expand axially through the aft-end of the chamber, as shown in Figure 1. The products can be further expanded by a nozzle to produce thrust or directed through turbomachinery for power generation.

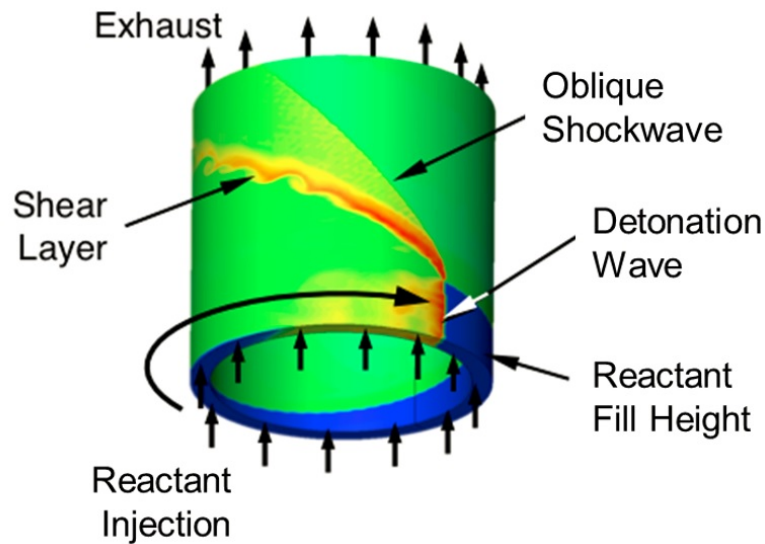
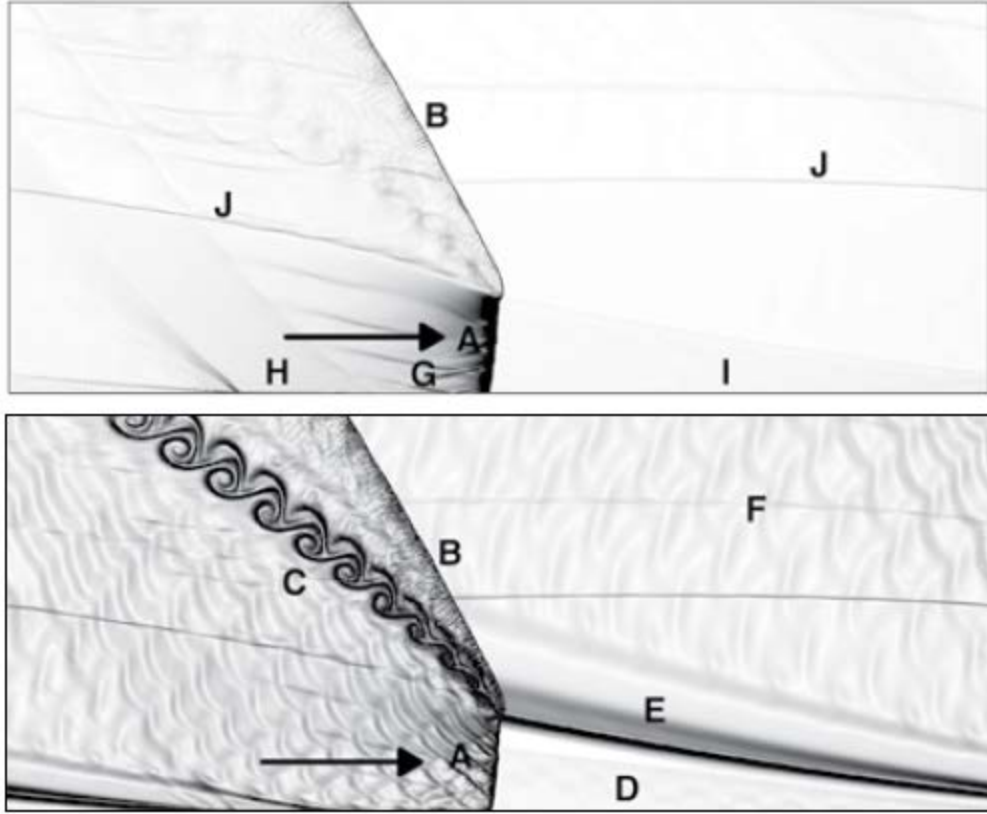


Figure 1. Numerical Simulation of a Generic RDE. Source: [1].

The Naval Research Laboratory conducted simulations of an RDE that showed a strong resemblance between RDE performance and ideal detonation cycle performance [2]. Figure 2 shows temperature and pressure gradient solutions of an “unrolled” hydrogen-air RDE to illustrate finer details of the flow field.



“Temperature (top) and pressure (bottom) gradient solution of an ‘unrolled’ hydrogen-air RDE solution, showing different relevant features of the flow. A) detonation wave, B) trailing edge shock wave, C) slip line between freshly detonated products and older products, D) fill region, E) nondetonated burned gas region, F) expansion region with detonated products, G) inlet region with blocked injector micro-nozzles, H) inlet region with partial filling micro-nozzles, I) inlet region with choked micro-nozzles, and J) secondary shock wave. Detonation wave moves azimuthally from left to right” [2].

Figure 2. Unrolled Numerical Simulation of a Hydrogen-Air RDE. Source: [2].

Unlike in a PDE, the detonation must only be initiated once and will continue to propagate assuming a detonable mixture is continually supplied [6]. RDEs yield more desirable thrust profiles and higher thrust densities than PDEs. Additionally, their thrust profiles closely resemble steady-state combustion because of the circumferential direction of detonation and high frequency operation, typically on the order of 1–20 kHz [1]. However, prototype RDEs have yet to achieve theoretical performance gains [6], [7], [8], [9]. Many technical challenges remain before RDEs can be practically implemented, such as low total pressure loss injection schemes and interfacing with turbomachinery.

B. MOTIVATION

RDEs have the potential to further increase the performance of air-breathing propulsion devices, and are currently being explored as an option for missions with wide flight Mach number and altitude ranges. Aerospike nozzles lend themselves well to this type of application because they possess altitude-compensating characteristics. However, the effects of the time-variant flow fields associated with RDEs on aerospike nozzle performance have not been fully determined. Consequently, aerospike nozzle design has not yet been optimized for RDE applications.

By optimizing aerospike nozzle design for RDE use, net performance of RDEs in terms of specific impulse (Isp) will be increased by the efficient acceleration of high-pressure combustion products to supersonic velocities. This is applicable to the interests of the Department of Defense because an increase in specific impulse will have a direct effect on aircraft range and efficiency.

C. OBJECTIVES AND APPROACH

The Naval Postgraduate School (NPS) Rocket Propulsion and Combustion Laboratory (RPCL) has been developing an RDE over the course of several years. This RDE currently possesses a nozzle design that was not optimized for thrust [6]. Rather, it was designed as a back pressurization device that offers control over combustion dynamics. The current configuration is simply a converging-diverging aerospike nozzle with a subsonic area ratio of 1.34 followed by a 15 degree half-angle divergence. The subsonic area ratio of 1.34 was sized to produce Mach 0.5 flow conditions within the combustion chamber [6]. An exploded view of the entire RDE is provided in Figure 3.

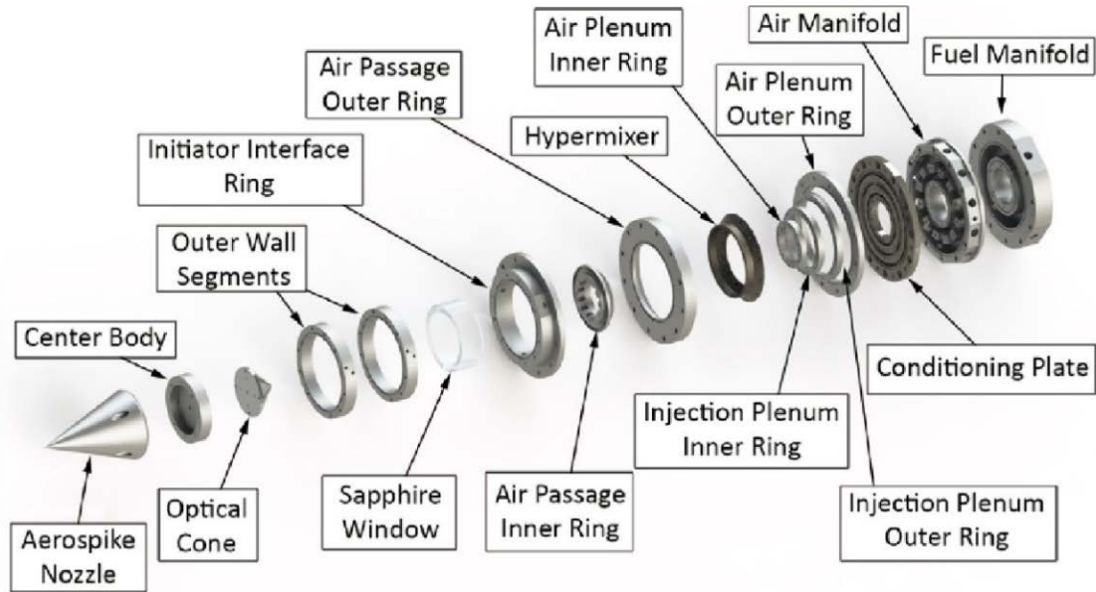


Figure 3. Engine Diagram—Exploded View. Source: [1].

The primary objective of this thesis was to determine whether aerospike nozzle design could be optimized for RDE applications using steady-state solutions. To date, no nozzle design technique accounts for the unsteady nozzle inlet dynamics associated with RDE operation. Thus, the nozzle contour was designed using a traditional, steady-state design methodology although it is expected to experience both on and off-design conditions throughout the combustion cycle. To gain additional understanding of the flow field about the region of the contoured nozzle and to aid in the design process, a steady-state computational fluid dynamics (CFD) investigation was conducted on several geometries over a wide range of operating pressure ratios.

The nozzle design was modeled in SolidWorks, a 3D computer aided design (CAD) software package, and integrated with existing hardware using a stacked assembly approach. Once the nozzle has been machined, it will be instrumented with pressure taps and integrated into the RDE to investigate the effect of RDE-specific flow fields on nozzle performance. By measuring the pressure distribution across the aerospike nozzle during RDE operation, the performance impacts of aerospike nozzles on RDEs will be characterized. The results of these experiments will be compared to the computational results and subsequently used to optimize aerospike nozzle design for RDE applications.

THIS PAGE INTENTIONALLY LEFT BLANK

II. BACKGROUND

The effect of spatially and temporally unsteady flow fields on aerospike operation has not been fully characterized. Thus, an optimal design technique has not been developed for the application of aerospike nozzles to RDEs. As a result, a comprehensive understanding of unsteady RDE characteristics and steady-state aerospike nozzle flow fields become critical in a first iteration aerospike design for RDEs. Chaves [6] and Ellsworth [1] provide excellent references on the thermodynamics behind detonation combustion and RDE operation. The following section introduces basic nozzle theory and illustrates the principles of aerospike nozzle flow physics. Based on this information, this work will take a methodical approach toward optimization of aerospike nozzle design for RDEs.

A. THRUST

Thrust is the reaction experienced by a propulsion system's structure due to the ejection of mass at a high velocity [10]. According to Newton's laws, one could determine the thrust on a propulsion system by evaluating an integral of the pressure and shear forces acting over all surface elements of the rocket [11]. Thrust, the resultant net force, would then be computed as the sum of the forces on these surfaces, as shown in Figure 4.

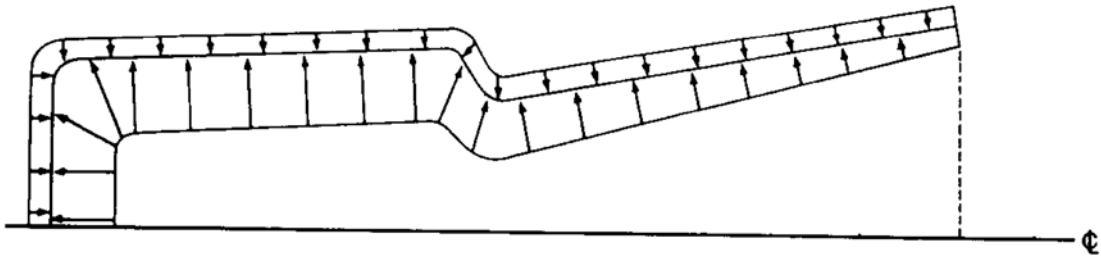


Figure 4. Pressure Distribution on a Simplified Rocket Casing.
Adapted from [11].

Any complexities in the system geometry, however, render this method very tedious, as seen for the turboshaft engine in Figure 5.

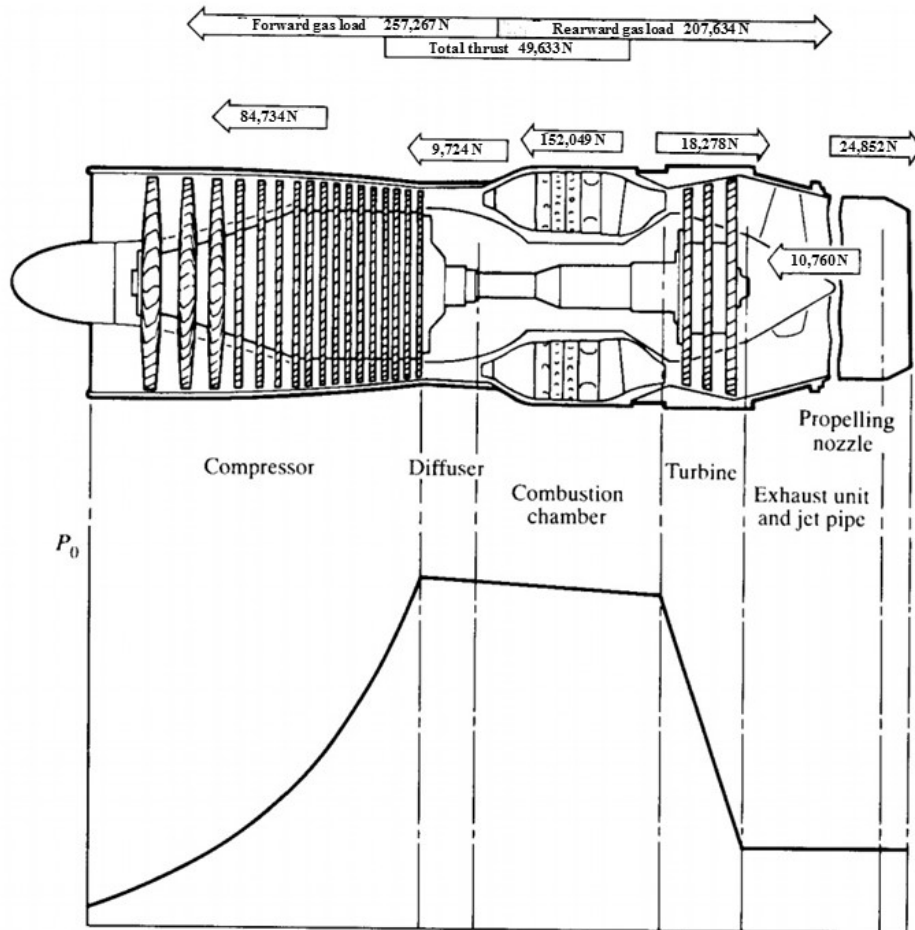


Figure 5. Internal Total Pressure and Thrust Distribution in a Turbojet Engine. Adapted from [11].

Instead, thrust calculations are best performed with a control volume analysis that also tracks momentum flux across a boundary. Propulsion systems develop thrust by imparting momentum to the fluid passing through them. Thus, a general equation for thrust can be developed from the momentum equation for a well-prescribed control volume without the need for detailed consideration of rocket geometry [11]. An example of a well-prescribed control volume for a simplified rocket geometry is shown in Figure 6.

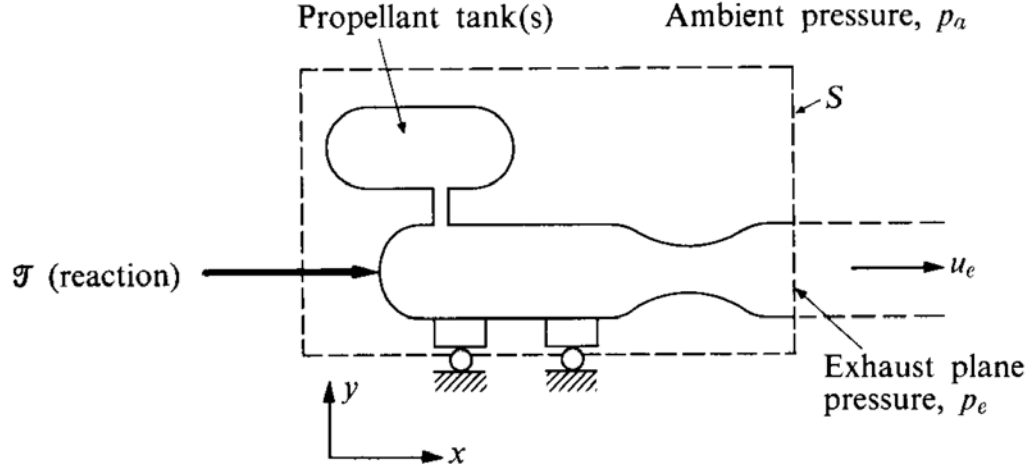


Figure 6. Well-Prescribed Control Volume for a Simplified Rocket Geometry. Source: [11].

Applying Newton's second law to a control volume results in the momentum equation, which relates momentum flux to forces on the control volume. Further application of the momentum equation to the stationary rocket indicated in Figure 6 shows how the thrust developed relates to the propellant flow rate, exhaust velocity and pressure, and ambient conditions. For a steadily operating rocket propulsion system, the total thrust is computed as [10]:

$$F = \dot{m}v + (p_e - p_a)A \quad (1)$$

where:

\dot{m} = propellant flow rate

v = propellant exhaust velocity relative to the vehicle

p_e = local pressure at the nozzle exit plane

p_a = atmospheric pressure

A = cross-sectional nozzle exit area

The first term of Equation (1), $\dot{m}v$, represents the momentum thrust due solely to the momentum imparted to the fluid. The second term, $(p_e - p_a)A$, represents the

pressure thrust at the exit plane, which is nonzero only when there exists an imbalance in ambient pressure and local exit pressure.

B. NOZZLES

Based on Equation (1), it is clear that the amount of thrust produced depends on the mass flow rate through the engine, the flow exit velocity, and the pressure at the exit [12]. The nozzle design of a rocket determines the values of these three variables [12]. Thus, the purpose of a nozzle is to expand and accelerate combustion products to high exit velocities. Maximum possible thrust is obtained by complete expansion of the exhaust gases to the ambient pressure through a nozzle designed to output a parallel uniform jet at the exit [13].

1. Basic Design

In order to reach supersonic flow conditions, nozzles must consist of a converging section followed by a diverging section. The subsonic (converging) section of a nozzle accelerates the flow from near-stagnation conditions in the combustion chamber to the nozzle's throat (the axial location in the nozzle that has the smallest cross-sectional area), where the flow obtains a Mach number of 1.0. Generally, the subsonic, converging nozzle contour and the throat section are not critical to performance. The favorable pressure gradients in these regions prevent flow separation and render contours of nearly any radius acceptable [10]. On the other hand, the shape of the supersonic or diverging section of the nozzle is of great importance. Even in the absence of boundary layer effects, improper shaping can result in unintended shock formation and performance loss [11]. The diverging portion of the nozzle is primarily what distinguishes different nozzle configurations.

2. Shortcomings of Conventional Nozzles

A number of different nozzle configurations are available today, including cone, bell-shaped, plug/ aerospike, and truncated aerospike nozzles [10]. Figure 7 depicts the geometries of several such configurations.

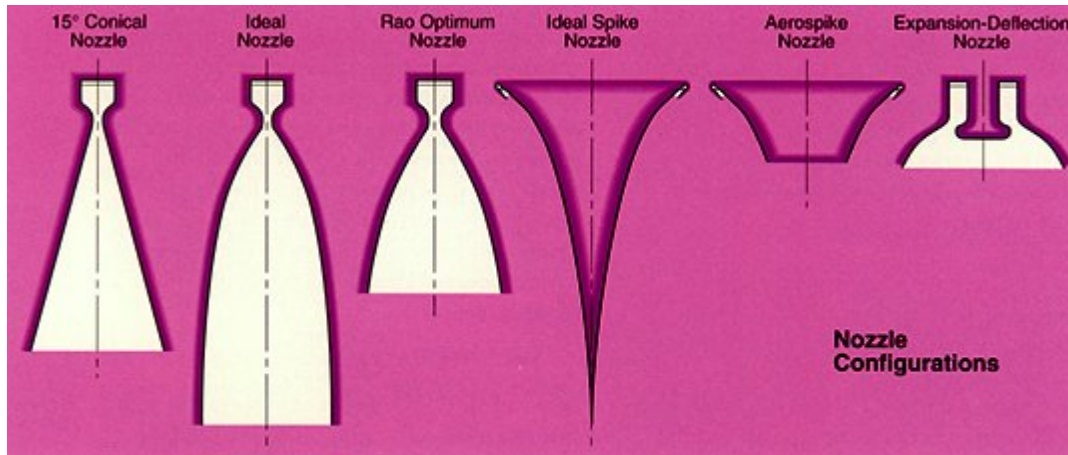


Figure 7. Nozzle Configurations. Source: [14].

The most common nozzle shape today is the bell-shaped or conventional nozzle, primarily for its simplicity and relatively low weight [10]. Additionally, bell nozzles provide higher efficiencies than simpler conical nozzles. In the diverging section of this type of nozzle, propellant gases expand through diverging walls that constrain the expansion away from the centerline [15].

Bell nozzle characteristics are heavily influenced by the flow regime in which they operate. These flow regimes are characterized by the pressure ratio between the chamber pressure and the design exhaust pressure, p_e . Chamber pressure is dictated by the propellant characteristics, while the exit design condition (p_e) is fixed by the area ratio of the nozzle exit area to throat area. For conventional bell nozzles with no moving parts, the nozzle geometry governs the area ratio, which remains constant throughout the engine's operation. The design area ratio can be translated into a design pressure ratio or exit Mach number via the isentropic relations.

The bell nozzle forms a boundary surface that contains the flow until a particular design Mach number or design pressure ratio is achieved, unless flow separation occurs. Nozzles are designed such that, for a constant chamber pressure, the flow is expanded such that nozzle exit pressure (p_e) equals ambient pressure (p_a) at one particular design condition. Thus, Equation (1) indicates thrust is affected by change of altitude (due to the resultant change in p_a).

a. Design Condition

At the design altitude, where $p_e = p_a$, pressure thrust is zero and the nozzle is operating at its design point. The operating pressure ratio assumes its design value because the exit pressure dictated by the nozzle geometry matches the local atmospheric pressure. From a performance standpoint, this represents the ideal, peak efficiency condition.

b. Overexpanded Condition

When the operating pressure ratio is less than the design pressure ratio, nozzle exit pressure will be lower than local atmospheric pressure. This is equivalent to the nozzle area ratio being larger than the optimum area ratio, or the rocket operating at an altitude below the design altitude (where ambient pressure exceeds the design condition). The pressure thrust term will generate a negative value because the supersonic flow has been expanded below the design pressure. These conditions are known as “overexpanded” conditions.

c. Underexpanded Condition

“Underexpanded” conditions exist when the operating pressure ratio is greater than the design pressure ratio. As a result, nozzle exit pressure will be higher than the local atmospheric pressure. That is, further expansion of the supersonic exhaust gases would be required in order to match the ambient pressure. This is equivalent to the nozzle area ratio being lower than the optimum area ratio, or the rocket operating at an altitude above the design altitude (where ambient pressure is lower than the design condition). In a conventional converging-diverging nozzle, an external expansion to ambient pressure occurs outside of the diverging portion of the nozzle.

Underexpanded conditions yield a positive pressure thrust term. Because ambient pressure decreases with altitude, a nozzle operating in the underexpanded regime will experience an increase in thrust with altitude. While thrust increases with altitude in underexpanded conditions, the nozzle is not operating at peak efficiency. A higher specific impulse could be obtained by expanding the exhaust further to the local ambient

pressure, which would yield a higher exit velocity (v). Ultimately, the highest thrust possible at a given altitude occurs when the exhaust gases are expanded to match the local ambient pressure at that altitude.

Figure 8 depicts the bell nozzle exhaust plume in overexpanded, on-design, and underexpanded conditions.

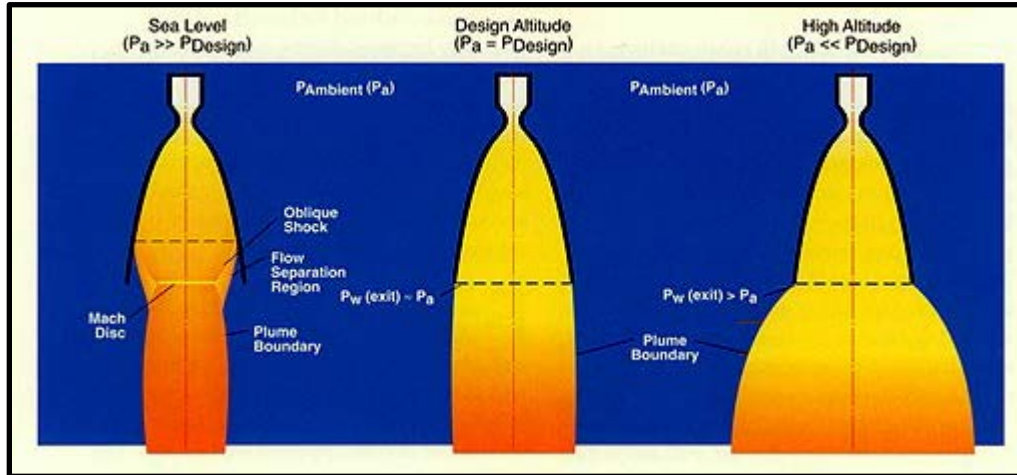


Figure 8. Bell Nozzle Exhaust Plume Comparison. Adapted from [14].

3. Altitude Compensation: An Alternative to Conventional Nozzles

Conventional nozzles are designed for a particular exit pressure. Thus, bell nozzle design involves a compromise between high altitude performance and the avoidance of flow separation when operating at low altitudes [15].

Development of a nozzle with the capability of producing optimum thrust over a wide range of altitudes has been a continuous subject of research in the rocket propulsion community. The military in particular has an interest in development of such a nozzle because military missions often require propulsion systems that operate efficiently over a wide range of ambient conditions. A class of nozzles called altitude compensating nozzles satisfy this requirement by allowing for nearly optimum performance at off-design conditions [10]. Altitude compensation is the ability to reduce over-expansion

losses at low altitudes while producing a significant portion of total thrust during high altitude operation [16].

C. INTRODUCTION TO AEROSPIKE NOZZLES

One type of altitude-compensating nozzle is the aerospike nozzle, which is an expansion device that attaches downstream of an annular doughnut-shaped combustion chamber and an annular nozzle slot [10]. Aerospike nozzles have attracted researchers since the mid-1950s [17], and have received renewed interest since the start of NASA's Single Stage to Orbit (SSTO) program in the 1990s. Figure 9 depicts an ideal, full-length, annular aerospike nozzle.



Figure 9. Annular Aerospike Nozzle. Source: [18].

The aerospike nozzle shape is often described as a bell nozzle turned inside-out and upside-down [19]. Berman and Crimp [20] note that a plug nozzle “may be looked upon as a modification of a conventional nozzle; the significant point of departure [being] that the supersonic expansion, which is generally not confined within solid walls, is continuously ‘re-directed’ by the ambient pressure to produce an essentially axial velocity vector.” One of the main properties of these nozzles is that their interaction with the external ambient prevents the flow separation phenomena that affect conventional bell nozzles [21].

The aerospike nozzle is also sometimes referred to as a “plug” nozzle, which refers to the centerbody that prevents the exhaust gases from flowing through what would be the centerline of a traditional nozzle. While the terms “plug” and “spike” nozzles are interchangeable, some authors use the term “aerospike nozzle” to refer to truncated spike nozzles with base bleed [22]. In this thesis, all three terms will be used interchangeably.

Rather than an outer wall (as in a conical or bell-shaped nozzle), the typical aerospike nozzle’s outside aerodynamic boundary in the divergent section is the interface between the hot gas and ambient air [10]. Since the flow is directly exposed to ambient pressure and its expansion is directly coupled to the external environment, automatic and continuous altitude compensation occurs with no moving parts.

In overexpanded conditions (corresponding to low altitude operation or a low pressure ratio), a shock wave forms on the plug to match the pressure to the surrounding ambient pressure. As ambient pressure decreases with altitude, the gas boundary expands outward and the shock wave moves further downstream. In underexpanded conditions (very high altitudes or pressure ratios), the shock wave moves off the plug altogether. Figure 10 shows the aerospike’s altitude-compensating characteristics. Note that the plug nozzle featured in Figure 10 is truncated, and thus experiences a recirculation region at the nozzle base. The flow features at these various conditions are very complex and will be discussed later.

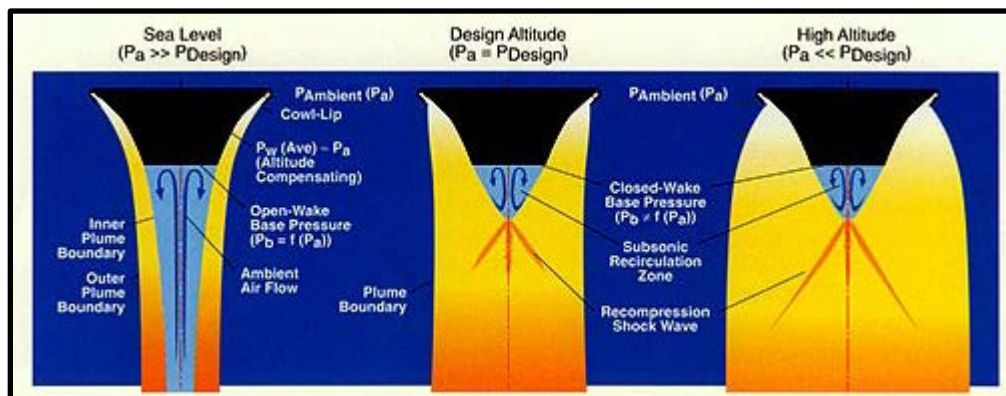


Figure 10. Aerospike Exhaust Plume Comparison. Adapted from [14].

In addition to altitude compensation, aerospike offer a significant advantage over conventional bell nozzles in terms of weight. Plug nozzles generally result in lower vehicle weights because they allow the engine to be integrated into the vehicle structure [23].

D. CLASSIFICATION OF AEROSPIKE NOZZLES

For classification purposes, two varieties of aerospike nozzles exist. They may be classified as either annular or linear.

1. Annular Aerospike Nozzles

The term “annular” refers to the fact that combustion occurs along a ring, or annulus, around the nozzle base. Three primary variations of annular aerospike nozzles exist:

a. Completely External

A completely external aerospike is a traditional curved spike with all supersonic expansion occurring externally, as shown in Figure 11.

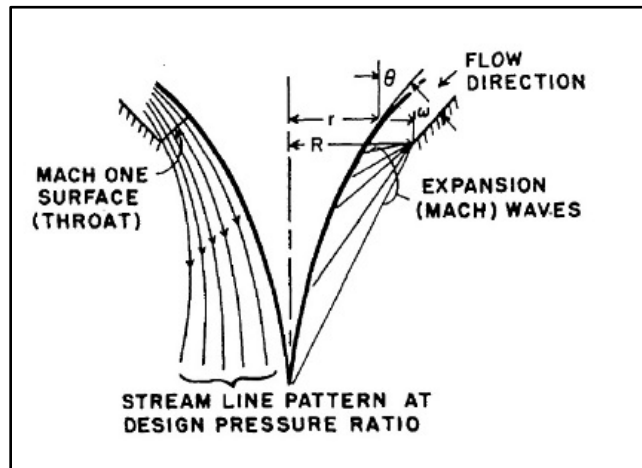


Figure 11. Completely External Aerospike. Adapted from [20].

b. Internal-External

An internal-external spike has a similar shape in which some supersonic expansion occurs internally within a cowl. See Figure 12.

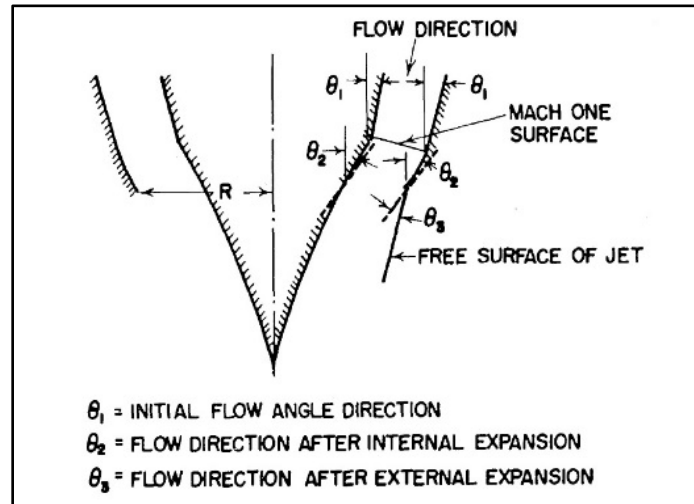


Figure 12. Internal-External Aerospike. Adapted from [20].

c. Completely Internal

The completely internal design is similar to an expansion-deflection nozzle, except that all expansion of the exhaust gases occurs internally. Figure 13 depicts this annular aerospike variation.

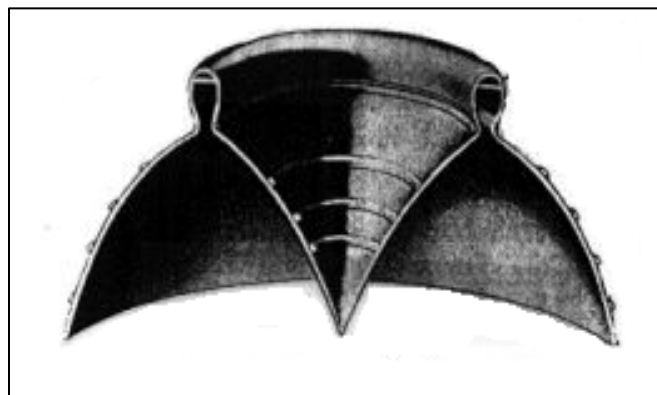


Figure 13. Completely Internal Aerospike. Adapted from [20].

Because annular nozzle throats can cause combustion problems due to uneven fuel/air distribution, an alternate practical version is composed of several small chambers with round throats arranged in a circle that fire along a shared aerospike nozzle [10]. Figure 14 depicts this type of configuration.

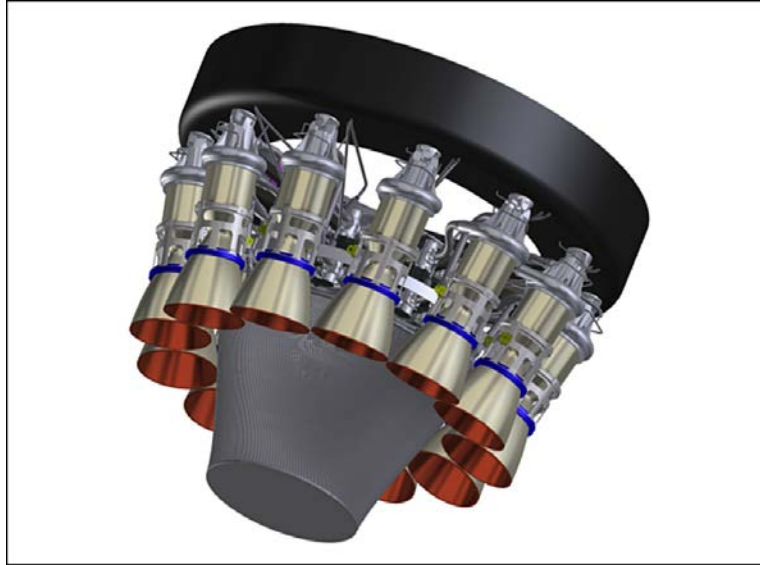


Figure 14. Alternate Combustion Chamber Arrangement. Source: [24].

Jackson et al. [23] explain that another feature of this arrangement is “the ability to provide thrust vector control (TVC) by differential throttling of the engine combustion elements, rather than the more conventional approach of gimballing the entire engine.” That is, the chamber pressure can be raised in one unit while being lowered in another, allowing the exhaust gases to translate and rotate with respect to the symmetry of the plug [20].

2. Linear Aerospike Nozzles

The second class of aerospike nozzles, known as the linear aerospike nozzle, was an approach pioneered by Rocketdyne in the 1970s [25]. Linear aerospike nozzles assume the shape of an annular aerospike that has been unwrapped and laid flat [19], as shown in Figure 15.

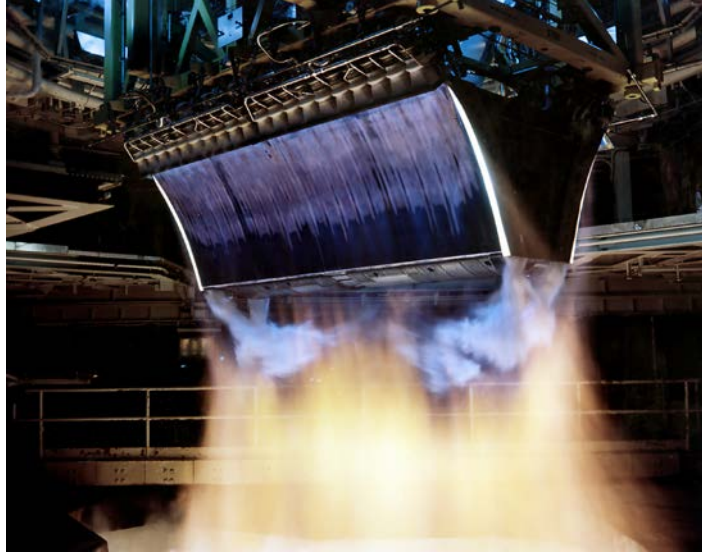


Figure 15. Linear Aerospike Nozzle. Source: [26].

NASA's SSTO program in the 1990s experimented with TVC by differential throttling of the combustion elements. Like the annular aerospike nozzle, the linear aerospike nozzle also possesses the advantages of altitude compensation and lower vehicle weight. This weight reduction results from the integration of the engine into the structure of the vehicle itself. In practice, they feature a series of small combustion chambers along the outer surface, also known as the ramp, similar to the configuration in Figure 14.

3. Truncation of Aerospike Nozzles

Despite their advantages over conventional nozzles in terms of altitude compensation, the practical application of ideal aerospike nozzles has structural and thermal limitations due to the sharp end of the plug. These problems can be largely averted by truncating the ideal plug to some fraction of its full length, reducing the weight and length of the nozzle while increasing its strength [17].

One of the main advantages of plug nozzles is that truncation does not significantly inhibit their performance, even when the nozzle is truncated at a small fraction of its length [21]. Like in conventional nozzles, the contour at the aft end of an ideal plug is perpendicular to the nozzle axis. Because the force acting on the plug wall at

this end point is in a direction perpendicular to the centerline, it contributes only a very small fraction of the overall nozzle thrust. Thus, truncation does not result in a significant thrust loss from the contour.

However, truncation results in a wake at the base of the plug nozzle that has some performance loss [15]. The base region is depicted in Figures 14 and 15. Fortunately, the recirculation region at the base of the cutoff exerts a thrust force, and truncation losses can be largely offset by bleeding a secondary exhaust flow into this region, increasing the back pressure [10].

Experimental results show that base truncation has a negligible effect on thrust in underexpanded conditions [17]. In contrast, thrust loss was found to increase with larger values of truncation in overexpanded conditions. However, the truncated nozzle in overexpanded conditions still maintained better performance than the conventional bell nozzle. Thus, proper selection of the amount of plug truncation depends on the vehicle's flight regime. If the majority of the thrust flight phase is to take place at altitudes lower than design altitude (overexpanded conditions), a lower value of nozzle truncation (yielding a longer nozzle) should be selected. If most of the thrust flight will take place above the design altitude (underexpanded conditions), a higher value of truncation (yielding a shorter nozzle) is recommended [17].

E. FLOW PHYSICS OF PLUG NOZZLES

Figure 16 depicts the geometry of an aerospike nozzle and associated terminology. The shroud is sometimes referred to as the “cowl,” and the shroud base is sometimes referred to as the “vehicle base.”

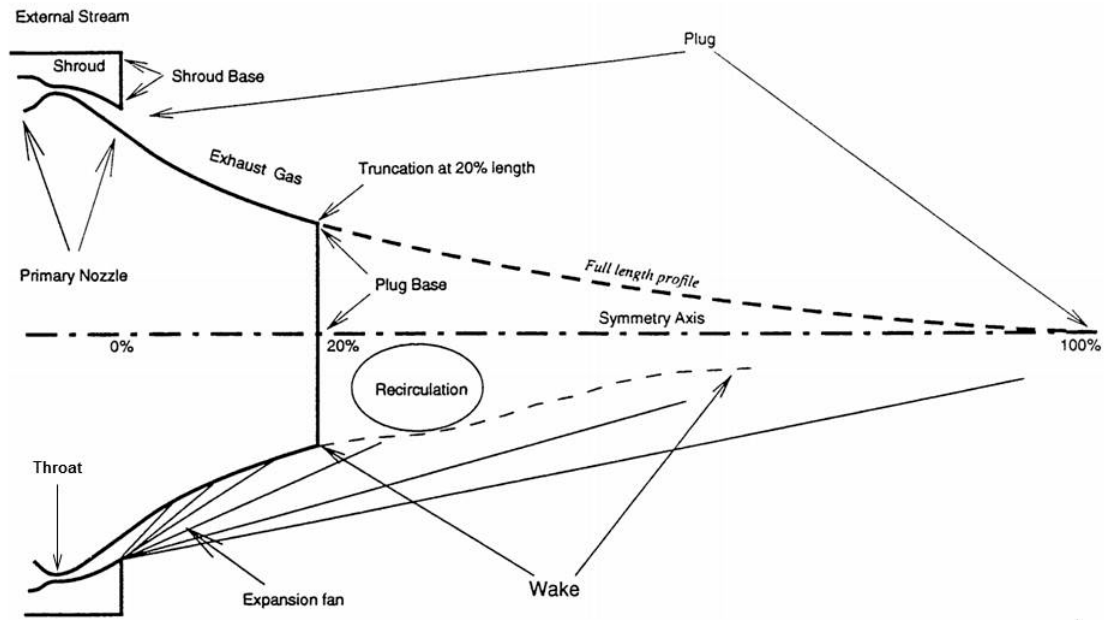


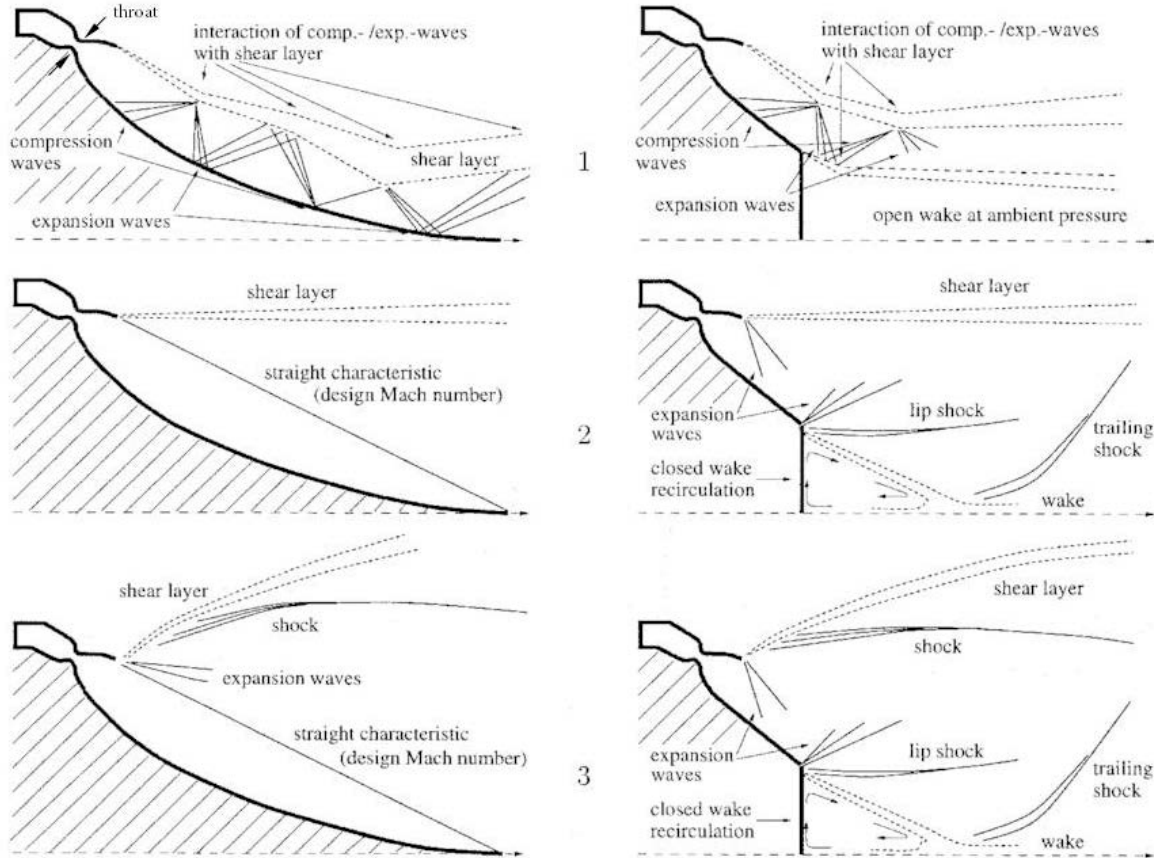
Figure 16. Aerospike Terminology. Adapted from: [27].

Note that the aerospike nozzle geometry will have a flat base when the plug contour stops short of the nozzle centerline. This situation occurs when a full-length nozzle is truncated, as in Figure 16, or when the contour is designed using Angelino's approximate method [28]. For these cases, a recirculation region develops at the nozzle base.

The flow physics of plug nozzles differs according to ambient conditions. That is, an aerospike will experience different flow features in quiescent air and in a co-flowing free-stream.

1. Flow Features in Quiescent Air

Figure 17 summarizes the principle flow features of annular plug nozzles with full length and truncated central bodies at on-design (17-2) and off-design conditions (17-1 and 17-3).



“Flow phenomena of a plug nozzle with full length (left column) and truncated central body (right column) at different pressure ratios p_c/p_{amb} , off-design (top, bottom) and design (center) pressure ratio.” [29].

Figure 17. Flow Features of a Plug Nozzle. Adapted from [29].

When the flow is choked at the throat, the exhaust gases undergo a centered expansion at the shroud lip and rotate up to the axial direction. The supersonic expansion flow features vary according to the operating conditions.

a. Design Condition

At the design condition, the last expansion wave emanating from the nozzle lip impinges on the tip of the plug contour (Figure 17-2). After passing this expansion wave, the jet exhaust pressure matches the ambient pressure at design altitude and the exhaust flows uniformly in the axial direction with a total turning angle α [30]. The corresponding computed wall pressure is a monotonic decreasing function [21]. The jet

boundary (shear layer) profile assumes a straight line that is parallel to the nozzle centerline, originating from the shroud lip.

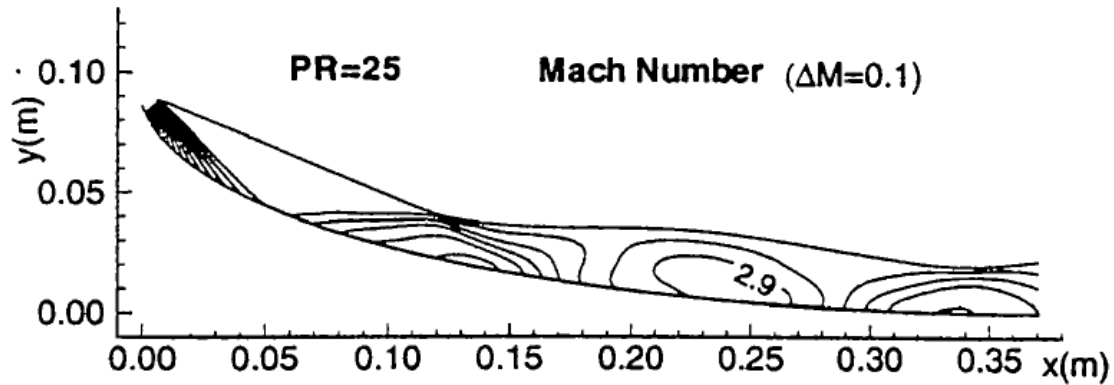
b. Underexpanded Condition

In underexpanded conditions (Figure 17-3), the pressure ratio exceeds the design pressure ratio, so further expansion is required at the primary nozzle lip to match the exit pressure to ambient. The additional expansion waves required to match the pressures do not impinge upon the plug contour, so that the design Mach number and wall pressure distribution are maintained from the on-design case. Thus, an underexpanded aerospike nozzle behaves as an ideal nozzle at design conditions. However, an underexpanded plug nozzle behaves like a conventional nozzle in that it loses its capability for further altitude compensation. Like in an underexpanded conventional nozzle, thrust increases only because of the pressure thrust term (the second term in Equation (1)) [21]. The impulse thrust term (the first term in Equation (1)) remains unchanged.

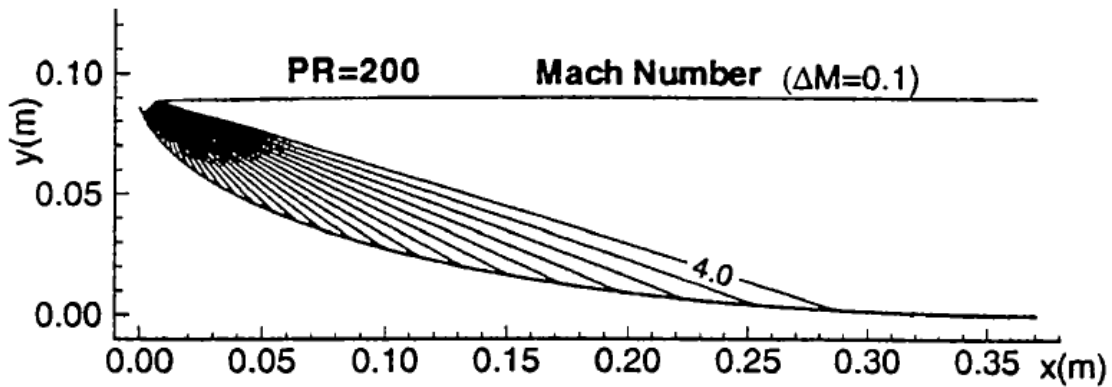
c. Overexpanded Condition

The advantages of plug nozzles are realized through their adaptive capabilities in overexpanded conditions (Figure 17-1), which make them suitable to achieve high expansion ratios at altitude. When the pressure ratio is lower than the design pressure ratio (e.g., when ambient pressure is high during low altitude operation), the exhaust flow undergoes a weaker centered expansion at the primary nozzle lip, and the flow turns less than in design conditions [21]. As the pressure ratio decreases, the last expansion wave impinges on the nozzle contour at decreasing distances from the throat [21]. Downstream of the final expansion wave, the plug geometry generates compression waves which interact with the constant-pressure jet boundary to form an additional expansion fan. This expansion fan causes the flow to expand again downstream, where the whole cycle can be repeated. Thus, the aerospike nozzle adapts the exhaust flow to ambient pressure via a system of recompression shocks and expansion waves [21]. The compression and expansion waves interact with the shear layer, producing inflections of the shear layer and causing it to enlarge farther downstream of the throat via turbulent diffusion [29].

Figure 18 shows the altitude compensation characteristics of a plug nozzle by comparing Mach number contours in overexpanded conditions (a) and on-design conditions (b). Note the characteristic barrel-like form of the exhaust flow in overexpanded conditions that results from a system of shocks and expansion waves [29].



(a) High ambient pressure operation



(b) Design operation

Figure 18. Mach Isolines and Jet Boundary in a Linear Full-Length Plug.
Source: [27].

2. Flow Features in a Supersonic Free Stream

Aerospike nozzle flow features change when a co-flowing supersonic free stream is introduced. The significant departures from the quiescent air case include the development of a plume shock and a recirculation region downstream of the shroud base.

Similar to the quiescent air case, the primary flow from the combustion chamber expands downward along the plug nozzle surface and then around the corner at the end of the plug. Figure 19 (a-c) shows sketches of the fully developed flow fields in various pressure ratio conditions.

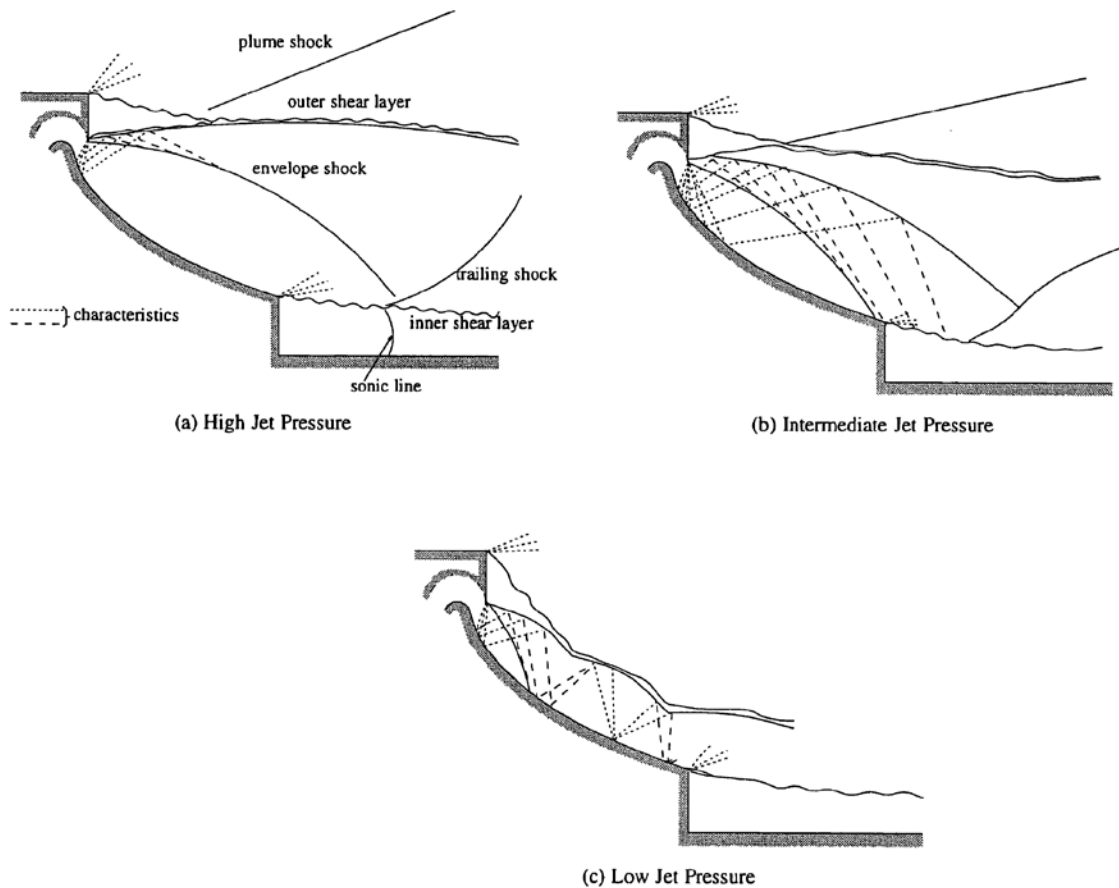


Figure 19. Plug Nozzle Flow Field at Various Jet Pressures. Adapted from [15].

a. High Pressure Ratio

For the high pressure ratio case (Figure 19(a)), the nozzle base recirculation region is bounded by the inner shear-layer, the nozzle base, and the sonic line of the base region. An envelope shock forms on the outboard side of the primary jet plume to match the jet flow velocity to the expanded free stream. At the shroud base, another subsonic region exists, bounded by the jet boundary and outer shear layer. This “dead-air region” is depicted in Figure 20.

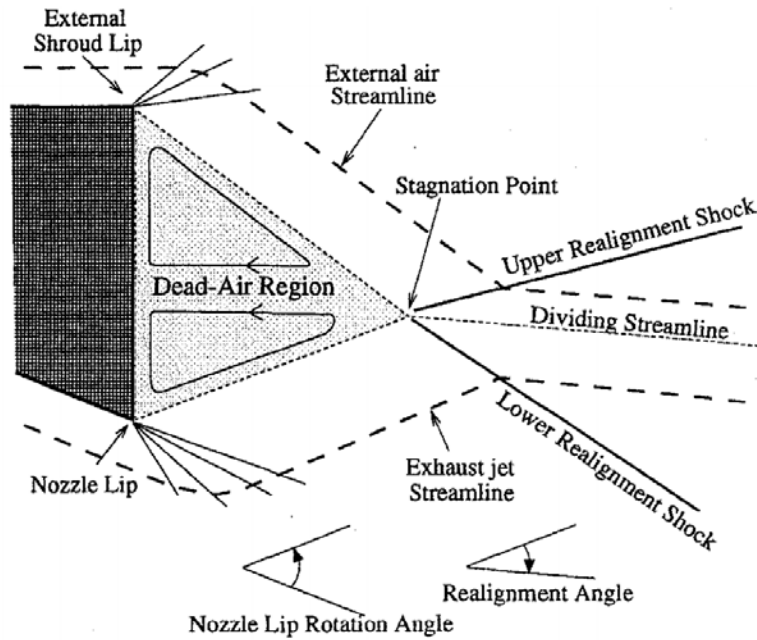


Figure 20. Schematic View of the Interaction Between Exhaust and External Supersonic Jets Behind the Primary Nozzle External Shroud.

Source: [27].

Because the free stream is supersonic, it gets compressed by the jet plume and forms a plume shock. Expansion waves originating from the nozzle lip reflect from the plug contour as expansion waves and then from the jet boundary as compression waves [31]. The compression waves coalesce and develop an envelope shock. The surface pressure at the plug contour continuously decreases with increasing axial distance, following the trend of the theoretical pressure distribution by a two-dimensional Prandtl-Meyer expansion [15].

b. Intermediate Pressure Ratio

In Figure 19(b), a lower pressure ratio drives the jet flow. The lower jet pressure brings the envelope shock upstream along the plug contour so that compression waves coming from the jet boundary impinge on the plug contour and inner shear layer [15].

c. Low Pressure Ratio

Figure 19(c) shows a flow field corresponding to overexpanded (low pressure ratio) conditions. The envelope shock is pushed even further upstream so that the compression and expansion waves impinge along a greater length of the plug contour. This generates an oscillating pressure distribution on the aerospike, and the altitude compensating characteristics are therefore directly related to the location of the compression waves in the flow [32].

F. FLOW PHYSICS OF THE NOZZLE BASE

Many experimental and theoretical studies have confirmed the existence of two wake regimes that can be experienced by the base of a plug nozzle; the “open wake” and “closed wake” regimes. In the open wake regime, base pressure is dependent on ambient pressure, while in the closed wake regime, base pressure is independent of ambient pressure.

1. The Open Wake Regime

In overexpanded conditions (Figures 17-1 and 19(c)), the jet boundary is close enough to the nozzle contour (that is, the plume does not significantly expand) for compression waves to impinge on the plug contour and inner shear layer. The nozzle base pressure is increased by the compression waves impinging on the inner shear layer bounding the subsonic region at the nozzle base [15]. The nozzle base remains under the influence of ambient pressure as long as the compression waves impinge on the inner shear layer. Because the nozzle base pressure is sensitive to ambient pressure, the plug nozzle is said to be operating in the “open wake” regime. Altitude compensation affects the nozzle pressure thrust only during the open wake regime [15].

The open wake regime is sometimes further classified into type 1 and type 2 flows based on the location of the expansion fan along the plug contour [33], [34], [35]. Type 1 flows, typically occurring at lower pressure ratios, are marked by intense wave interactions on the plug surface. This configuration occurs when the expansion fan ends upstream of the nozzle exit plane so that the compression and expansion waves impinge along a significant length of the plug contour, as in Figures 17-1 and 18(a). Type 2 flows occur when the entire plug surface resides under the characteristic lines of the expansion fan emanating from the primary nozzle lip, as in Figures 17-2 and 18(b). Type 2 flow is marked by a constant pressure at the plug lip. Plug base pressure varies continuously in type 1 and 2 flows.

2. The Closed Wake Regime

As the pressure ratio increases, the jet boundary moves outward such that the compression waves and/or envelope shock move downward along the plug contour. Once the compression waves move downstream of the sonic line of the nozzle base flow (Figure 17-2), an additional decrease of ambient pressure has no further effect on nozzle base pressure [36]. The plug nozzle is said to be in the “closed wake” regime as the nozzle base pressure is insensitive to ambient pressure.

The closed wake regime is sometimes referred to as type 3 flow. A constant base pressure is characteristic of this type of flow.

3. Open/Closed Transition

Nasuti, Onofri, and Chutkey et al. [21], [27], [33], [34], [37] independently present detailed engineering models for prediction of transition between wake states in both still air and supersonic flow. Essentially, the wake is said to be closed if the last characteristic wave of the expansion fan centered at the nozzle lip impinges on the wake downstream of the reattachment point [21]. Figure 21 depicts closed wake operation because the final expansion wave (g) impinges downstream of the reattachment point (E).

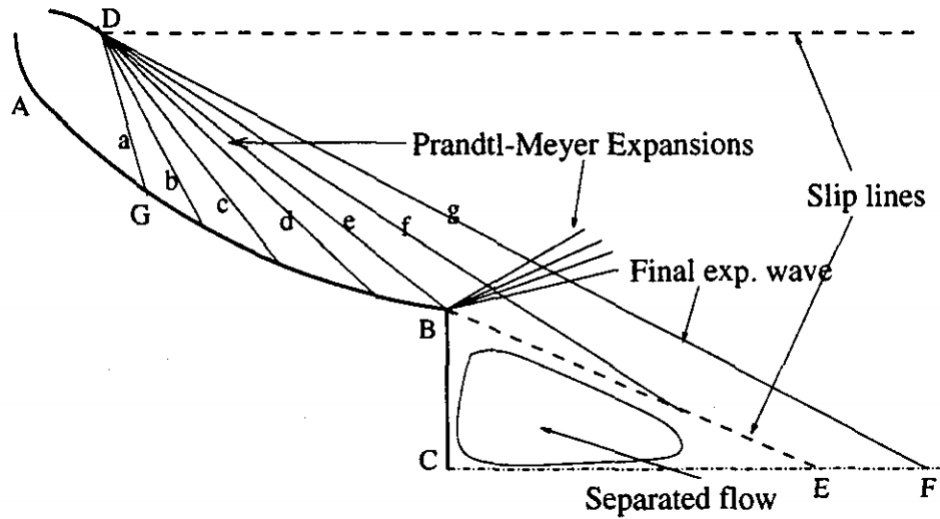


Figure 21. Schematic View of Closed Wake Operation. Source: [37].

The last expansion wave of the fan (g) carries the ambient pressure value [37]. When (g) interacts with the base region, the wall pressure acting on the truncated base is affected by the ambient pressure [37]. The limiting case for closed wake operation occurs when the final expansion wave (g) intersects the reattachment point (E). Thus, Figure 22 shows the limiting case for closed wake operation because (g) is just outside of the base recirculation region.

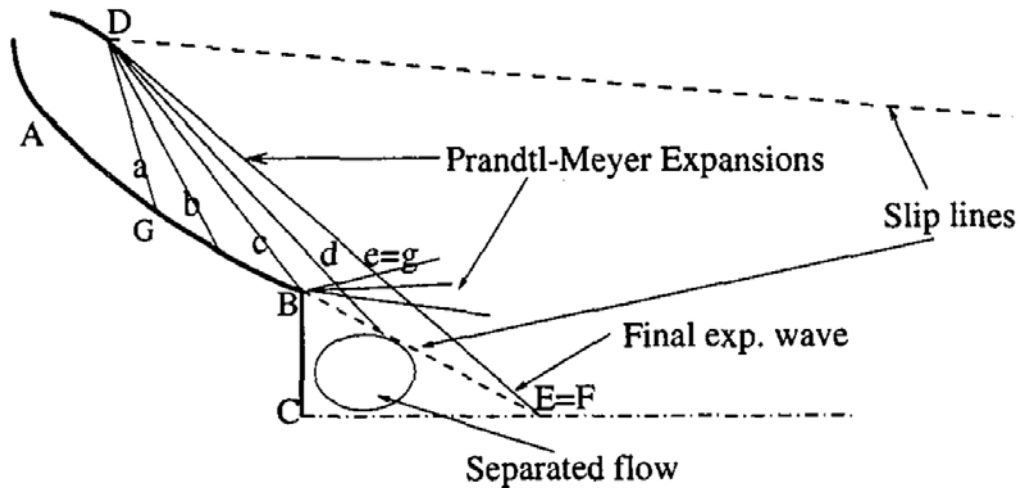


Figure 22. Closed-Open Wake Transition. Source: [37].

An engineering model derived in [37] provides a prediction for the pressure ratio PR_{tr} at which the closed-open wake transition occurs. To evaluate the point where the wave (g) impinges on the nozzle axis in the annular plug case, the characteristic lines can no longer be approximated by straight lines. Close to the centerline, they become curved due to the axisymmetric effect. Figure 23 shows an exaggerated effect of the flow axisymmetry on the curvature of characteristic line (g).

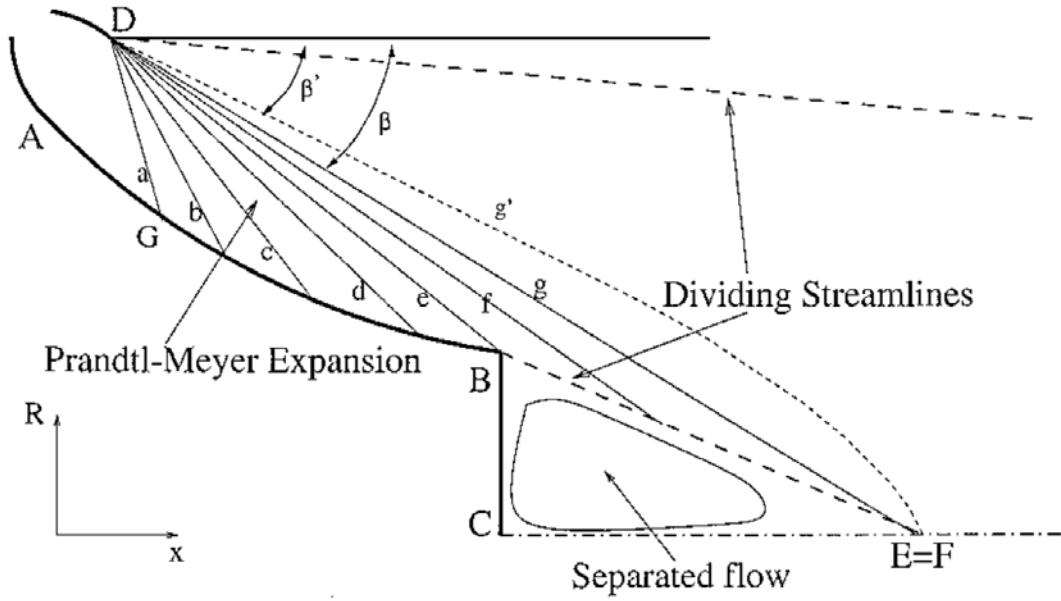


Figure 23. Schematic of Characteristic Lines at Closed-Open Wake Transition.
Source: [37].

Compared to the straight line (g), the actual line (g') corresponds to the larger expansion indicated by the angle β' . Nasuti and Onofri [37] use the classic Prandtl-Meyer expansion relations to compute β' for an assigned pressure ratio. They define the corrected angle

$$\beta' = \beta + \Delta\beta \quad (2)$$

to allow for the determination of F by drawing a straight line. It has been shown that a constant value $\Delta\beta = 5^\circ$ can be assumed.

The following model allows for the prediction of PR_{tr} by iteration:

$$\beta' = \mu(M_{tr}, \gamma) - \nu(M_{tr}, \gamma) + \nu(M_e, \gamma) + \delta \quad (3)$$

$$M_{tr} = \left\{ \frac{2}{\gamma - 1} (PR_{tr}^{(\gamma-1)/\gamma} - 1) \right\}^{1/2} \quad (4)$$

where:

PR_{tr} = transition pressure ratio

M_{tr} = transition Mach number

M_e = design exit Mach number

δ = flow direction at the primary nozzle exit (in this case, the throat)

ν = Prandtl-Meyer function

μ = Mach angle

The angle β is evaluated trigonometrically via the ratio CE/BC. The following experimental correlation has been suggested for use with annular plug nozzles [37]:

$$\frac{CE}{BC} = 2.65 - 0.00144\varphi^2 \quad (5)$$

where φ is the exit angle of the plug. The assumption that CE is approximately 2.65 times the length of BC has been shown via backward-facing step computations, and holds for an approaching flow Mach number greater than 2.0 [37]. The corrective parameter (the second term on the right-hand side of Equation (5)) adjusts for the departure from the backward-facing step case due to the difference in plug exit angle. By iterating through PR_{tr} values, β' can be computed independently via Equations (2) and (3), and compared until the correct PR_{tr} is selected.

4. Base Pressure Prediction

A universally accepted model to predict plug nozzle base pressure has not yet been established. Furthermore, the complexities of plug nozzle base flow render prediction methods different for the open and closed wake regimes.

a. Open Wake Base Pressure Prediction

It is important to note that open wake operation does not guarantee that base pressure will be equal to the local ambient pressure. Rather, operation in the open wake regime just indicates that base pressure varies in the radial direction about the ambient pressure value, depending on the prevailing pressure at the plug lip, which in turn depends on the nature of the wave interactions at lower pressure ratios [34], [33]. For annular plug nozzles in the open wake regime, base pressure has been shown to vary about the atmospheric pressure value, while for the linear plug case, the open wake base pressure can be reasonably approximated to atmospheric pressures [21], [34].

Development of an empirical model for predicting the open wake base pressure has proven to be challenging due to the sheer complexity of this base flow regime. Both Chutkey et al. [34] and Onofri et al. [21] suggest that, from the viewpoint of design, it is reasonable to assume an atmospheric pressure prevails on the base surface in the open wake regime. In this case, the problem becomes predicting the transition pressure ratio at which the recirculation bubble closes, rather than predicting the nozzle base pressure.

b. Closed Wake Base Pressure Prediction

The closed wake flow regime is characterized by a constant base pressure. Analytical, pure-empirical, and theoretical/empirical methods have been employed to predict this pressure [21]. The most recent attempt to predict closed wake base pressure for the annular plug nozzle yielded the following empirical correlation based on experimental data in the literature [34]:

$$\frac{p_b}{p_o} = \frac{p_{lip}}{p_o} \left(0.05 + 0.967 \left(1 + \frac{\gamma-1}{2} M_{lip}^2 \right)^{-1} \right)^{0.7027} \quad (6)$$

where p_{lip} and M_{lip} represent the local pressure and Mach number at the lip of the nozzle base, respectively.

c. CFD Predictions

The limitations of present day computational tools in computing plug nozzle base flows is well documented [34], [38]. While CFD has been shown to adequately predict the pressure ratio at which open/closed wake transition occurs, it tends to grossly underpredict the base pressure for most pressure ratios [33], [34]. Furthermore, CFD has been shown to predict a nonuniform base pressure, whereas experimental base pressure is fairly uniform with radius [34].

THIS PAGE INTENTIONALLY LEFT BLANK

III. NOZZLE DESIGN METHOD

A. INTRODUCTION

The nozzle contour must be carefully optimized to provide the maximum thrust for given geometric limitations [39]. An ideally contoured nozzle produces a uniform, one-dimensional flow profile in the exit plane [40]. In principle, this can be achieved with any nozzle type. The common design philosophy for each contour is that at the design pressure ratio, all expansion waves propagating through the flow towards the nozzle wall (and thereby accelerating the flow to the desired design Mach number) are cancelled out by a proper wall contour design [40].

Since the 1950s, various methods have been developed for supersonic nozzle design, although standard design methods for plug nozzles have not yet been established [41]. Many design approaches have been investigated, including those based on the Method of Characteristics (MOC) [42], [43], [44], Rao's calculus of variations [13], a simple approximate method [45], [22], or some combination of these methods. In fact, many aerospoke nozzle designs simply use some combination of quadratic functions [41], 2nd or 3rd order polynomials [39], [46], circular arcs, and/or parabolas [30] to describe the contour. Onofri et al. [21] provide an extensive summary of plug nozzle contour design methods.

In an effort to characterize the differences between various design methods, Nazarinia [17] used both the MOC and Angelino's approximate method to design full-length plugs of two aerospoke nozzles. The resultant geometries yielded almost identical plug shapes, with results showing a maximum difference of 5% in radius. Similarly, Besnard [22] found that the contours for a truncated plug nozzle designed using Rao's method and a nozzle designed using the approximate method differed very little, and the calculated plug lengths were the same. Due to the qualitative similarities between all design approaches in terms of the resultant plug contour, it is reasonable to expect similar performance for any contoured aerospoke designed with the same set of parameters.

B. DESIGN APPROACH: THE SIMPLE APPROXIMATE METHOD

In 1964, Angelino proposed an approximate design method for aerospike nozzle contours [28]. By assuming the flow properties at the plug inlet plane are uniform and one-dimensional, the expansion fan emanating from the shroud lip can be approximated as straight, isentropic, constant-property lines [30]. Several of these expansion fan characteristic lines are shown in Figure 24.

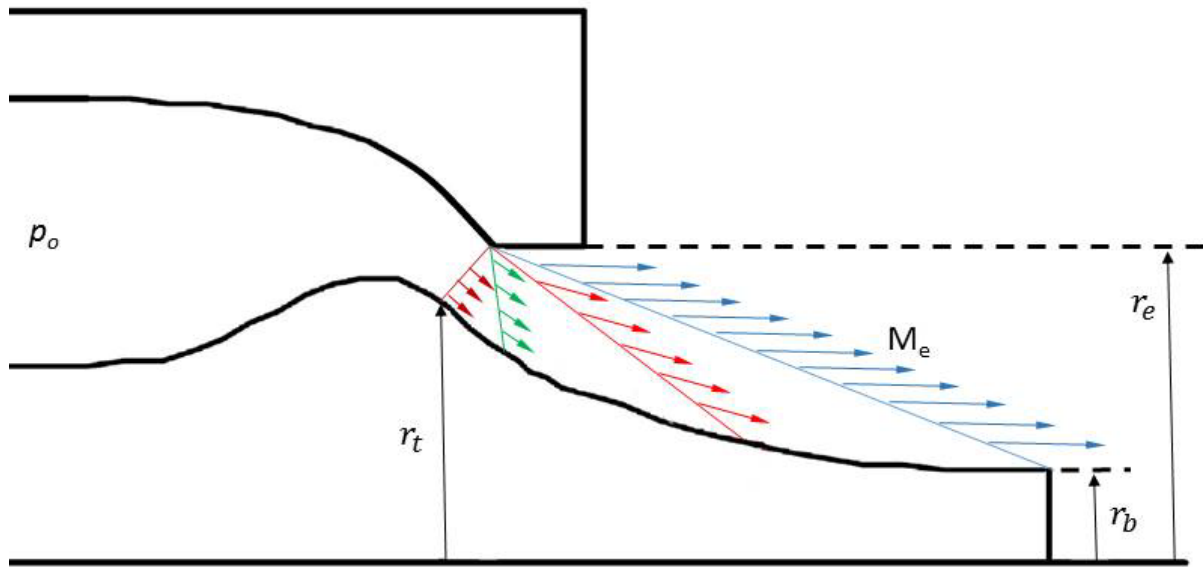


Figure 24. Expansion Characteristic Lines

Provided the expansion characteristics do not depart significantly from straight constant property lines, Angelino found good agreement in terms of plug contours between the approximate method and the MOC. An aerospike nozzle contour designed by this method is referred to as “ideal,” as it would have perfect performance in uniform flowing conditions [30]. This method has been widely adopted due to its simplicity and has proved successful in many experiments [22], [41], [45], [21], [47], [48]. Subsequently, Angelino’s approximate method was implemented to design the plug nozzle contour for the NPS RDE. A derivation of the simple approximate method as it applies to the RDE geometry is provided in the following section (adapted from [22] and [28]).

C. DERIVATION

Denton [43] states that “for maximum thrust, the flow direction of the fluid under sonic conditions should be offset from the axisymmetric line by an angle equal to the Prandtl-Meyer expansion angle associated with the desired exit Mach number of the nozzle.” Since the flow is assumed to be parallel to the nozzle axis at the exit, the throat angle is given by Equation (7):

$$\theta_t = \nu(M_e) \quad (7)$$

where M_e is the Mach number at the exit and ν is the Prandtl-Meyer function. Figure 25 depicts the orientation of θ_t with respect to the aerospike geometry.

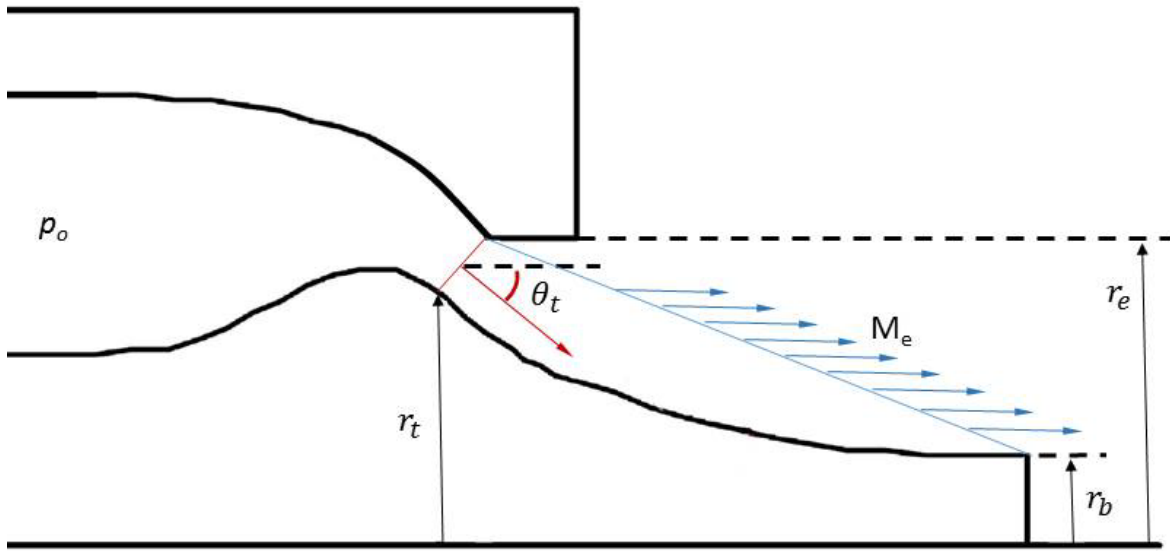


Figure 25. Throat Angle Orientation with Respect to Contour Geometry

M_e can be determined from the design pressure ratio and ratio of specific heats γ via the isentropic flow equation:

$$\frac{p_o}{p} = \left(1 + \frac{\gamma - 1}{2} M^2 \right)^{\gamma/(\gamma - 1)} \quad (8)$$

where p_o / p is the design pressure ratio.

When solved for M_e , Equation (8) becomes:

$$M_e = \sqrt{\left(\frac{2}{\gamma-1}\right) \left(\left(\frac{p_o}{p}\right)^{(\gamma-1)/\gamma} - 1 \right)} \quad (9)$$

The Prandtl-Meyer function required to determine the throat angle, θ_t , is provided in Equation (10). It describes the maximum angle through which a sonic flow can be turned around an apex:

$$\nu(M) = \sqrt{\frac{\gamma+1}{\gamma-1}} \tan^{-1} \sqrt{\frac{\gamma-1}{\gamma+1} (M^2 - 1)} - \tan^{-1} \sqrt{M^2 - 1} \quad (10)$$

Each characteristic line originates from the cowl expansion point and extends toward the centerline at an angle α . This angle is dependent on the Mach angle μ and local flow direction θ , such that $\alpha = \mu + \theta$. Figure 26 illustrates this relationship.

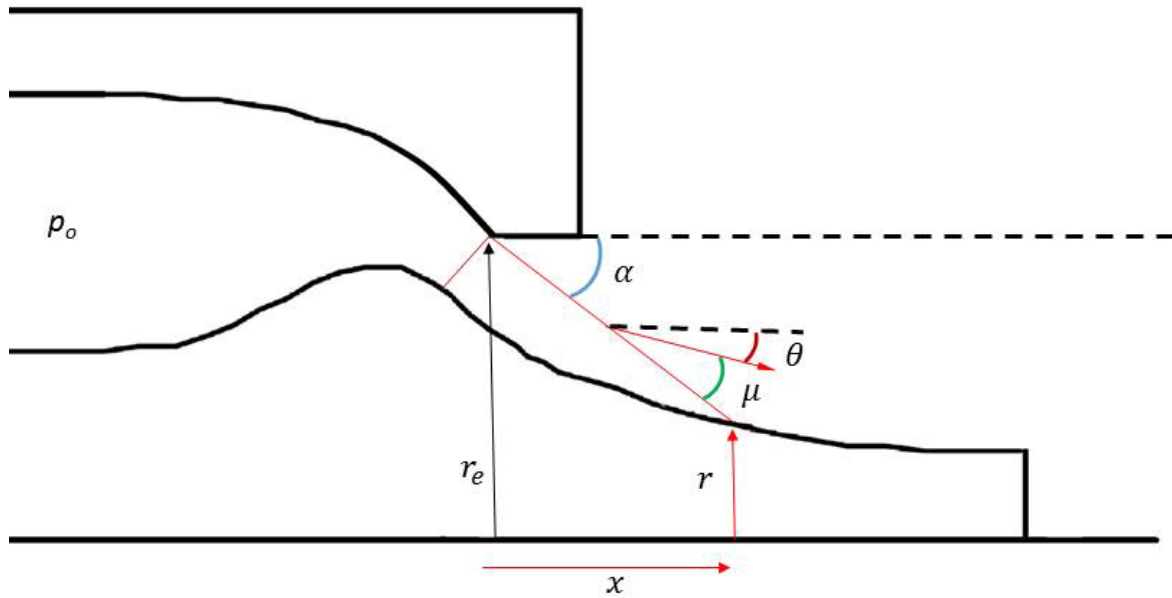


Figure 26. Local Characteristic Line Geometry

Along the aerospike contour, the local flow surface area is generated by the revolution of this characteristic line about the nozzle centerline. This represents the area over which the flow possesses constant properties equal to the flow properties at the plug surface location (x, r) . The resultant area resembles the surface area of a truncated cone, as shown by the red plane in the three-dimensional cutaway view of Figure 27.

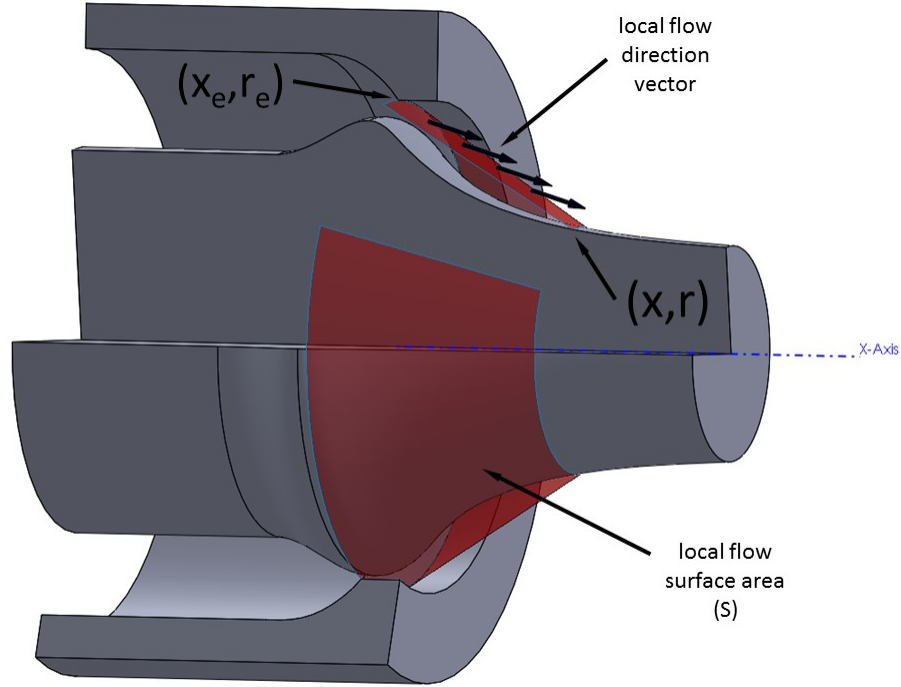


Figure 27. Approximate Method Contour Geometry

The surface area of this truncated cone is given by:

$$S = 2\pi \frac{(r_e + r)}{2} \frac{(r_e - r)}{\sin(\alpha)} = \frac{\pi(r_e^2 - r^2)}{\sin(\alpha)} \quad (11)$$

where α is the characteristic line

$$\alpha = \mu + \theta \quad (12)$$

and θ is the local flow direction that is stepped through by an incremental ν value:

$$\theta = \theta_t - \nu \quad (13)$$

Because the velocity makes an angle μ with the surface S, the local passage area A is only the portion of the conical area perpendicular to the local flow direction. The flow direction is offset from the α characteristic line by the Mach angle μ , such that:

$$A_{local} = S_{local} \sin(\mu) = \frac{\pi(r_e^2 - r_t^2)}{\sin(\alpha)} \sin(\mu) = \frac{\pi(r_e^2 - r_t^2)}{\sin(\mu + \theta)} \sin(\mu) \quad (14)$$

For the throat area, the Mach angle becomes π and the area is reduced to:

$$A_{local} = A^* = \frac{\pi(r_e^2 - r_t^2)}{\cos(\theta_t)} \quad (15)$$

The area ratio A / A^* can thus be written as:

$$\frac{A_{local}}{A^*} = \frac{\pi(r_e^2 - r_t^2) \left(\frac{\sin(\mu)}{\sin(\mu + \theta)} \right)}{\left(\frac{\pi(r_e^2 - r_t^2)}{\cos(\theta_t)} \right)} = \left(\frac{\sin(\mu) \cos(\theta_t)}{\sin(\mu + \theta)} \right) \frac{(r_e^2 - r_t^2)}{(r_e^2 - r_t^2)} \quad (16)$$

Solving for the radial coordinate,

$$r = \sqrt{r_e^2 - (r_e^2 - r_t^2) \frac{A}{A^*} \left(\frac{\sin(\mu) \cos(\theta_t)}{\sin(\mu + \theta)} \right)} \quad (17)$$

In terms of the local Mach number, the area ratio A / A^* is given by the isentropic relationship

$$\frac{A}{A^*} = \frac{1}{M} \left[\left(\frac{2}{\gamma + 1} \right) \left(1 + \left(\frac{\gamma - 1}{2} \right) M^2 \right) \right]^{\frac{(\gamma + 1)}{2(\gamma - 1)}} \quad (18)$$

and the Mach angle is defined as

$$\mu = \sin^{-1} \left(\frac{1}{M} \right) \quad (19)$$

From geometry, the axial coordinate becomes:

$$x = \frac{r_e - r}{\tan(\mu + \theta)} \quad (20)$$

By stepping through the Prandtl-Meyer function incrementally and using the method of bisection to determine the local Mach number, Equations (17) and (20) define the coordinates of the aerospike nozzle contour. This method was converted into a MATLAB code, provided in Appendix A, and subsequently used to generate the aerospike contour for the RDE.

THIS PAGE INTENTIONALLY LEFT BLANK

IV. NOZZLE DESIGN FOR THE RDE

The design methodology detailed in the previous section assumes uniform flow conditions at the throat. No efforts to adapt nozzle design techniques to transient flow fields associated with RDEs have been found in the literature. Thus, Angelino's approximate nozzle design method was applied to the RDE nozzle design recognizing performance will differ from the ideal steady-state prediction. The expectation was that using on and off-design conditions with this technique could provide first-order design guidance until a full unsteady simulation can be obtained.

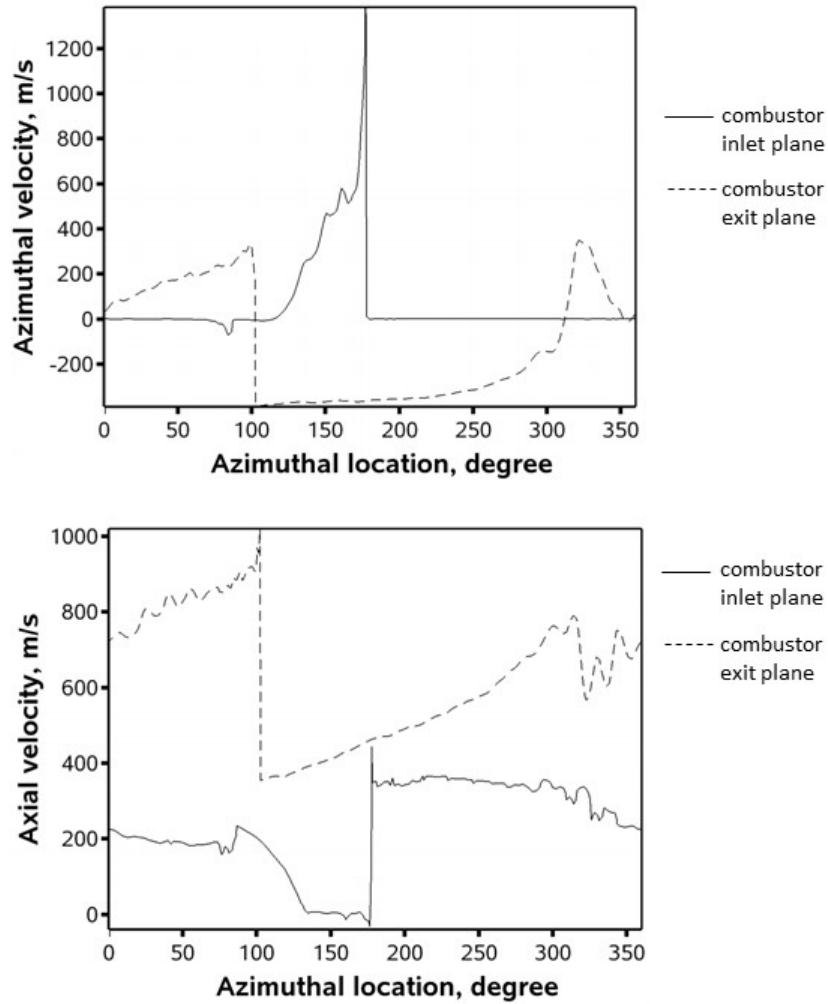
A. NOZZLE DESIGN ASSUMPTIONS

General knowledge of RDE flow fields was employed to make educated design choices for the first iteration of the nozzle geometry. Several assumptions were made to justify these choices.

1. Assumption of Purely Axial Flow

Numerical simulations have shown that flow direction is not purely axial at the exit plane of an RDE combustor, possessing an azimuthal component [2]. To improve the fidelity of the nozzle design, the azimuthal component would need to be accounted for by adjusting the local area ratio experienced by the flow along the resultant velocity vector. Due to the transient nature of RDE operation, it was beyond the scope of this thesis but should be considered for future optimization studies.

Instead, the azimuthal component was assumed to be small compared to the bulk axial flow, so this was neglected in the nozzle design. Figure 28 displays velocity profiles for the flow in a stoichiometric hydrogen-air RDE simulation. This justifies the assumption of small azimuthal velocities by showing the disparity between azimuthal and axial velocity at the combustor inlet and exit planes.



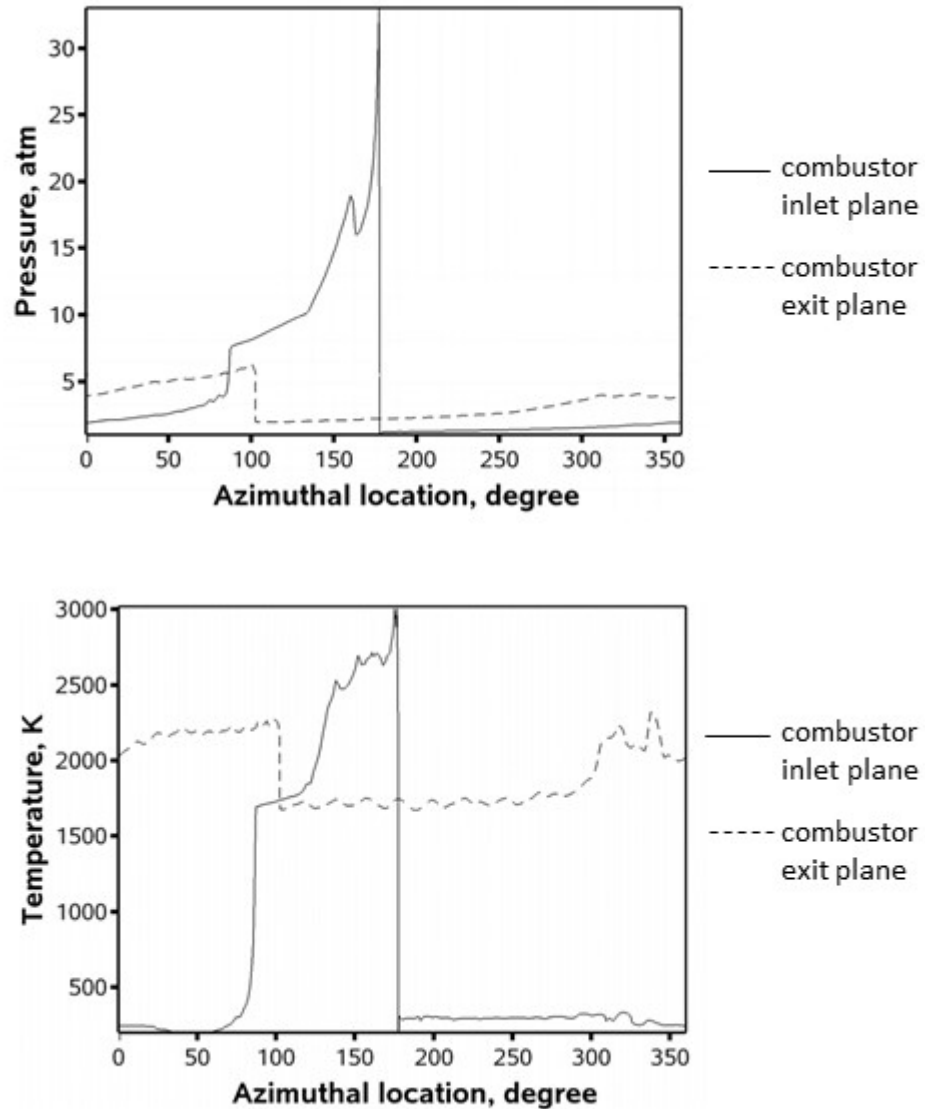
These plots were generated by a simulation of a stoichiometric hydrogen-air RDE operating at 10 atm, 300 K stagnation premixture conditions and 1 atm back pressure.

Figure 28. Inlet (Solid) and Outlet (Dashed) Velocities as a Function of Azimuthal Location for a Generic RDE Simulation. Source: [49].

2. Nonuniform Throat Conditions

The structure of the detonation wave shown in Figure 2 suggests a pressure difference between the region immediately trailing the oblique shock (B) and the region ahead of the oblique shock and downstream of the fill region (F). The region consisting of detonated products from the previous revolution of the detonation wave (F) has a lower pressure than the products in the region behind the oblique shock (C). Figure 29

shows that the exit plane of a generic RDE combustor adopts pressure and temperature distributions which vary azimuthally from a maximum value downstream of the oblique shock to a minimum value just upstream of this oblique shock.



These plots were generated by a simulation of a stoichiometric hydrogen-air RDE operating at 10 atm, 300 K stagnation premixture conditions and 1 atm back pressure.

Figure 29. Inlet (Solid) and Outlet (Dashed) Pressures and Temperatures as a Function of Azimuthal Location for a Generic RDE Simulation.

Source: [49].

It is reasonable to assume the nozzle throat conditions adopt a qualitative structure similar to the structure of the flow through the combustor exit. A qualitative representation of this hypothetical pressure distribution at the throat is shown in the cutaway view of Figure 30, where relative higher pressure regions are represented in red and relative lower pressures are represented in yellow.

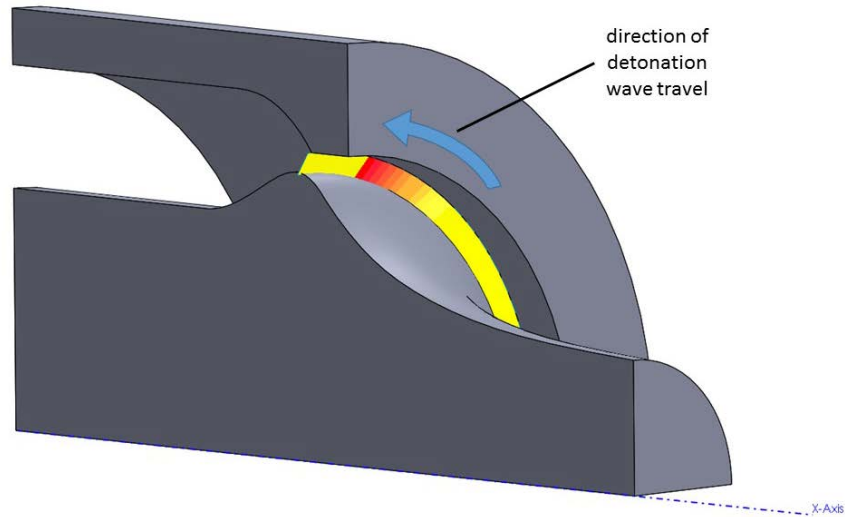


Figure 30. Expected Nonuniform Throat Conditions

The most notable assumption in this work is that the time-averaged flow characteristics over aerospike nozzles operating in RDEs are expected to resemble the steady-state properties for an aerospike operating at some effective pressure ratio.

3. Expected Pressure Ratio

A chamber pressure ratio of approximately 5:1 or 6:1 is characteristic for typical flow rates being run with the NPS RDE at the RPCL [6]. The highest expected nozzle entrance stagnation pressure ratio from the RDE at NPS is approximately 10:1. Thus, it is assumed that the chamber pressure varies azimuthally from approximately 5:1 to 10:1, and that the effective pressure ratio “seen” by the aerospike is within those limits.

4. Ideal Design Pressure Ratio

The ideal design pressure ratio (for a given atmospheric pressure) for the RDE nozzle was assumed to be *equal to or greater than* the maximum expected stagnation pressure ratio along the combustor exit. This would hypothetically yield the following advantages:

a. Altitude Compensation from Overexpanded Conditions

By designing for a chamber pressure *equal to* the maximum expected stagnation pressure, most of the flow will be overexpanded because the maximum pressure at the detonation front is localized to a small region of the chamber cross section at any instant in time. At best, this would result in a small region of the flow being expanded at design conditions and the remaining portion of the flow being overexpanded. Similarly, by designing for a chamber pressure *greater than* the maximum expected stagnation pressure, it is expected that all of the flow will be overexpanded.

As explained previously, the altitude-compensating benefits of aerospike nozzles are realized in the overexpanded flow regime. Thus, assuming a nozzle design pressure ratio for an RDE equal to or greater than the maximum expected pressure ratio would yield the most favorable thrust characteristics by fully capturing the advantages of aerospike nozzles in the overexpanded flow regime.

b. Open Wake Pressure Thrust

Because the flow in this case would always be optimally expanded or overexpanded, the nozzle base region would be experiencing type 1 or type 2 flow. This means that, for constant altitude operation, one would expect the base flow to be in the open wake regime. This is beneficial for constant altitude operation because the base pressure, on average, will be higher than for closed wake flow and close to ambient pressure. Furthermore, research has shown the existence of a subsonic free-stream for the open wake case to cause the base to experience an average pressure higher than ambient [21]. This would be advantageous for subsonic missile applications because it means the nozzle base would contribute to overall thrust.

B. APPLICATION TO THE CURRENT RDE

These assumptions were applied to the RDE at the NPS RPCL to determine the relevant design parameters for the Approximate Method.

1. Determination of Input Parameters

The parameters required as inputs for the Approximate Method are a design pressure ratio and ratio of specific heats.

a. Pressure Ratio

An analysis using the MATLAB code in Appendix A showed that the highest integer design pressure ratio (PR_{design}) possible for the NPS RDE geometry was 44:1. As explained previously, the highest expected local pressure ratio for most air-breathing applications is 10:1. Three design pressure ratios between these two limits were selected as design inputs, yielding three different aerospike nozzle geometries. For CFD purposes, pressure ratios of 10:1, 25:1, and 40:1 were selected to compare steady-state flow characteristics.

For the experimental RDE nozzle, a design pressure ratio of 10:1 was selected in order to balance resolution of the pressure distributions over the nozzle contour and base. The approximate nozzle design method indicates a higher design pressure ratio yields a longer aerospike nozzle, which is more desirable because it allows more pressure taps to be instrumented in the axial direction for increased spatial fidelity. However, a longer aerospike nozzle reduces the nozzle base area, which means that less area is available for instrumentation of pressure taps on the base. The design pressure ratio of 10:1 yielded the geometry most favorable to pressure tap instrumentation.

b. Ratio of Specific Heats

The NASA computer program CEA (Chemical Equilibrium with Applications) calculates chemical equilibrium product compositions from any set of reactants and determines thermodynamic and transport properties for the product mixture [50]. In order to predict the ratio of specific heats of the combustion products, a CEA detonation

problem was run with a mixture of C_2H_4 and an oxidizer composed of air, CO_2 , H_2O , O_2 , and N_2 . The inputs for this run were consistent with the values characteristic of RDE tests at the NPS RPCL. The CEA input and output files are included in Appendix B. This problem resulted in a ratio of specific heats, gamma (γ), value of 1.24 for the burned gas. Thus, a γ value of 1.24 was selected as the design specific heat ratio.

c. Design Exit Mach Number

Using $\gamma = 1.24$ and the three design pressure ratios, and Equations (3)-(6), the design exit Mach numbers were calculated using Equations (7)-(9). Results are shown in Table 1.

d. Transition Pressure Ratio

The analysis conducted in Appendix C uses Equations (2)-(5) to predict the transition pressure ratio (PR_{tr}) for each design pressure ratio. Results are shown in Table 1. This ratio was rounded to the closest integer value.

Table 1. Input Parameters and Calculated Transition Pressure Ratio

PR_{design}	Gamma	Design Exit Mach Number	PR_{tr}
10:1	1.24	2.163	33:1
25:1	1.24	2.684	78:1
40:1	1.24	2.947	129:1

Because all three transition pressure ratios are higher than the maximum expected chamber stagnation pressure of 10:1, the RDE is always expected to operate in the open wake regime. Subsequently, base pressure is assumed to be close to ambient.

2. Computed Results

The parameters were input into the MATLAB script of Appendix A to generate the aerospike nozzle contour using Angelino's approximate method for plug nozzle design. The resultant spike contour for the $PR_{design} = 10:1$ case is shown in Figure 31.

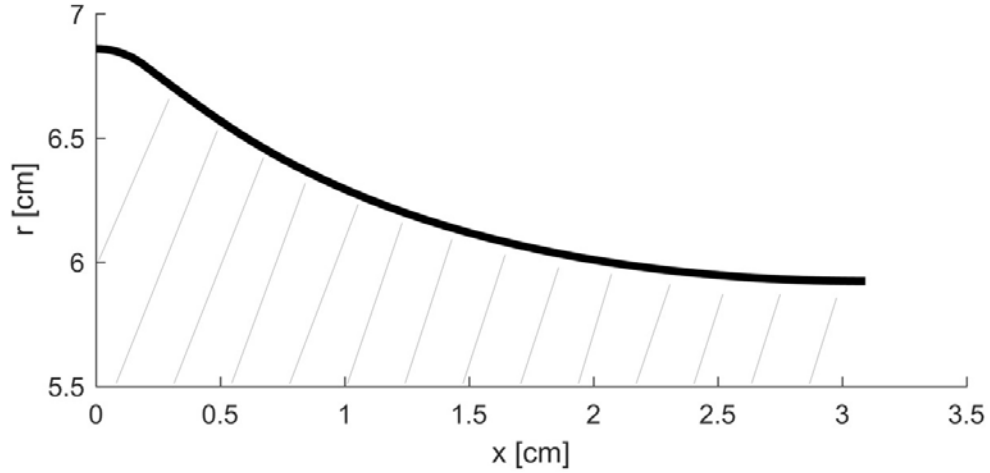


Figure 31. Aerospike Contour for $PR_{\text{design}} = 10:1$

As mentioned previously, the flow direction of the fluid at the throat is equal to the Prandtl-Meyer expansion angle associated with the desired exit Mach number of the nozzle [43]. Thus, the physical nozzle throat area is not normal to the engine centerline, but is inclined by that angle. In order to properly size the throat, a cowl (or shroud) was designed around the spike to minimize the local area at this precise angle. Figure 32 shows the resultant cowl contour for the $PR_{\text{design}} = 10:1$ case.

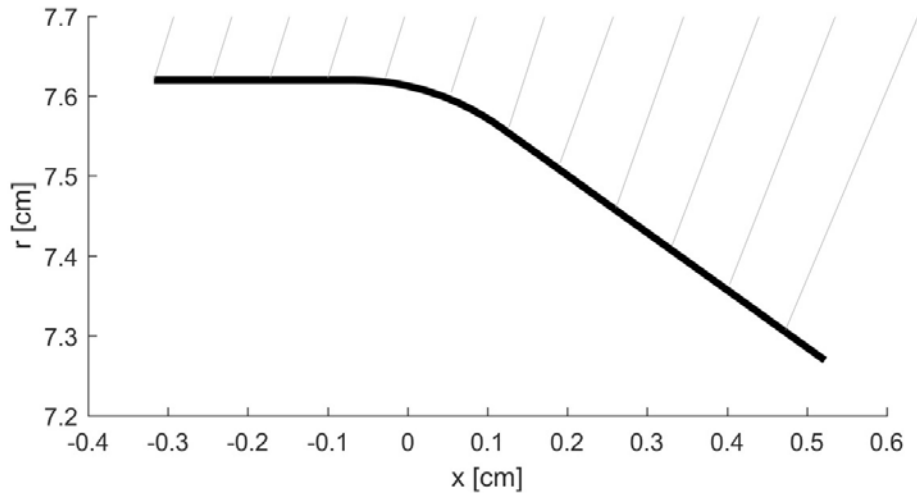


Figure 32. Cowl Contour for $PR_{\text{design}} = 10:1$

The flow must be turned to achieve θ_t at the throat because the flow in the combustion chamber is assumed to possess only an axial component. To minimize losses associated with this turn, both the cowl and spike contours were designed with a 0.318 cm (1/8 inch) fillet radius to achieve this throat angle, as opposed to simply turning the flow around a sharp corner. The slice view of Figure 33 shows the relationship between the contours, throat, and RDE centerline for the 10:1 design pressure ratio.

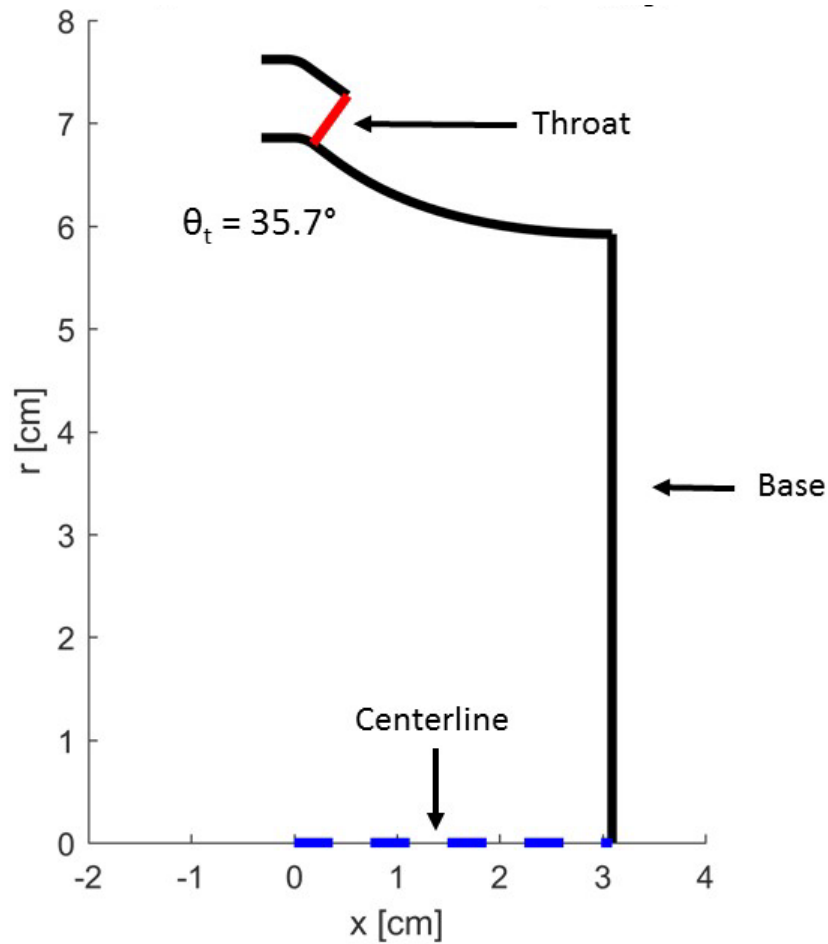


Figure 33. Spike and Cowl Configuration for $PR_{\text{design}} = 10:1$

Figures 34 and 35 show the spike and cowl contours for the $PR_{\text{design}} = 25:1$ and 40:1 designs, respectively, to compare the differences in geometry between these designs.

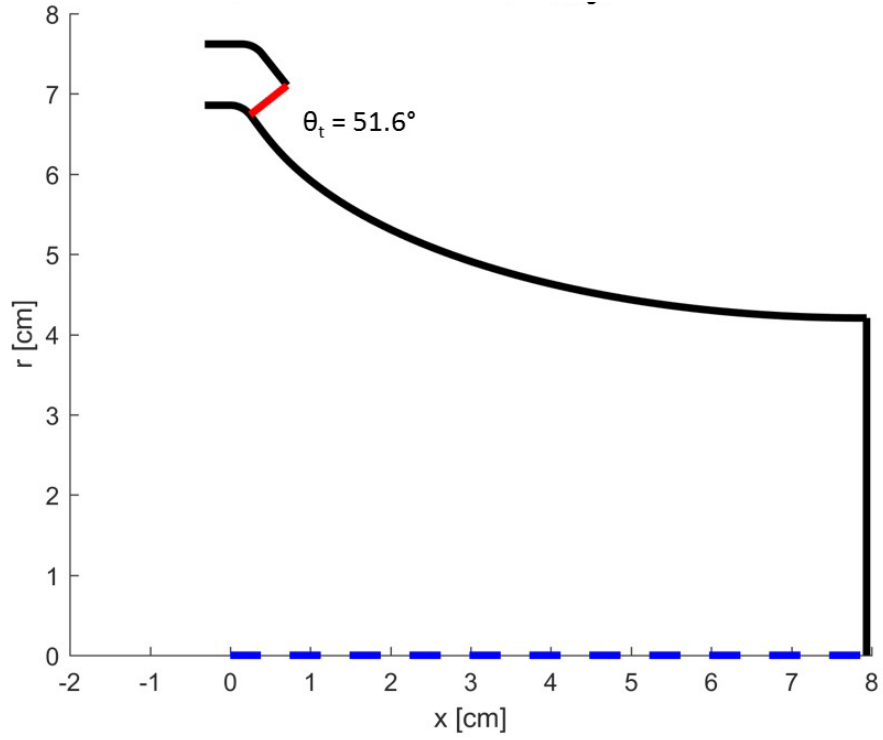


Figure 34. Spike and Cowl Configuration for $PR_{\text{design}} = 25:1$

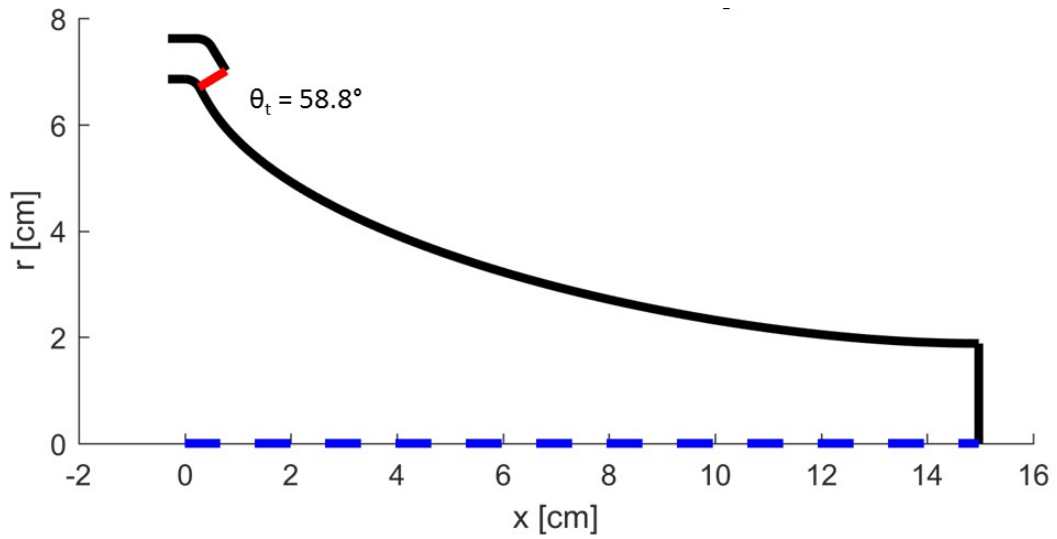


Figure 35. Spike and Cowl Configuration for $PR_{\text{design}} = 40:1$

C. SOLIDWORKS DESIGN

The cowl and plug pieces for the $PR_{\text{design}} = 10:1$ geometry were modeled in SolidWorks by importing the contours and revolving them about the RDE centerline. The pieces were designed to interface with the current RDE hardware.

The cowl connects to the furthest downstream RDE outer ring via six 0.635 cm (1/4 inch) screw clearances, while the nozzle attaches to the RDE center body with a single 0.953 cm (3/8 inch) screw. Seven 0.159 cm (1/16 inch) diameter through-holes were placed along the axial direction of the spike contour. Starting at the throat, they were spaced at 0.318 cm (1/8 inch) intervals and located tangent to the local contour surface. These holes will allow seven capillary tube average pressure (CTAP) probes to be instrumented so pressure distribution along the nozzle can be recorded during RDE operation. On the nozzle base, four additional through-holes were placed at 0.635 cm (1/4 inch) intervals vertically to allow for the base pressure distribution to be determined by CTAP probes. The nozzle and cowl pieces are shown in Figures 36 and 37, respectively.

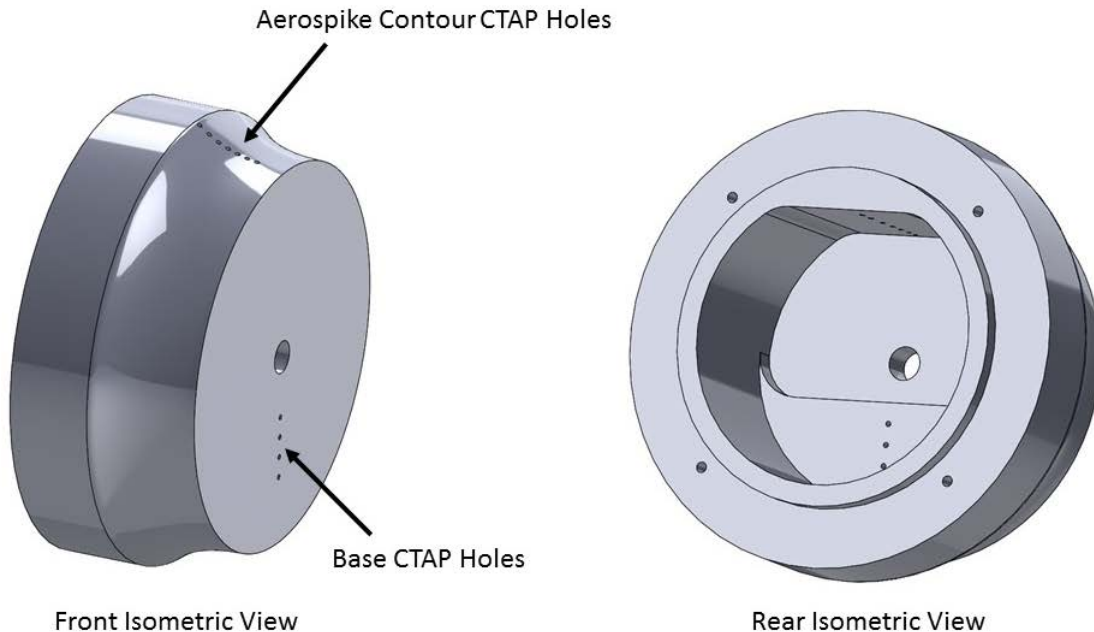


Figure 36. Aerospike SolidWorks Model

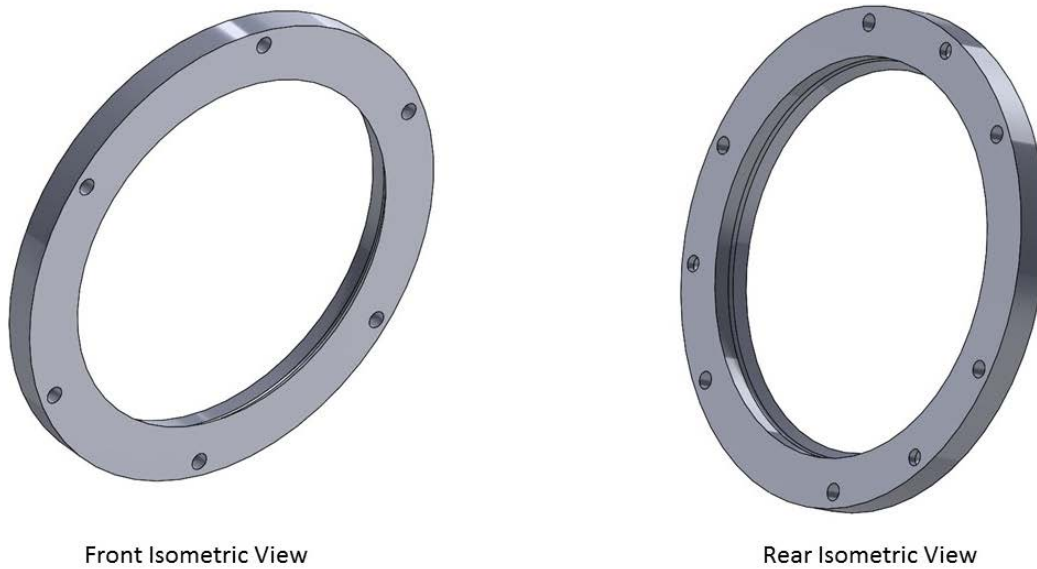


Figure 37. Cowl SolidWorks Model

Additionally, a center body piece was constructed to attach the aerospike to the existing RDE hardware. Four through holes allow the CTAP tubes to be fed back through the center body to a manifold located outside of the RDE system. The center body piece is shown in Figure 38.

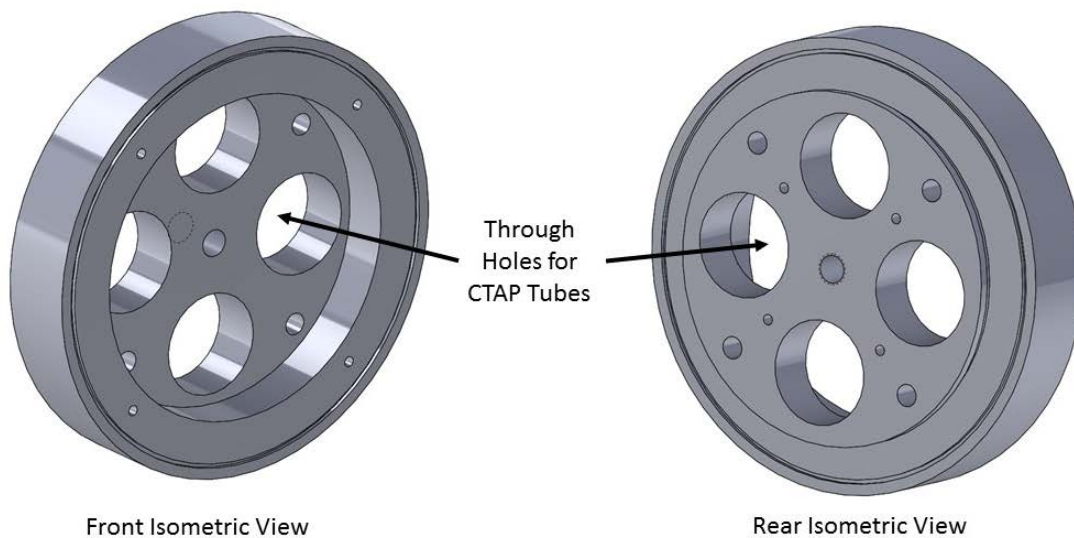


Figure 38. Center Body SolidWorks Model

These parts interface with the existing RDE assembly in the manner shown in Figure 39.

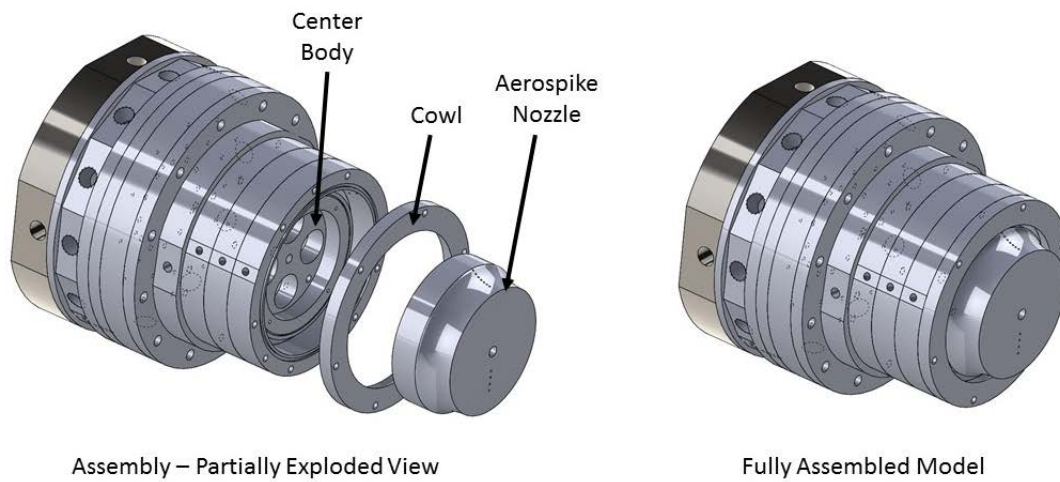


Figure 39. Integration with Current RDE Hardware

THIS PAGE INTENTIONALLY LEFT BLANK

V. CFD ANALYSIS

A. OVERVIEW

Numerical studies were conducted using ANSYS CFX modeling software to approximate nozzle performance. These studies are valuable for multiple reasons. Full-length plug nozzle design makes the assumption of steady flow of an inviscid gas in quiescent air (no external flow), so a steady-state CFD analysis was conducted to validate the geometry developed in the previous section. It was also assumed, for some effective input pressure ratio, steady-state CFD simulations can be used to approximate the time-averaged flow characteristics of the contoured plug nozzle.

Two steady-state simulation types were run: one quiescent air case that approximates experimental conditions, and one case with a supersonic free-stream to model an air-breathing flight vehicle.

B. FLUID DOMAIN

Three fluid domains, corresponding to the three design pressure ratios, were designed in SolidWorks and imported into ANSYS for simulation. The domain corresponding to the 10:1 design pressure ratio is shown in Figure 40. This domain is representative of the experimental nozzle geometry. The two inlet faces correspond to the combustion products and the quiescent air (or supersonic free-stream, depending on the simulation type), shown in red and blue, respectively. Arrows depict the flow paths. In an effort to reduce computational complexity and time, the domain used symmetric boundary conditions to model a 10° slice about the nozzle centerline. The top surface was located 30.48 cm (12 inches) above the centerline, while the outlet plane was located 91.44 cm (36 inches) downstream of the throat. This length was sufficient for the nozzle exhaust flow to be fully-developed by the outlet plane. Corresponding domains were generated for $PR_{\text{design}} = 25:1$ and $40:1$.

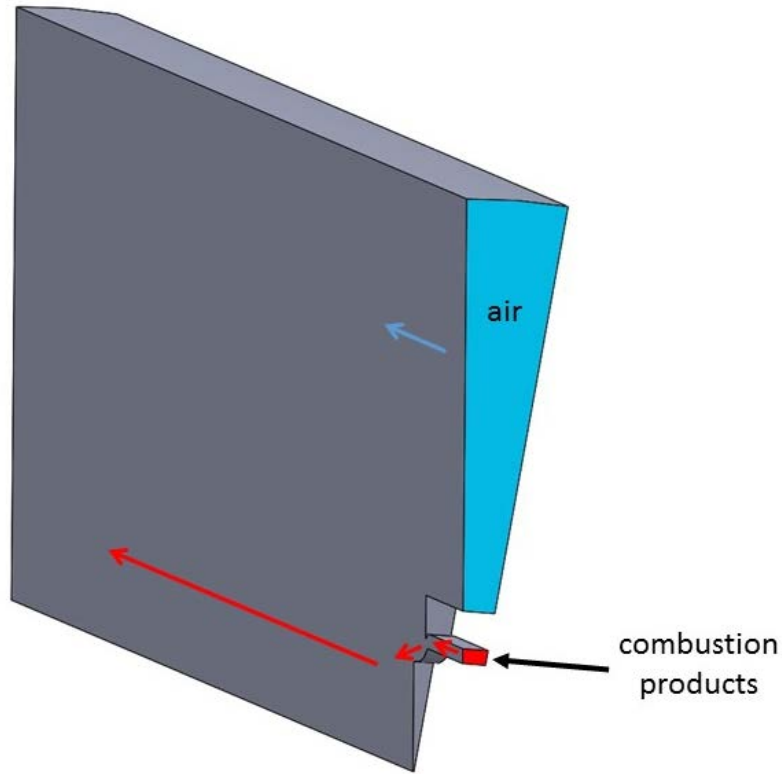


Figure 40. Experimental Fluid Domain Geometry for $PR_{\text{design}} = 10:1$

Because ANSYS CFX does not allow an axis or curved surface to be designated as a symmetric boundary condition, the centerline had to be modified in the domain. The domain was sliced 0.318 cm (1/8 inch) above the physical centerline to create a plane across which the symmetric boundary condition could be enforced. While this is not equivalent to symmetry at the nozzle axis, this was assumed to be a good approximation.

Note that the experimental geometry cowl thickness was 1.91 cm (3/4 inch) in order to properly interface with the existing RDE hardware. Shroud base drag was not taken into consideration for this design.

C. COMPUTATIONAL MESH PARAMETERS

The fluid domains outlined were imported into ANSYS CFX to discretize the volumes into computational meshes. The meshes consisted of general settings for element size, face meshing to ensure identical slices about the centerline, and sweep methods

about the centerline to designate the number of divisions within the 10° slice. Face sizing definitions were included to achieve appropriate grid resolution in areas of interest. The mesh was limited to approximately 3 million elements, balancing sufficient resolution to capture flow characteristics with computational time. A mesh sensitivity analysis (presented in a following section) determined this resolution was sufficient for the important flow properties to have converged.

1. Common Mesh Settings

The ANSYS mesh settings common for all simulations are outlined in Table 2.

Table 2. Common Mesh Settings

Parameter	Setting
Sizing	
Size Function	Curvature
Relevance Center	Fine
Initial Size Seed	Active Assembly
Smoothing	Medium
Transition	Slow
Span Angle Center	Fine
Curvature Normal Angle	Default (18.0 °)
Min Size	Default (1.5137e-004 m)
Max Face Size	Default (1.5137e-002 m)
Max Tet Size	Default (3.0274e-002 m)
Growth Rate	1.10
Automatic Mesh Based Defeaturing	On
Defeature Size	Default (7.5684e-005 m)
Minimum Edge Length	5.5344e-004 m
Inflation	
Use Automatic Inflation	None
Inflation Option	Smooth Transition
Transition Ratio	0.77
Maximum Layers	10
Growth Rate	1.1
Inflation Algorithm	Pre
View Advanced Options	No

2. Face Sizing and Meshing

Face sizing, face meshing, and a sweep method were employed to obtain a symmetric mesh with high resolution around critical features of the geometry.

a. Face Sizing

Face sizing was employed on the wall boundaries to capture the grid resolution desired to obtain higher fidelity of the flow characteristics. This permits a finer mesh around critical features of the fluid domain while allowing the regions of less interest a much coarser mesh. Two separate face sizing functions were used. The first was applied to the nozzle base, plug contour, and leading edges of the cowl. A nominal element size of 2.54×10^{-5} meters (0.001 inches) was prescribed for these faces. The second function was applied to the inlet and combustion chamber channel walls leading up to the plug. A nominal element size of 2.54×10^{-4} meters (0.01 inches) was prescribed for these faces.

b. Face Meshing and Sweep Method

Face meshing was employed to several faces to ensure mesh symmetry about the nozzle centerline. A sweep method was employed between the left and right sides of the domain to obtain 20 slices about the nozzle centerline. This ensures a resolution of 0.5° per slice. An overview of the domain mesh for the $PR_{\text{design}} = 10:1$ case is shown in Figure 41.

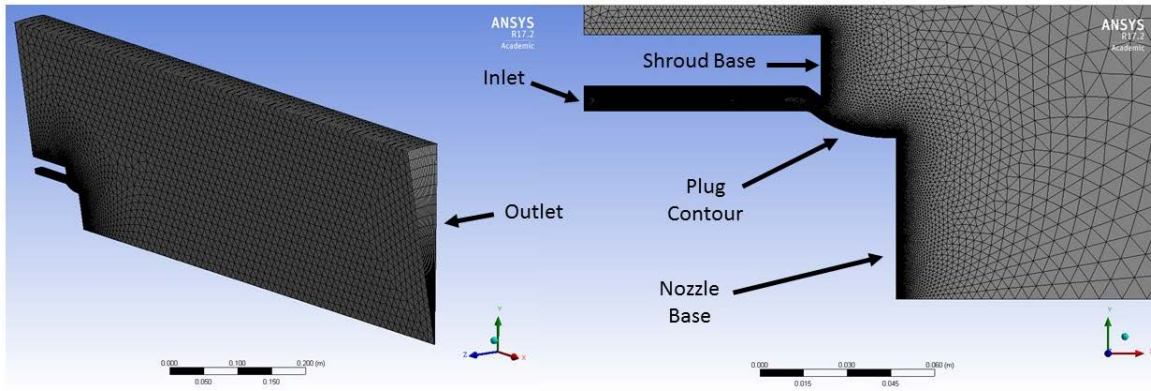


Figure 41. ANSYS Domain Mesh for $PR_{\text{design}} = 10:1$

D. CFD ASSUMPTIONS

To simplify the computational process, the following assumptions were made:

1. Non-Reacting Flow Modeled as Combustion Products

All simulations made the assumption of non-reacting flow, where the properties of the simulated working fluid were representative of the combustion gases expanding through the nozzle. The assumption is justified because combustion can be assumed to be complete a significant distance downstream of the detonation. In the RDE, the throat will be located 0.116 meters (4.57 inches) downstream of the injection plane, which is assumed to be a sufficient distance for the products to have reached equilibrium.

By the combustor exit, the detonation product composition is typically close to those associated with a deflagration of the same reactants. The assumption of products resulting from a deflagration is reasonable in this case because the nozzle is located several inches downstream from the mixer.

At the combustor exit, the detonation product composition was approximated with deflagration products produced by reactants at the same conditions. For subsonic flow in a combustor, γ and molecular weights of deflagrations are sufficient to approximate the properties of detonation products. Figure 42 shows that variability of pressure and temperature with γ (here, k) in the subsonic regime is quite small, so slight inaccuracies in γ will not significantly affect simulation results, especially for nozzles with low expansion ratios. Furthermore, the maximum Mach number expected for the simulated nozzles is 2.163. Figure 42 shows that flow properties do not diverge significantly with γ until Mach 10 is reached.

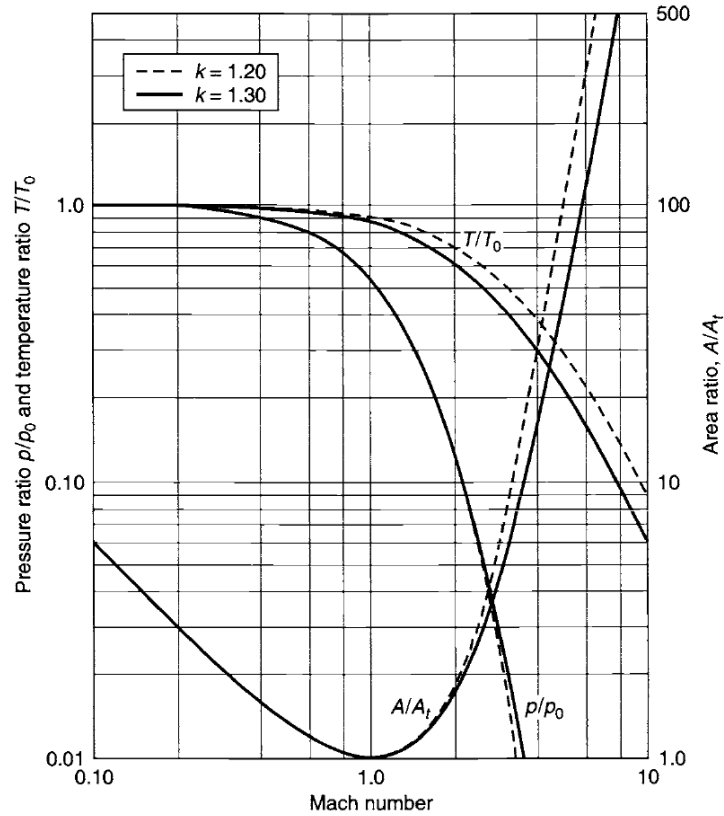


Figure 42. Variability of Properties with Ratio of Specific Heats.
Source: [10].

By simulating typical rocket problems in CEA, the most significant product species, in terms of mass fraction, could be determined. Thus, the combustion products were modeled as mixtures of the product species with significant concentrations as determined by CEA constant-pressure combustion models.

Two CEA rocket problems were conducted to determine the composition of the combustion products. The RDE at the NPS RPCL typically detonates hydrogen or hydrocarbon fuels in air, so the first CEA run assumed stoichiometric combustion of hydrogen (H_2) and air, while the second assumed stoichiometric combustion of ethylene (C_2H_4) and air. The associated input and output files are included in Appendix D. The three largest product constituents for both CEA runs, on a mass basis, are shown in Table 3. In ANSYS, the combustion products were modeled as mixtures of these three largest constituents at the resulting chamber temperature. Because small amounts of the trace

species were ignored, the combustion products in ANSYS rounded the constituents on a mass basis. These approximations are also shown in Table 3.

Table 3. CEA Results and ANSYS Approximations

H₂ / Air Rocket Problem							
P [atm]	T [K]	Mass Fraction Ar		Mass Fraction H₂O		Mass Fraction N₂	
		CEA	ANSYS	CEA	ANSYS	CEA	ANSYS
2.5	2406.69	0.01255	0.01	0.24123	0.25	0.73246	0.74
5	2424.52	0.01255	0.01	0.24301	0.25	0.73254	0.74
7.5	2433.89	0.01255	0.01	0.24395	0.25	0.73258	0.74
10	2440.09	0.01255	0.01	0.24459	0.25	0.73262	0.74
12.5	2444.64	0.01255	0.01	0.24505	0.25	0.73265	0.74
15	2448.2	0.01255	0.01	0.24542	0.25	0.73267	0.74
C₂H₄ / Air Rocket Problem							
P [atm]	T [K]	Mass Fraction N₂		Mass Fraction CO₂		Mass Fraction H₂O	
		CEA	ANSYS	CEA	ANSYS	CEA	ANSYS
2.5	2400.01	0.70567	0.7	0.17248	0.2	0.07775	0.1
5	2421.42	0.70573	0.7	0.17572	0.2	0.07826	0.1
7.5	2433.08	0.70577	0.7	0.17752	0.2	0.07854	0.1
10	2440.96	0.7058	0.7	0.17875	0.2	0.07872	0.1
12.5	2446.85	0.70582	0.7	0.17967	0.2	0.07886	0.1
15	2451.51	0.70585	0.7	0.18041	0.2	0.07897	0.1

2. Uniform Inlet Flow in the Radial and Circumferential Directions

Additionally, flow was assumed to have constant properties across the inlet plane in the radial direction. Because the radial dimension is typically small compared to the azimuthal and axial dimension, there is generally little variation radially within the flow [49]. This assumption is reasonable for the RDE at NPS because the channel height, or distance between the inner and outer chamber rings, is 7.62e-3 meters (0.3 inches), which was assumed to be small enough to neglect variation in the radial direction.

Inlet properties were also assumed to be constant in the circumferential direction. While the RDE flow field varies azimuthally, these CFD simulations seek to model the constant effective pressure ratio “seen” by the nozzle.

E. SOLVER DEFINITION AND BOUNDARY CONDITIONS

The top of the domain was specified as an opening at 1 atm, and an average static pressure of 1 atm was specified at the outlet. Symmetry was imposed on both sides of the domain as well as the thin slice near the nozzle centerline. Figure 43 illustrates the boundary conditions specification for the $PR_{\text{design}} = 10:1$ case. The other domains utilized the same boundary conditions.

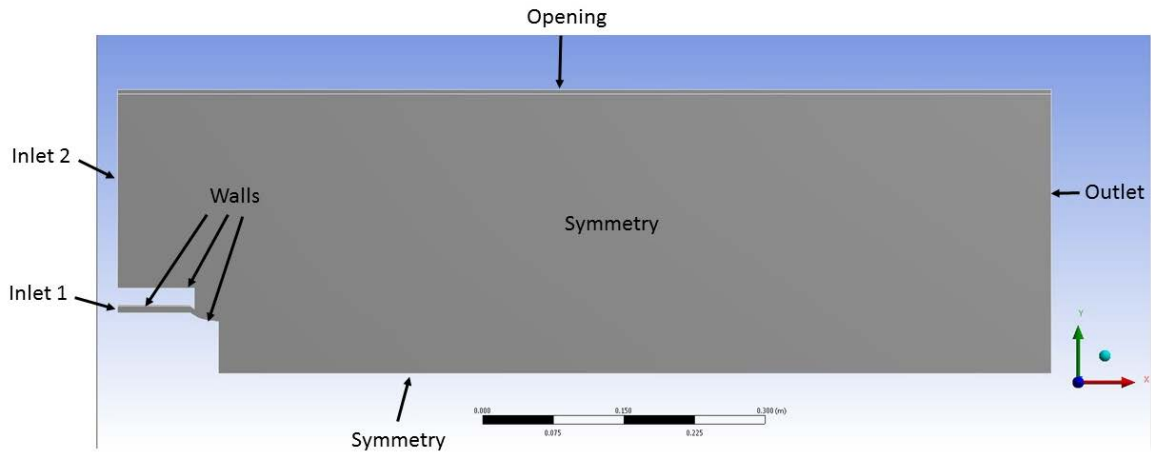


Figure 43. Boundary Conditions for the $PR_{\text{design}} = 10:1$ Case

The solver parameters are outlined in Table 4 for the $PR_{\text{design}} = 10:1$, C_2H_4 case in quiescent air at a pressure ratio of 10:1. All other simulations maintained the same settings, varying only the inlet conditions according to Table 3.

Table 4. Solver Parameters

Parameter	Setting
Analysis Type	
Analysis Type	Steady-State
Default Domain	
Type	Fluid
Fluid Definition	Products: Material Library, Continuous Fluid
Buoyancy Model	Non Buoyant
Domain Motion	Stationary
Reference Pressure	0.0 [atm]
Component Models	Air Ideal Gas (Constraint)
	CO ₂ (Transport Equation)
	H ₂ O (Transport Equation)
	N ₂ (Transport Equation)
Heat Transfer Model	Total Energy, Include Viscous Work Term
Turbulence Model	k epsilon
Turbulent Wall Functions	Scalable, High Speed Model Off
Combustion Products Inlet	
Type	INLET
Component	CO ₂ : Mass Fraction: 0.2
	H ₂ O: Mass Fraction: 0.1
	N ₂ : Mass Fraction: 0.7

Flow Direction	Normal to Boundary Condition
Flow Regime	Subsonic
Heat Transfer	Total Temperature: 2441.0 [K]
Mass And Momentum	Total Pressure (Relative): 10.0 [atm]
Turbulence	Zero Gradient
Quiescent Air Inlet	
Type	INLET
Component	CO ₂ : Mass Fraction: 0.0
	H ₂ O: Mass Fraction: 0.0
	N ₂ : Mass Fraction: 0.0
	Air Ideal Gas: Constraint
Flow Direction	Zero Gradient
Flow Regime	Subsonic
Heat Transfer	Static Temperature: 290.0 [K]
Mass And Momentum	Static Pressure (Relative): 1.0 [atm]
Turbulence	Zero Gradient
Opening	
Type	OPENING
Component	CO ₂ : Mass Fraction: 0.0
	H ₂ O: Mass Fraction: 0.0
	N ₂ : Mass Fraction: 0.0
	Air Ideal Gas: Constraint
Flow Direction	Normal to Boundary Condition
Flow Regime	Subsonic
Heat Transfer	Opening Temperature: 290.0 [K]
Mass And Momentum	Static Pressure and Direction: Relative Pressure: 1.0 [atm]

Turbulence	Zero Gradient
Outlet	
Type	OUTLET
Flow Regime	Subsonic
Mass And Momentum	Average Static Pressure
Pressure Profile Blend	0.05
Relative Pressure	1.0 [atm]
Pressure Averaging	Average Over Whole Outlet
Symmetry: Left, Right, Bottom	
Type	SYMMETRY
Walls	
Type	WALL
Heat Transfer	Adiabatic
Mass And Momentum	No Slip Wall
Wall Roughness	Smooth Wall

F. TEST MATRIX

In summary, the test matrix for all CFD simulations is shown in Table 5.

Table 5. Test Matrix

Run Number	Design Pressure Ratio	Case	Fuel	Simulated Pressure Ratio
1	10:1	Quiescent Air	H ₂	2.5:1
2	10:1	Quiescent Air	H ₂	5:1
3	10:1	Quiescent Air	H ₂	7.5:1
4	10:1	Quiescent Air	H ₂	10:1
5	10:1	Quiescent Air	H ₂	12.5:1
6	10:1	Quiescent Air	H ₂	15:1
7	10:1	Quiescent Air	C ₂ H ₄	2.5:1
8	10:1	Quiescent Air	C ₂ H ₄	5:1
9	10:1	Quiescent Air	C ₂ H ₄	7.5:1
10	10:1	Quiescent Air	C ₂ H ₄	10:1
11	10:1	Quiescent Air	C ₂ H ₄	12.5:1
12	10:1	Quiescent Air	C ₂ H ₄	15:1
13	25:1	Quiescent Air	H ₂	2.5:1
14	25:1	Quiescent Air	H ₂	5:1
15	25:1	Quiescent Air	H ₂	7.5:1
16	25:1	Quiescent Air	H ₂	10:1
17	25:1	Quiescent Air	H ₂	12.5:1
18	25:1	Quiescent Air	H ₂	15:1
19	40:1	Quiescent Air	H ₂	2.5:1
20	40:1	Quiescent Air	H ₂	5:1
21	40:1	Quiescent Air	H ₂	7.5:1
22	40:1	Quiescent Air	H ₂	10:1
23	40:1	Quiescent Air	H ₂	12.5:1
24	40:1	Quiescent Air	H ₂	15:1
25	10:1	Supersonic Free-Stream	H ₂	10:1

VI. CFD RESULTS

A. QUIESCENT AIR

The first set of ANSYS simulations attempted to model the expected experimental conditions at the NPS RPCL. Twelve quiescent air ANSYS simulations (run numbers 1–12 of Table 5) were conducted, on the 10:1 design pressure ratio geometry. Inlet total pressure was varied from 2.5 atm to 15 atm, ensuring overexpanded, on-design, and underexpanded conditions. The constituents of the working fluid alternated between those produced by the combustion of hydrogen in air and ethylene in air, according to Table 3.

The second set of simulations varied the nozzle geometry (run numbers 13–24 of Table 5). The same inlet total pressure values (2.5 atm through 15 atm) were applied to the domains corresponding to $PR_{\text{design}} = 25:1$ and $40:1$. Because the inlet conditions (for an ambient pressure of 1 atm) were less than the design pressure ratios for these nozzles, the flow was always overexpanded. The working fluid for these simulations was the products generated by combustion of hydrogen in air.

All simulations were for steady-state conditions, which is not representative of RDE operation. However, the results are valuable for several reasons. First, they validate the nozzle design technique by providing a means to illustrate the nozzle's operation under ideal conditions. Second, they provide a means to predict the effects of different fuel types and geometries. Furthermore, it is expected that within the range of simulated pressure ratios, there exists some effective pressure ratio over which the time-averaged properties of the unsteady flow field can be approximated by a steady-state solution.

1. Nondimensional Wall Distance and Turbulence Modeling

The average y^+ along the plug surface for the quiescent air simulations was 17.93. The maximum y^+ at any point on the plug surface for these simulations was 61.08, which is sufficient for the standard form of the k-epsilon turbulence model.

Additionally, because the k-epsilon model has been shown to perform poorly at the wall, the shear stress transport (SST) model was used in one simulation to examine the sensitivity of the results to the turbulence model. Results are presented in a later section.

2. Validation of the Experimental Nozzle Design

The following results apply to the 10:1 design pressure ratio nozzle geometry. They validate the nozzle design technique because they successfully reproduce the design input parameters.

a. Ratio of Specific Heats, Gamma

For the steady-state simulations, the ratio of specific heats, γ , was averaged along the plug surface for all 6 pressure ratios and both fuel types. The maximum γ was 1.248 and the minimum γ was 1.245. The average γ for all trials was computed as 1.247. This validates the design γ value of 1.24 because it corresponds to a 0.565% error.

b. Design Exit Mach Number

Figure 44 plots the Mach number along the exit plane for all pressure ratios for the hydrogen fuel case. The y-axis values extend from $r = 5.715$ cm (2.25 inches) just below the nozzle lip (at 5.922 cm) to $r = 9.525$ cm (3.75 inches) at the outside edge of the shroud.

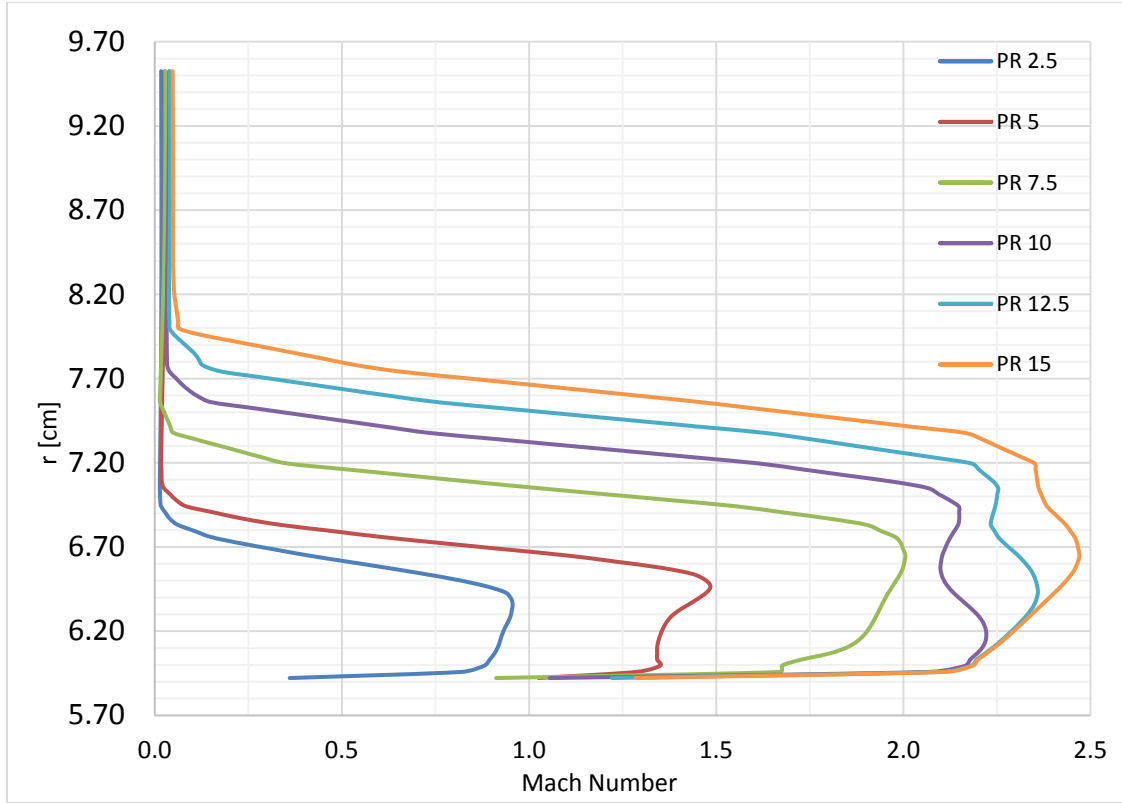


Figure 44. Mach Number Distribution along the Nozzle Exit Plane at Various Pressure Ratios for the Quiescent Air Hydrogen Fuel Case, $PR_{\text{design}} = 10:1$

This validates the nozzle design because for on-design and underexpanded conditions (PR 10:1, 12.5:1, and 15:1), the average exit Mach number just outside of the boundary layer at the nozzle lip 9.525 cm (3.75 inches) was 2.177. This equates to a 0.647% error from the design exit Mach number of 2.163. Physically, this corresponds to the expansion wave carrying the exit design conditions impinging on the nozzle lip.

The overexpanded conditions simulated also display expected distributions. For these conditions, the exit Mach number at $r = 5.922$ cm decreased from 1.675 to 0.879 as pressure ratio decreased. The Mach number variation at the exit plane can be seen to vary with increasing distance from the nozzle lip due to the reflection of expansion waves from the nozzle contour that originated from the nozzle lip. Compression waves from the nozzle contour and reflected from the shear layer further alter the Mach number profile in the flow region.

3. Steady-State Pressure Distribution along the Aerospike

Figure 45 shows the nondimensional computed pressure distribution for all pressure ratios for the hydrogen fuel case, 10:1 pressure ratio design. For all cases, the sharp drop in pressure at approximately $X/L = 0.06$ corresponds to the location of the nozzle throat.

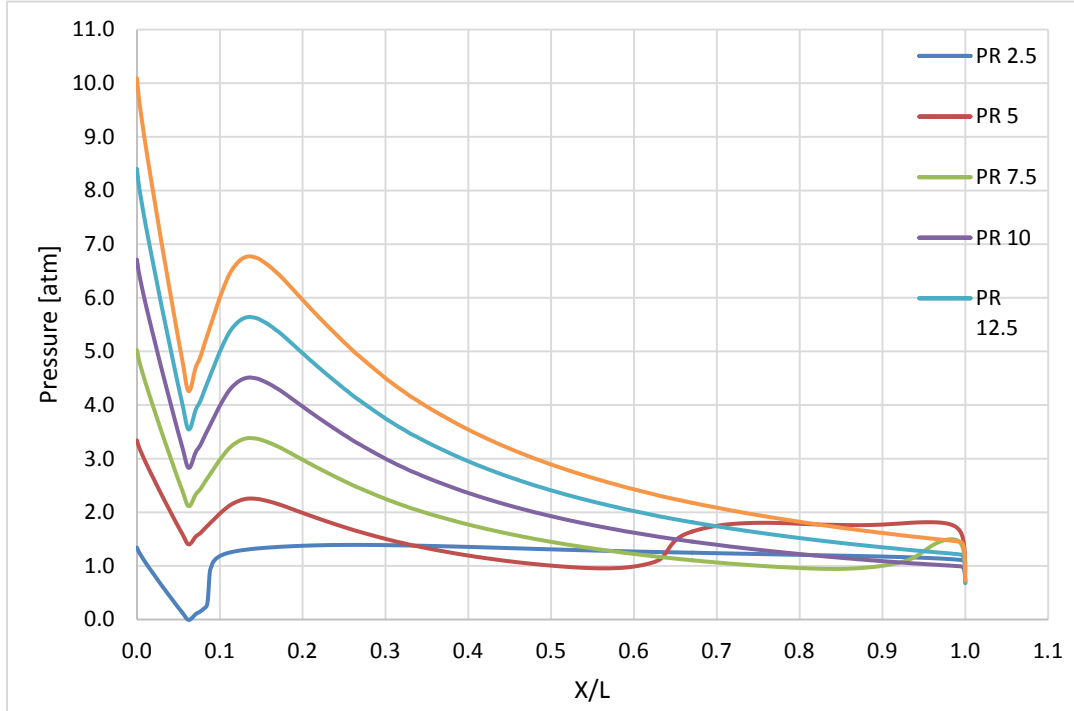


Figure 45. Steady-State Nozzle Pressure Distribution at Various Pressure Ratios for the Quiescent Air Hydrogen Fuel Case, $PR_{\text{design}} = 10:1$

Figure 45 does not show the characteristic oscillating pressure distributions associated with type 1 overexpanded flows (such as Figure 18 (a)). Flow in the type 1 regime would be marked by intense wave interactions on the plug surface. Only the PR 5:1 case shows the beginnings of such interaction between the compression and expansion waves with the shear layer, as indicated by the pressure increase and subsequent plateau at approximately $x = 0.65$. This suggests that, for the simulated pressure ratios, the spike is operating closer to the type 2 regime, where the majority of

the plug is under the characteristic lines of the expansion fan. For the PR 2.5:1 case, note the compression waves coalesce into a normal shock at approximately $X/L = 0.08$, which is detrimental to performance.

This result is significant because it suggests that a higher design pressure ratio can be afforded, and as a result, a different design approach may be beneficial. Rather than selecting a design pressure ratio equal to the maximum expected pressure ratio from the detonation across any small azimuthal range, an artificially higher design pressure could be selected. Although this would guarantee completely overexpanded operation for all pressure ratios, altitude compensating characteristics in type 1 flow would prevent significant thrust loss. Such a design would be beneficial because it would yield a longer nozzle, a smaller nozzle base, and guarantee the preservation of open-wake flow.

The simulations for the $PR_{\text{design}} = 25:1$ and 40:1 nozzles illustrate this idea. Figures 46 and 47 plot the computed pressure distributions for these geometries, respectively.

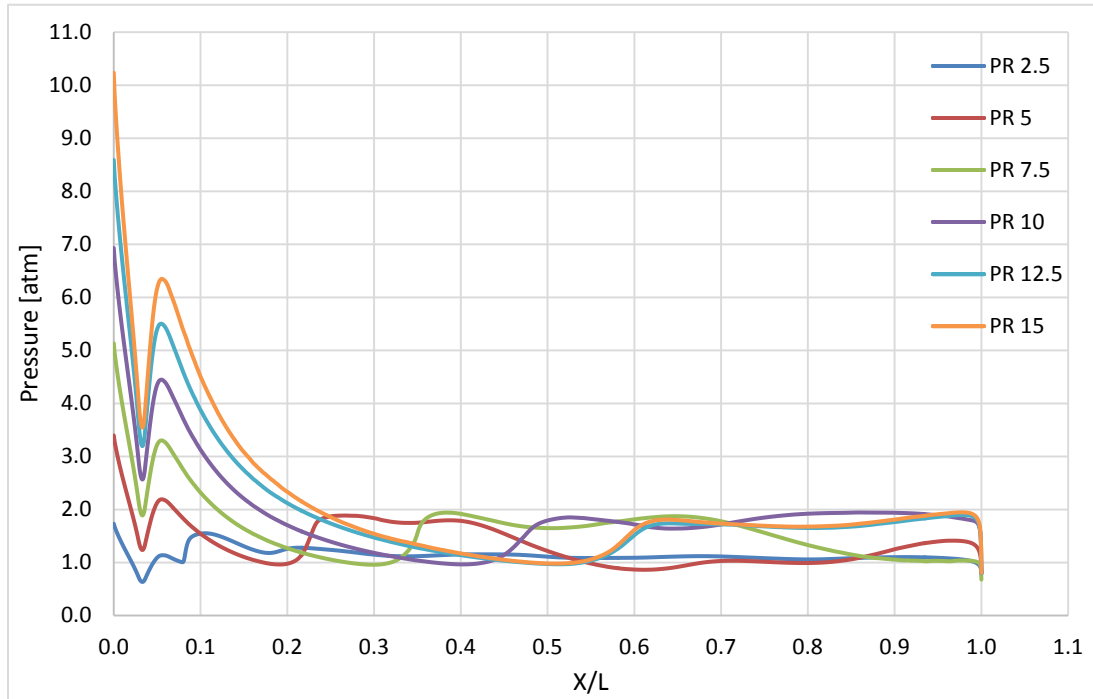


Figure 46. Steady-State Nozzle Pressure Distribution at Various Pressure Ratios for the Quiescent Air Hydrogen Fuel Case, $PR_{\text{design}} = 25:1$

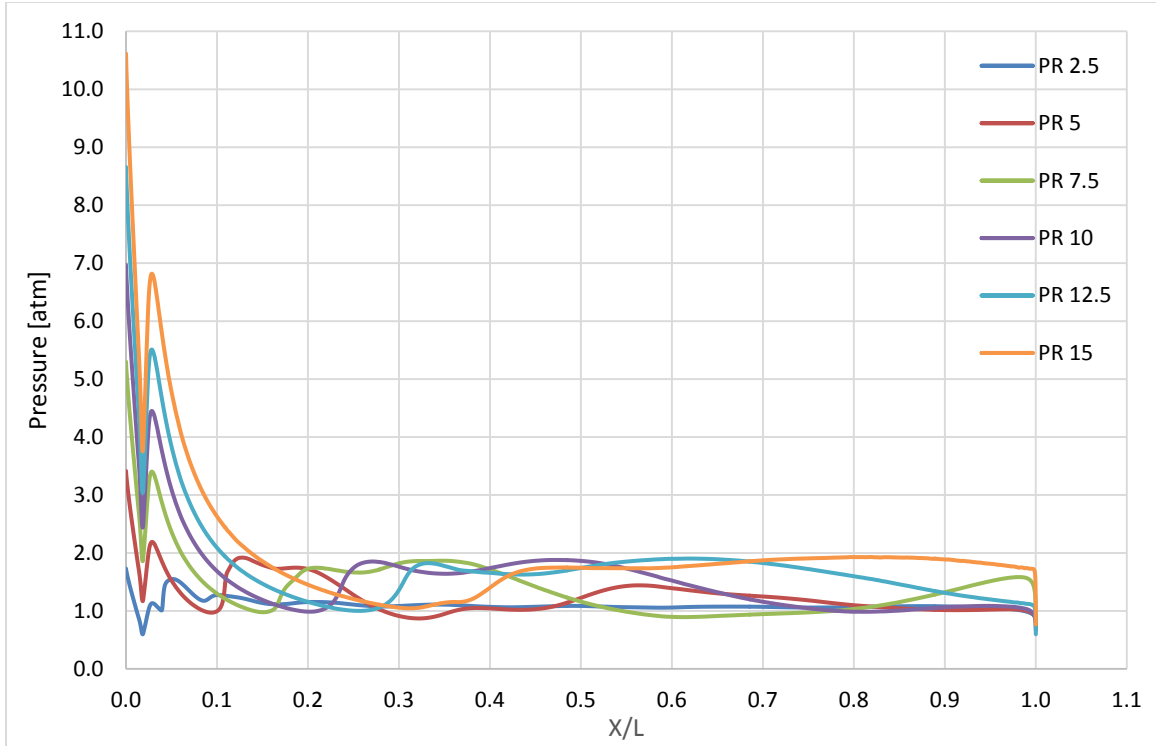


Figure 47. Steady-State Nozzle Pressure Distribution at Various Pressure Ratios for the Quiescent Air Hydrogen Fuel Case, $PR_{\text{design}} = 40:1$

Note the characteristic oscillating pressure distributions along the nozzle contours for Figures 46 and 47. This suggests type 1 operation.

4. Steady-State Base Pressure Distribution

The computed base pressure distribution for all pressure ratios for $PR_{\text{design}} = 10:1$, hydrogen-air case is shown in Figure 48.

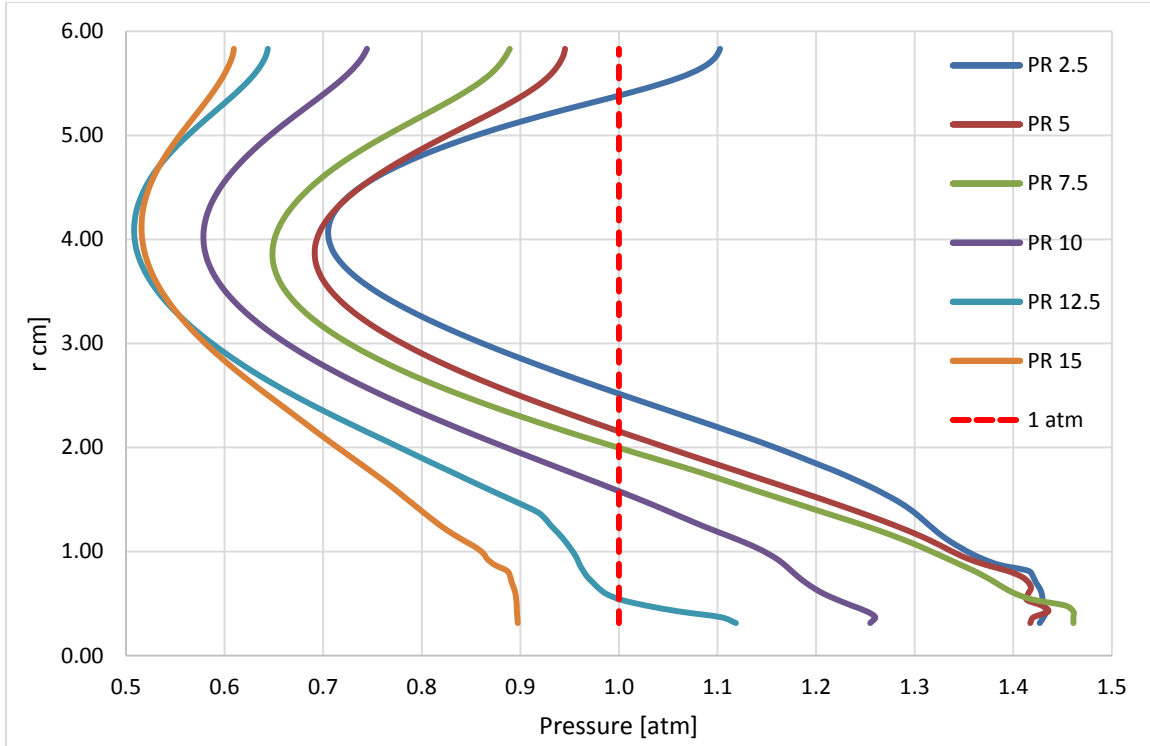


Figure 48. Steady-State Base Pressure Distribution at Various Pressure Ratios for the Quiescent Air Hydrogen Fuel Case, $PR_{\text{design}} = 10:1$

As explained previously, present day computational tools are limited in their ability to compute plug nozzle base flows. Figure 48 shows that base pressure is nonuniform with radius and is generally less than atmospheric pressure. These somewhat inaccurate results are consistent with those found in the literature ([33], [34], [38]). Because CFD has been shown to underpredict the base pressure and overpredict pressure variation with radius for most pressure ratios, the experimental pressure distribution is expected to be closer to atmospheric pressure and fairly uniform with base radius.

5. Steady-State Thrust Computation

In order to predict the gross thrust generated by the RDE, a control volume was defined with six surfaces as shown in Figure 49. This figure overlays the control surfaces on a cutaway view of the entire RDE.

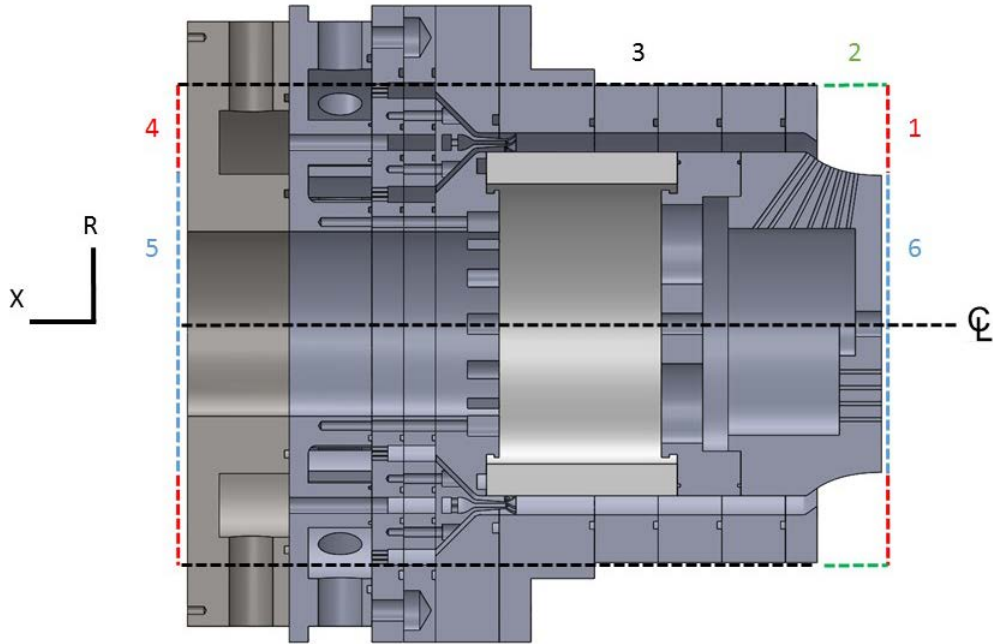


Figure 49. Designation of the RDE Control Volume

Because air enters the engine radially, the flux of air through control surface 3 can be ignored. Additionally, because control surface 2 extends completely around the centerline, the radial component of force can be neglected, and only the x-component is of concern.

The net force on the control volume can be computed by evaluating the momentum flux and pressure forces on the control surfaces that comprise this control volume. When applied to a particular surface, the ANSYS force function calculator computes the force on that surface in the specified direction due to pressure and advection of momentum. The force function was applied in the x-direction to surfaces 1, 2, and 6, as shown in Figure 50.

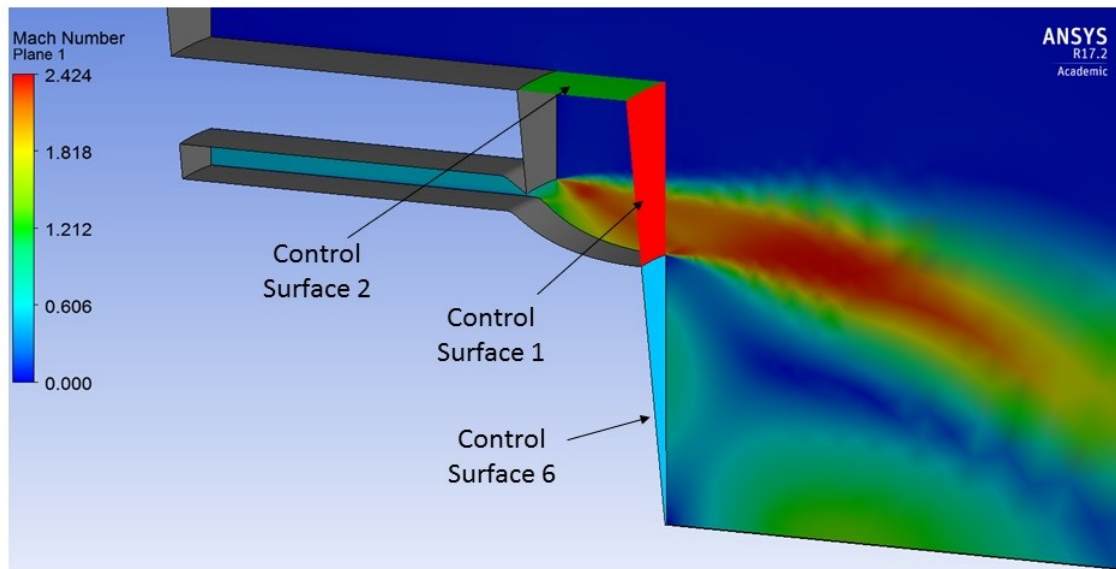


Figure 50. Control Surfaces Over Which ANSYS Force Function Was Applied in the X-Direction, $PR_{\text{design}} = 10:1$

By subtracting the atmospheric pressure force on the corresponding opposite faces of surfaces 1 and 6, (control surfaces 4 and 5 of Figure 49, respectively), the thrust contribution can be determined for each control surface. These contributions are shown in Figure 51 for the hydrogen and ethylene fuel cases for the $PR_{\text{design}} = 10:1$ nozzle simulation. The contributions labeled “Momentum Flux 1” come from the force computed in the axial direction on control surface 1 in Figure 50, and the contributions labeled “Momentum Flux 2” come from the force computed in the axial direction on control surface 2 in Figure 50. The contribution labeled “Base Drag” comes from the force computed in the axial direction on control surface 6 in Figure 50. Computations show that the nozzle base exerts a significant drag force because the integrated pressure is less than ambient. This is assumed to be inaccurate due to the aforementioned shortcomings of CFD in predicting nozzle base flow.

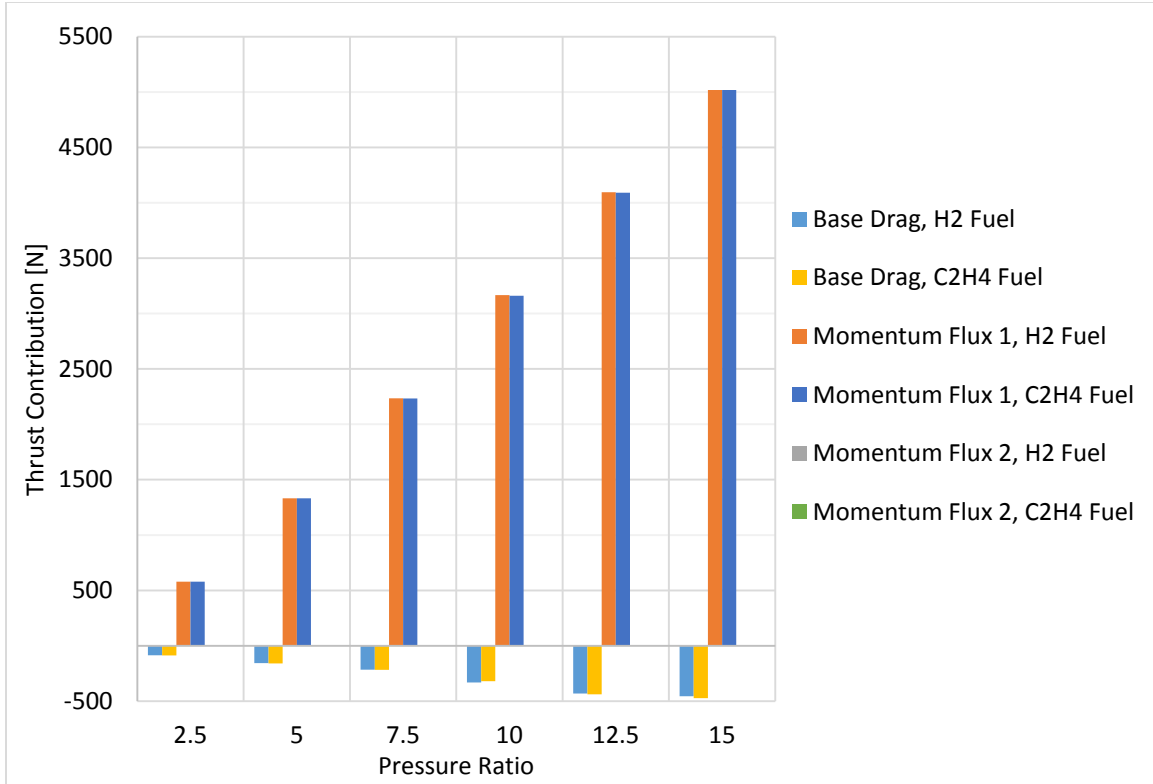


Figure 51. Thrust Contribution for Control Surfaces 1, 2, and 6 for the Quiescent Air Hydrogen and Ethylene Fuel Cases, $PR_{\text{design}} = 10:1$

Figure 51 shows that for the $PR_{\text{design}} = 10:1$ simulations, the difference in thrust between the two fuel cases was negligible. This result is assumed to hold for the $PR_{\text{design}} = 25:1$ and $40:1$ cases, so only the H_2 fuel case was simulated for those designs.

Figure 51 also shows that the nozzle base exerts a drag force on the control volume. As explained previously, CFD is limited in its ability to predict these base flows. The analysis provided in Appendix C shows that the transition pressure ratio at which the wake changes from open to closed is $33:1$. Because the RDE will never exceed a pressure ratio of $10:1$ at any sector about the centerline, the nozzle base should always be operating in the open wake regime. Assuming the base is operating in the open wake regime for these pressure ratios, it is reasonable to expect atmospheric pressure to prevail over the base surface. Thus, the base would not be contributing to or detracting from overall thrust, and can be neglected in force computations.

Additionally, Figure 51 shows that the contribution from control surface 2 (labeled “Momentum Flux 2”) is negligible compared to the contributions from the base and control surface 1. As a result, the gross thrust can be estimated by the contribution of control surface 1 alone. Figure 52 shows the gross thrust from Momentum Flux 1 for the H₂ fuel case for all three nozzles.

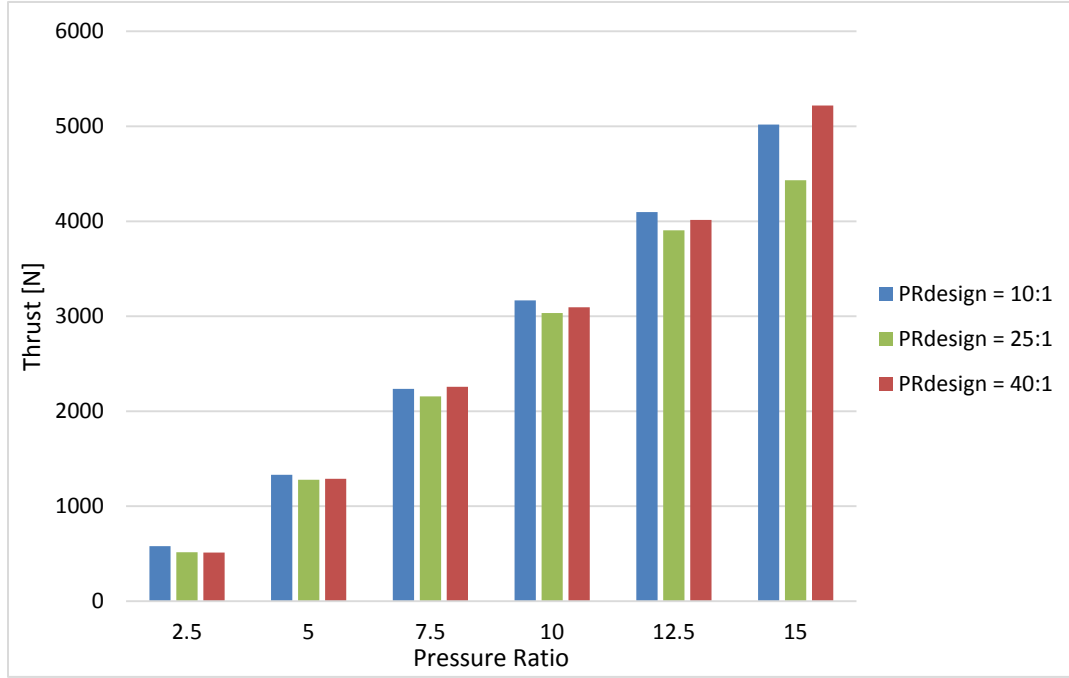


Figure 52. Gross Thrust vs Pressure Ratio for H₂ Fuel Case

6. Steady-State Thrust Coefficient

Thrust coefficient is generally computed as:

$$C_f = \frac{F}{p_o A_t} \quad (21)$$

The previous section showed that Momentum Flux 1 is a sufficient approximation of the net force on the control volume for the CFD simulations. Thus, the gross thrust force F can be approximated as the force from Momentum Flux 1, p_o is the inlet stagnation pressure, and A_t is the nozzle throat area. Figure 53 shows the thrust coefficient as a function of pressure ratio for the H₂ fuel case for all three nozzles.

The thrust coefficient for an ideal variable area ratio nozzle is included for reference. This was computed as:

$$C_F = \sqrt{\frac{2\gamma^2}{\gamma-1} \left(\frac{2}{\gamma+1} \right)^{(\gamma+1)/(\gamma-1)} \left(1 - \left(\frac{p_e}{p_o} \right)^{(\gamma-1)/\gamma} \right)} \quad (22)$$

Forces on the nozzle base are neglected because the plug is assumed to be in the open wake regime, so the pressure experienced on the base is close to ambient pressure. Forces on control surface 2 (Momentum Flux 2) are neglected, because the results of Figure 51 show that these forces are negligible compared to Momentum Flux 1. This data will be used to develop a correlation between the time-averaged aerospike pressure distribution and the effective pressure ratio “seen” by the RDE nozzle. It remains unclear why the thrust coefficient for the nozzle with a design pressure ratio of 25:1 decreases at a pressure ratio of 15:1. All other computed thrust coefficient values increase with increasing pressure ratio.

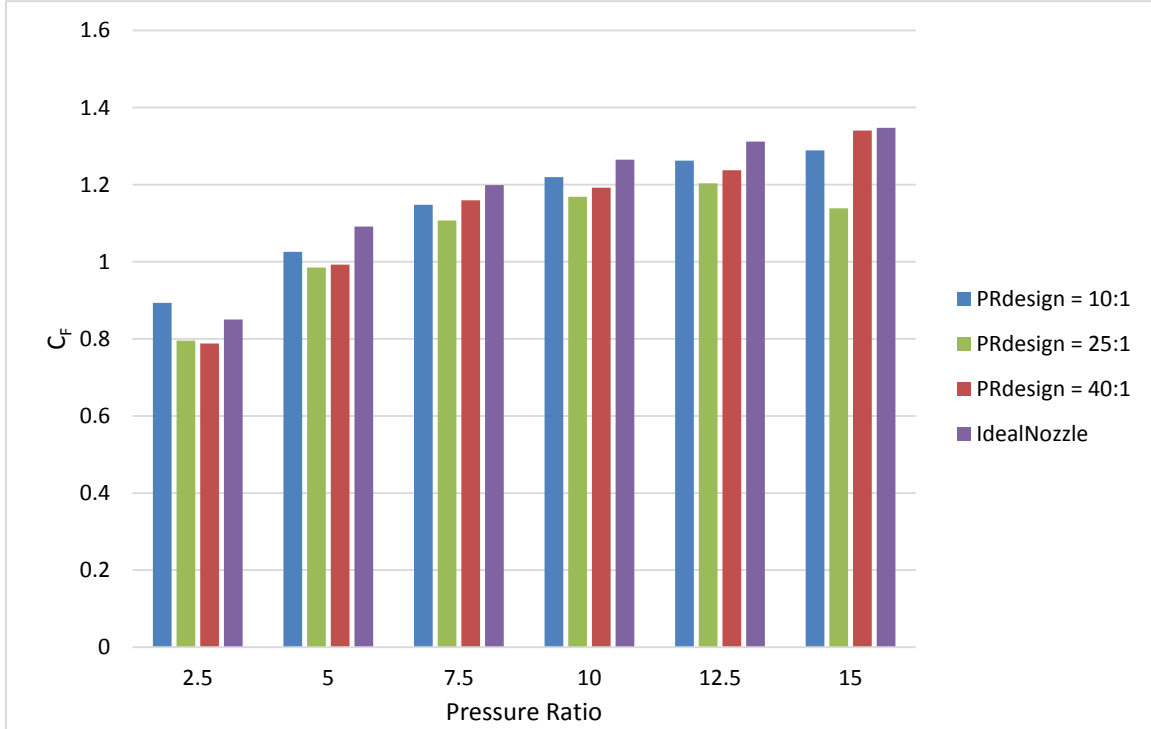


Figure 53. Thrust Coefficient vs Pressure Ratio for H₂ Fuel Case

B. SUPERSONIC FREE-STREAM

The last CFD simulation (run number 25 of Table 5) attempted to model conditions that would be experienced by an air-breathing flight vehicle utilizing an aerospike-equipped RDE for propulsion. These ANSYS simulations featured a supersonic free-stream to model expected flight conditions. The pressure ratio for this simulation was maintained at the design pressure ratio of 10:1, and the working fluid was modeled as the combustion products from combustion of hydrogen in air (see Table 3). This case allows for the determination of the qualitative effect of base bleed, which was varied from 0 to 10% of the inlet mass flux.

In order for combustion to occur at sea level at the design pressure ratio of 10:1, the incoming air must have a stagnation pressure of 10 atm. A pressure ratio of 10:1 for a γ value of 1.4 (air) corresponds to an ideal Mach number of 2.157 via the isentropic relations. Thus, the Mach number of the free-stream inlet boundary condition was set to 2.157 to match the simulation pressure ratio of 10:1. In reality, inlet losses would require a higher flight Mach number to achieve this value.

A slice view of the Mach number contours for this simulation is shown in Figure 54.

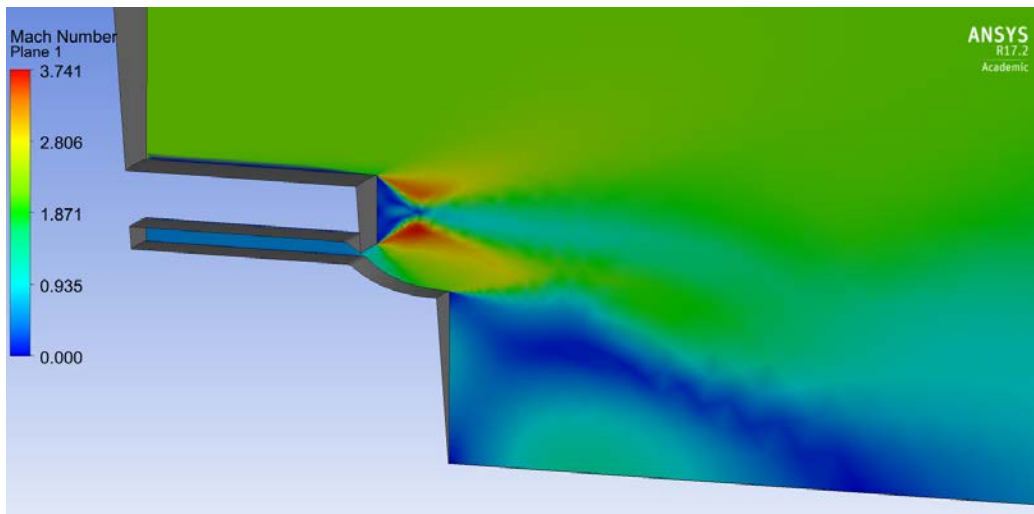


Figure 54. Plot of Mach Numbers for Supersonic Free-Stream Case, No Base Bleed

The dead air region at the shroud base, as shown in Figure 20, is clearly visible in Figure 54. This affects the Mach number distribution along the exit plane, as shown in Figure 55.

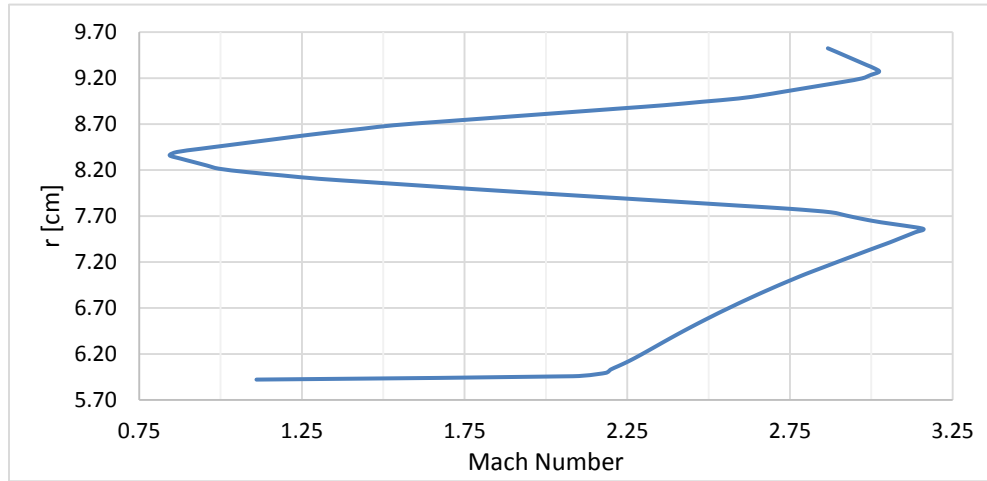


Figure 55. Mach Number Distribution along the Nozzle Exit Plane at Various Pressure Ratios for the Supersonic Free-Stream Hydrogen-Air Case

The pressure distribution along the spike, however, remains virtually unchanged from the quiescent air case, as shown in Figure 56.

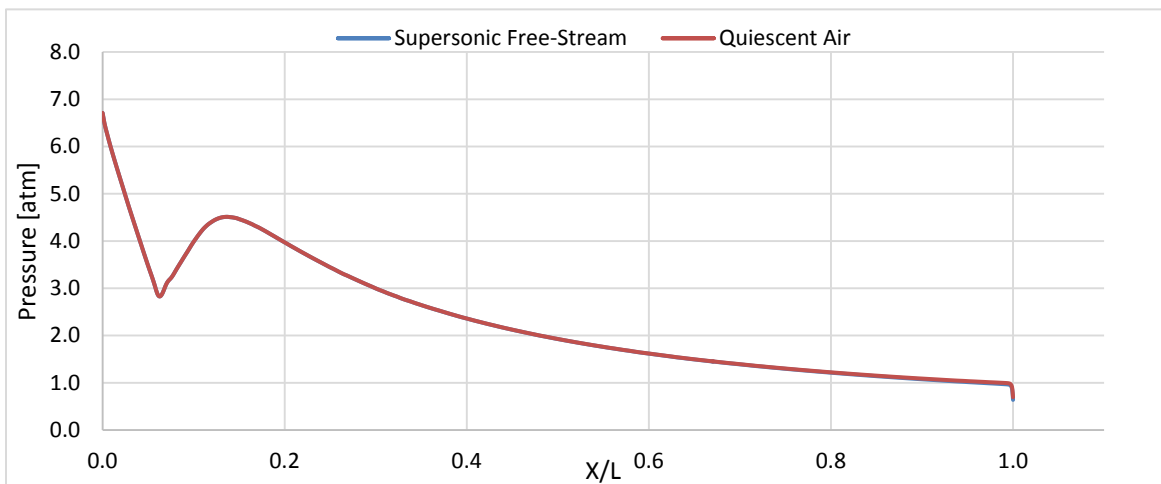


Figure 56. Steady-State Nozzle Pressure Distribution at Various Pressure Ratios for the Supersonic Free-Stream Hydrogen-Air Case, $PR_{\text{design}} = 10:1$

The effect of base bleed on the base pressure distribution is shown in Figure 57.

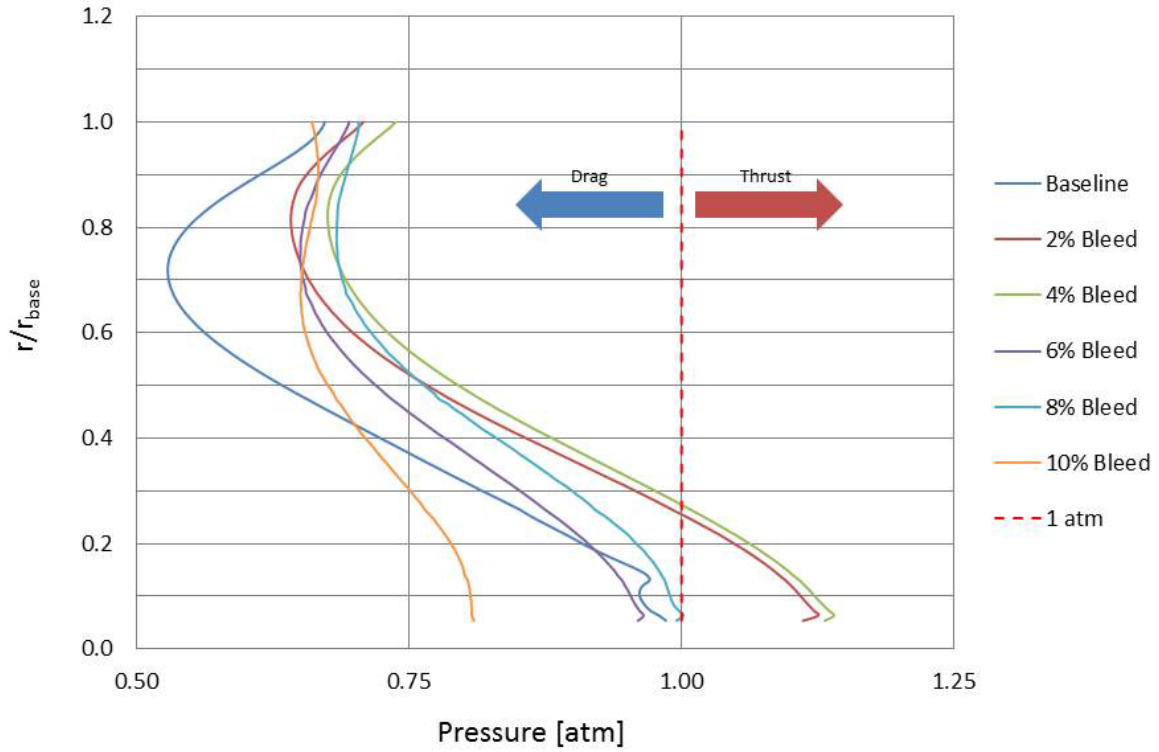


Figure 57. Effect of Base Bleed on Base Pressure Distribution, $PR_{\text{design}} = 10:1$, H_2 Fuel Case

While CFD has been shown to inadequately predict pressure in this region, Figure 57 is still valuable because it shows that there exists an optimum amount base bleed for a given aerospike nozzle in certain operating conditions. For this case, 4% base bleed produced the optimum base pressure distribution, as this amount of base bleed raised the base pressure closest to ambient.

C. MESH SENSITIVITY AND TURBULENCE MODELING

A mesh sensitivity analysis was performed to ensure that the mesh densities used were fine enough to fully resolve the important flow characteristics. The number of elements in the mesh was increased until the pressure distribution along the aerospike nozzle in the axial direction converged. Because the k-epsilon turbulence model used in the simulations is not always sufficient in supersonic flows, the SST turbulence model

was also used for one test in the sensitivity analysis to examine sensitivity of the turbulence model.

All tests were carried out for the $PR_{\text{design}} = 10:1$, quiescent air, hydrogen fuel case at a 10:1 operating pressure ratio. Figure 58 shows the results of this analysis.

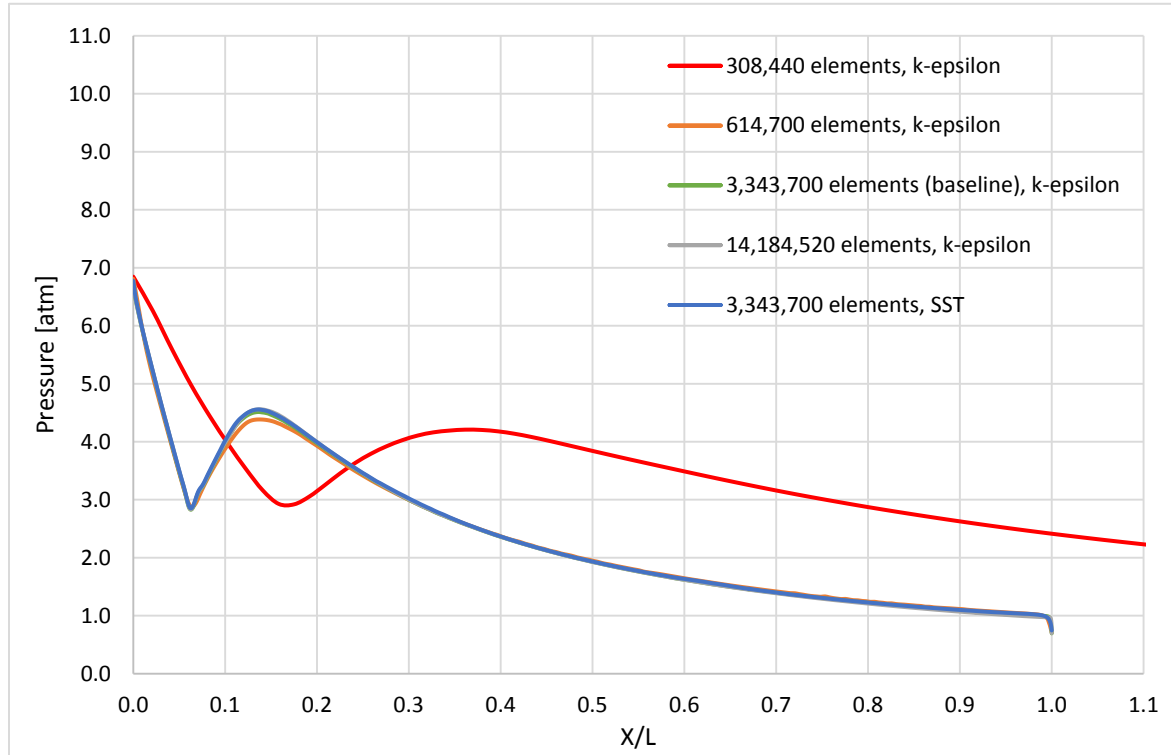


Figure 58. Mesh Sensitivity and Turbulence Model Analysis

From Figure 58, it is evident that 3,343,700 elements are sufficient for the pressure distribution along the aerospike nozzle to converge. 3,343,700 elements were used for all the $PR_{\text{design}} = 10:1$ simulations, and a comparable number of elements were used in the $PR_{\text{design}} = 25:1$ and $40:1$ cases. Further mesh refinement to 14,184,520 resulted in no difference in pressure distribution along the aerospike nozzle contour. Changing the turbulence model to SST for the baseline case of 3,343,700 elements also had virtually no effect on the distribution.

VII. SUMMARY

The high frequency operation of RDEs results in flow fields that are more apt to utilize steady-state devices, such as aerospikes nozzles, for thrust generation. This thesis developed a technique for the initial design of aerospikes nozzles for rotating detonation engines.

A. DESIGN GUIDELINES

Due to the transient nozzle entrance pressure values produced throughout the combustion cycle, it is recommended that the nozzle design pressure ratio should meet or exceed the highest expected stagnation pressure ratio across any azimuthal range at the nozzle entrance. This is expected to yield the most favorable thrust characteristics by fully capturing the altitude-compensating advantages of aerospikes nozzles in the overexpanded flow regime. Additionally, this is expected to guarantee open wake base flow, which has been shown to minimize base drag in constant altitude operation when compared to the closed wake case.

Angelino's approximate method for plug nozzle design can be used to generate the axisymmetric nozzle contour using this design pressure ratio, assuming steady flow. Although this is not an accurate assumption for RDE operation, careful selection of input parameters can produce an acceptable contour that maintains altitude-compensating characteristics within unsteady flow fields.

B. FUTURE WORK

It is unclear how effectively a steady-state CFD analysis will approximate the flow properties for an aerospikes in a spatially and temporally varying RDE flow field. Experimental testing and/or a full unsteady CFD analysis should be used to determine the thrust coefficient of an aerospikes nozzle operating on a RDE.

Future work is needed to implement the nozzle designed in this thesis. Experimental work should obtain the pressure distribution across the aerospikes contour and base during RDE operation, and compare the time-averaged values with the steady-

state computational results. Gross thrust should be calculated by integrating the pressure distribution over the aerospike contour, and a time-averaged thrust coefficient should be computed for various operating pressure ratios. Subsequently, the performance impacts of aerospike nozzles on RDEs should be characterized and used to optimize aerospike nozzle design for RDE applications.

APPENDIX A. MATLAB CODE

```

%% Angelino's Approximate Method MATLAB Code
% by Mark C. Schnabel
% This code outputs the contour for an aerospike nozzle using Angelino's method based on the isentropic area ratio
% relationship. This code accounts for the RDE geometry and a fillet radius.
%% Initialization
clc; clear all; close all
%% Inputs
% Nozzle Inputs
PR = 40; % design pressure ratio
Gamma = 1.24; % specific heat ratio
MChamber = 0.5; % Mach number desired in the chamber
% Chamber Geometry
OD = 6; % RDE outer diameter, inches
ID = 5.4; % RDE inner diameter, inches
FilletRadius = 1/8; % desired fillet radius, inches
nu_step = 0.001; % incremental Prandtl-Meyer angle
%% Calculations
% Combustion Chamber
AChamber = pi/4*(OD^2-ID^2); % cross-sectional area, in^2
% Nozzle
Mexit = sqrt((PR^((Gamma-1)/Gamma)-1)/(2*(Gamma-1))); % design exit M
nu_e = (sqrt((Gamma+1)/(Gamma-1))*atan(sqrt((Gamma-1)/(Gamma+1)*(Mexit^2-1)))-atan(sqrt(Mexit^2-1))); % P-
M function
ThetaT = nu_e; % throat angle
% Account for the fillet radius
radius_shift = FilletRadius - FilletRadius*cos(ThetaT);
rt = ID/2 - radius_shift;
% Area Ratios
EpsilonChamber = (1/MChamber)*((1+((Gamma-1)/2)*MChamber^2)/((Gamma+1)/2))^((Gamma+1)/(2*(Gamma-
1))); % subsonic area ratio
At = AChamber/EpsilonChamber; % throat area
EpsilonRequired = (1/Mexit)*((1+((Gamma-1)/2)*Mexit^2)/((Gamma+1)/2))^((Gamma+1)/(2*(Gamma-1))); %
supersonic area ratio
Ae = EpsilonRequired*At; % nozzle exit area
% Expansion Points
re = sqrt(rt^2 + At*cos(ThetaT)/pi); % radial coord. of nozzle lip
xe = 0; % axial coord. of nozzle lip
rb = sqrt(re^2-Ae/pi); % radial coord. of nozzle base
xt = (re-rb)/(tan(pi/2+ThetaT)); % axial coord. of throat point on plug contour
%% Determine the Nozzle Contour
% Initialization
r_spike = [];
x_spike = [];
Ma = 1;
nu = 0;
% Loop
while Ma < Mexit
    nu = nu + nu_step;
    theta = ThetaT - nu;
    f = @(M) nu - (sqrt((Gamma+1)/(Gamma-1))*atan(sqrt((Gamma-1)/(Gamma+1)*(M^2-1)))-atan(sqrt(M^2-1)));
    Ma = bisection(f,1,Mexit+1); % method of bisection to get the local Mach number
    mu = asin(1/Ma);
    AreaRatio = (1/Ma)*((1+((Gamma-1)/2)*Ma^2)/((Gamma+1)/2))^((Gamma+1)/(2*(Gamma-1)));
    r_next = sqrt(re^2-(re^2-rb^2)*AreaRatio*sin(mu+theta)/(sin(mu)*cos(ThetaT)));
    x_next = (re-r_next)/tan(mu+theta);
    r_spike = [r_spike;r_next];

```

```

    x_spike = [x_spike;x_next];
end
%% Connect the contour to the throat
xconnect = (linspace(xt,x_spike(1),20))';
rconnect = (linspace(rt,r_spike(1),20))';
r_spike = [rconnect;r_spike];
x_spike = [xconnect;x_spike];
%% Sweep out the fillet radius
theta_sweep = (pi/2-ThetaT):0.01:(pi/2);
xc = xt-FilletRadius*sin(ThetaT);
rc = rt-FilletRadius*cos(ThetaT);
fillet_xvals = FilletRadius.*cos(theta_sweep)+xc;
fillet_xvals=flipud(fillet_xvals');
fillet_rvals = FilletRadius.*sin(theta_sweep)+rc;
fillet_rvals=flipud(fillet_rvals');
%% Extend backward by the fillet radius
xq=(linspace((fillet_xvals(1)-1/8),fillet_xvals(1),10))';
rq=ID/2.*ones(length(xq),1);
%% Connect to meet the center body
xs=(linspace((xq(1)-7/10),xq(1),10))';
rs=ID/2.*ones(length(xs),1);
%% Generate the cowl
% Section 1: tangent to the throat
x1=xe;r1=re;
r2=OD/2;
m=-tan(ThetaT);
b=r1-m*x1;
x2=(r2-b)/m;
xtan=(linspace(x2,x1,20))';
rtan=m.*xtan+b;
% Section 2: parallel to the outer ring
xp=(linspace(xq(1),xtan(1),10))';
rp=OD/2.*ones(length(xp),1);
% Section 3: fillet radius
m1=(rtan(1)-rtan(end))/(xtan(1)-xtan(end));
m2=-1/m1;
yc=OD/2-FilletRadius;
thetafill=atan(m2);
y2=yc+FilletRadius*sin(thetafill);
x2=(y2-b)/m1;
xc=x2-FilletRadius*cos(thetafill);
thetasweep=thetafill:0.01:pi/2;
xcowlsweep=FilletRadius.*cos(thetasweep)+xc;
xcowlsweep=flipud(xcowlsweep');
rcowlsweep=FilletRadius.*sin(thetasweep)+yc;
rcowlsweep=flipud(rcowlsweep');
% Compile
xc1=linspace(xp(1),xcowlsweep(1),10)'; xc2=xcowlsweep; xc3=linspace(xcowlsweep(end),xtan(end),10)';
rc1=linspace(rp(1),rcowlsweep(1),10)'; rc2=rcowlsweep; rc3=linspace(rcowlsweep(end),rtan(end),10)';
xcowl=[xc1;xc2;xc3];
rcowl=[rc1;rc2;rc3];
%% Verify the throat location and throat area
areas=[];
angles=[];
for i=1:length(fillet_xvals)
    for j=1:length(xtan)
        x1=xtan(j); r1=rtan(j);
        x2=fillet_xvals(i); r2=fillet_rvals(i);
        theta=abs(atan((x2-x1)/(r2-r1)));
        A=pi*abs(r1^2-r2^2)/cos(theta);
        areas=[areas;i,j,A];
    end
end

```

```

        angles=[angles;i,j,theta];
    end
end
% Find smallest
index = min(areas(:,3));
index = find(areas(:,3)==index);
fprintf('Throat point 1 (on plug contour): x1=%1.3f in., r1=%1.3f in. \n',
    fillet_xvals(areas(index,1)),fillet_rvals(areas(index,1)))
fprintf('Throat point 2 (at nozzle lip): x2=%1.3f in., r2=%1.3f in. \n', xtan(areas(index,2)),rtan(areas(index,2)))
fprintf('Throat area: %1.4f in^2. \n',areas(index,3))
fprintf('Throat angle: %1.4f rads. \n',angles(index,3))
%% Export the Contour
% Compile Fillet Contour
fillet_xvals=fillet_xvals(1:6:end,:); % save only every 6th point
fillet_rvals=fillet_rvals(1:6:end,:); % save only every 6th point
fillet_xvals=fillet_xvals(1:end-1); % remove the last point (close to the throat point)
fillet_rvals=fillet_rvals(1:end-1); % remove the last point (close to the throat point)
% Compile Nozzle Contour
x_spike=x_spike(1:5:end,:); % save only every 5th point
r_spike=r_spike(1:5:end,:); % save only every 5th point
% Combine Both Contours
xnozzle=[fillet_xvals;x_spike];
rnozzle=[fillet_rvals;r_spike];
% Shift
x_shift=xnozzle(1);
xnozzle=xnozzle-x_shift;
% Save
AngelinoContour=[xnozzle,rnozzle];
AngelinoContour=unique(AngelinoContour,'rows'); % eliminate duplicate rows
% Plot
figure(1)
hold on
title('Aerospike Contour')
xlabel('Axial Coordinate, x [inches]')
ylabel('Radial Coordinate, r [inches]')
plot(AngelinoContour(:,1),AngelinoContour(:,2),'k','LineWidth',3) % aerospike contour
axis equal
hold off
% Export
xlswrite('AngelinoContour.xlsx',AngelinoContour)
%% Export the Cowl
% Compile the Cowl Contour
xcowl=xcowl-x_shift;
AngelinoCowl=[xcowl,rcowl];
AngelinoCowl=unique(AngelinoCowl,'rows'); % eliminate duplicate rows
% Plot
figure(2)
hold on
title('Cowl Contour')
xlabel('Axial Coordinate, x [inches]')
ylabel('Radial Coordinate, r [inches]')
plot(AngelinoCowl(:,1),AngelinoCowl(:,2),'k','LineWidth',3) % cowl contour
plot(xcowlsweep-x_shift,rcowlsweep,'k.')
axis equal
hold off
% Export
xlswrite('AngelinoCowl.xlsx',AngelinoCowl)
%% Combined Image
figure(3)
hold on
title('PRdes 40:1')

```

```

xlabel('Axial Coordinate, x [in]')
ylabel('Radial Coordinate, r [in]')
plot(AngelinoContour(:,1),AngelinoContour(:,2),'k','LineWidth',3) % aerospike contour
plot([AngelinoCowl(1,1),AngelinoContour(1,1)], [AngelinoContour(1,2),AngelinoContour(1,2)], 'k','LineWidth',3) %
complete the aerospike contour
plot([AngelinoContour(end,1),AngelinoContour(end,1)], [0,AngelinoContour(end,2)], 'k','LineWidth',3) % base
plot(AngelinoCowl(:,1),AngelinoCowl(:,2),'k','LineWidth',3) % cowl contour
plot([(xe-x_shift),(xt-x_shift)], [re,rt], 'r','LineWidth',3) % throat
plot(AngelinoContour(:,1),0.*AngelinoContour(:,2),'b--','LineWidth',3) % centerline
axis equal
hold off

```

```

function p = bisection(f,a,b)
% method of bisection
if f(a)*f(b)>0
    disp('Wrong choice bro')
else
    p = (a + b)/2;
    err = abs(f(p));
    while err > 1e-7
        if f(a)*f(p)<0
            b = p;
        else
            a = p;
        end
        p = (a + b)/2;
        err = abs(f(p));
    end
end

```


APPENDIX B. CEA DETONATION ANALYSIS

NASA-GLENN CHEMICAL EQUILIBRIUM PROGRAM CEA2, MAY 21, 2004
 BY BONNIE MCBRIDE AND SANFORD GORDON
 REFS: NASA RP-1311, PART I, 1994 AND NASA RP-1311, PART II, 1996

```

prob
phi,eq.ratio=0.4 det t,k=1205 p,atm=1
react
  oxid=Air wt=40 t,k=300
  fuel=C2H4 wt=100 t,k=300
  oxid=CO2 wt=4.8 t,k=1808
  oxid=H2O wt=4.8 t,k=1808
  oxid=O2 wt=4.7 t,k=1808
  oxid=N2 wt=45.6 t,k=1808
output
  siunits short
end
  
```

DETONATION PROPERTIES OF AN IDEAL REACTING GAS

CASE =

REACTANT	WT FRACTION (SEE NOTE)	ENERGY KJ/KG-MOL	TEMP K
OXIDANT Air	0.4004004	-71.689	300.000
FUEL C2H4	1.0000000	52579.505	300.000
OXIDANT CO2	0.0480480	-313599.987	1808.000
OXIDANT H2O	0.0480480	-178578.227	1808.000
OXIDANT O2	0.0470470	51991.211	1808.000
OXIDANT N2	0.4564565	49262.657	1808.000

O/F= 61.23479 %FUEL= 1.606818 R,EQ.RATIO= 0.614522 PHI,EQ.RATIO= 0.400000

UNBURNED GAS

P1, BAR 1.0132
 T1, K 1205.00
 H1, KJ/KG 35.74

M1, (1/n) 28.287
GAMMA1 1.2951
SON VEL1,M/SEC 677.3

BURNED GAS

P, BAR 2.6304
T, K 2089.86
RHO, KG/CU M 4.2781-1
H, KJ/KG 507.37
U, KJ/KG -107.47
G, KJ/KG -18647.8
S, KJ/(KG)(K) 9.1658

M, (1/n) 28.261
(dLV/dLP)t -1.00033
(dLV/dLT)p 1.0109
Cp, KJ/(KG)(K) 1.5458
GAMMA_s 1.2409
SON VEL,M/SEC 873.5

DETONATION PARAMETERS

P/P1 2.596
T/T1 1.734
M/M1 0.9991
RHO/RHO1 1.4954
DET MACH NUMBER 1.9286
DET VEL,M/SEC 1306.2

MOLE FRACTIONS

*Ar 0.00360
*CO 0.00039
*CO2 0.06246
*H 0.00002
*H2 0.00014
H2O 0.10532
*NO 0.00546
NO2 0.00001
*N2 0.75051
*O 0.00021
*OH 0.00215
*O2 0.06973

* THERMODYNAMIC PROPERTIES FITTED TO 20000.K

NOTE. WEIGHT FRACTION OF FUEL IN TOTAL FUELS AND OF OXIDANT IN
TOTAL OXIDANTS

THIS PAGE INTENTIONALLY LEFT BLANK

APPENDIX C. TRANSITION PRESSURE RATIO ANALYSIS

PRdesign	Based on Nozzle Geometry							Transition Pressure Ratio Iteration								% Error
	γ	ϕ (rad)	CE/BC	β (rad)	$\Delta\beta$ (deg)	$\Delta\beta$ (rad)	β' (rad)	Guess PRtr	Mtr	$\mu(\text{Mtr},\gamma)$	$\nu(\text{Mtr},\gamma)$	Me	$\nu(\text{Me},\gamma)$	δ (rad)	β' (rad)	
10	1.24	0.0	2.650	0.361	5.0	0.087	0.274	25	2.684	0.382	0.381	2.163	-0.158	0.623	0.465	69.845
10	1.24	0.0	2.650	0.361	5.0	0.087	0.274	26	2.706	0.379	0.405	2.163	-0.158	0.623	0.438	59.963
10	1.24	0.0	2.650	0.361	5.0	0.087	0.274	27	2.727	0.375	0.428	2.163	-0.158	0.623	0.412	50.484
10	1.24	0.0	2.650	0.361	5.0	0.087	0.274	28	2.748	0.373	0.450	2.163	-0.158	0.623	0.387	41.379
10	1.24	0.0	2.650	0.361	5.0	0.087	0.274	29	2.767	0.370	0.471	2.163	-0.158	0.623	0.363	32.623
10	1.24	0.0	2.650	0.361	5.0	0.087	0.274	30	2.786	0.367	0.492	2.163	-0.158	0.623	0.340	24.192
10	1.24	0.0	2.650	0.361	5.0	0.087	0.274	31	2.804	0.365	0.511	2.163	-0.158	0.623	0.318	16.065
10	1.24	0.0	2.650	0.361	5.0	0.087	0.274	32	2.822	0.362	0.530	2.163	-0.158	0.623	0.296	8.223
10	1.24	0.0	2.650	0.361	5.0	0.087	0.274	33	2.839	0.360	0.549	2.163	-0.158	0.623	0.275	0.649
10	1.24	0.0	2.650	0.361	5.0	0.087	0.274	34	2.856	0.358	0.567	2.163	-0.158	0.623	0.255	6.674
10	1.24	0.0	2.650	0.361	5.0	0.087	0.274	35	2.872	0.356	0.584	2.163	-0.158	0.623	0.236	13.760
25	1.24	0.0	2.650	0.361	5.0	0.087	0.274	70	3.261	0.312	0.980	2.684	0.381	0.623	0.336	22.689
25	1.24	0.0	2.650	0.361	5.0	0.087	0.274	71	3.268	0.311	0.988	2.684	0.381	0.623	0.327	19.591
25	1.24	0.0	2.650	0.361	5.0	0.087	0.274	72	3.276	0.310	0.995	2.684	0.381	0.623	0.319	16.544
25	1.24	0.0	2.650	0.361	5.0	0.087	0.274	73	3.284	0.309	1.003	2.684	0.381	0.623	0.311	13.547
25	1.24	0.0	2.650	0.361	5.0	0.087	0.274	74	3.292	0.309	1.010	2.684	0.381	0.623	0.303	10.599
25	1.24	0.0	2.650	0.361	5.0	0.087	0.274	75	3.299	0.308	1.017	2.684	0.381	0.623	0.295	7.698
25	1.24	0.0	2.650	0.361	5.0	0.087	0.274	76	3.307	0.307	1.024	2.684	0.381	0.623	0.287	4.842
25	1.24	0.0	2.650	0.361	5.0	0.087	0.274	77	3.314	0.307	1.031	2.684	0.381	0.623	0.279	2.032
25	1.24	0.0	2.650	0.361	5.0	0.087	0.274	78	3.321	0.306	1.038	2.684	0.381	0.623	0.272	0.736
25	1.24	0.0	2.650	0.361	5.0	0.087	0.274	79	3.329	0.305	1.045	2.684	0.381	0.623	0.264	3.461
25	1.24	0.0	2.650	0.361	5.0	0.087	0.274	80	3.336	0.304	1.052	2.684	0.381	0.623	0.257	6.145
40	1.24	0.0	2.650	0.361	5.0	0.087	0.274	125	3.589	0.282	1.278	2.947	0.663	0.623	0.290	5.956
40	1.24	0.0	2.650	0.361	5.0	0.087	0.274	126	3.594	0.282	1.282	2.947	0.663	0.623	0.286	4.413
40	1.24	0.0	2.650	0.361	5.0	0.087	0.274	127	3.598	0.282	1.286	2.947	0.663	0.623	0.281	2.885
40	1.24	0.0	2.650	0.361	5.0	0.087	0.274	128	3.603	0.281	1.289	2.947	0.663	0.623	0.277	1.372
40	1.24	0.0	2.650	0.361	5.0	0.087	0.274	129	3.607	0.281	1.293	2.947	0.663	0.623	0.273	0.127
40	1.24	0.0	2.650	0.361	5.0	0.087	0.274	130	3.612	0.281	1.297	2.947	0.663	0.623	0.269	1.612
40	1.24	0.0	2.650	0.361	5.0	0.087	0.274	131	3.616	0.280	1.301	2.947	0.663	0.623	0.265	3.082
40	1.24	0.0	2.650	0.361	5.0	0.087	0.274	132	3.621	0.280	1.304	2.947	0.663	0.623	0.261	4.539
40	1.24	0.0	2.650	0.361	5.0	0.087	0.274	133	3.625	0.280	1.308	2.947	0.663	0.623	0.257	5.983
40	1.24	0.0	2.650	0.361	5.0	0.087	0.274	134	3.629	0.279	1.311	2.947	0.663	0.623	0.253	7.413
40	1.24	0.0	2.650	0.361	5.0	0.087	0.274	135	3.633	0.279	1.315	2.947	0.663	0.623	0.249	8.830

THIS PAGE INTENTIONALLY LEFT BLANK

APPENDIX D. CEA DEFLAGRATION ANALYSIS

NASA-GLENN CHEMICAL EQUILIBRIUM PROGRAM CEA2, MAY 21, 2004
 BY BONNIE MCBRIDE AND SANFORD GORDON
 REFS: NASA RP-1311, PART I, 1994 AND NASA RP-1311, PART II, 1996

```

prob
phi,eq.ratio=0.1,0.2,0.3,0.4,0.5,0.6,0.7,0.8,0.9,1 rocket equilibrium tcest,k=38
00 p,atm=9.88
react
  fuel=H2 wt=100 t,k=300
  oxid=Air wt=100 t,k=300
output
  siunits massf short
end
  
```

THEORETICAL ROCKET PERFORMANCE ASSUMING EQUILIBRIUM

COMPOSITION DURING EXPANSION FROM INFINITE AREA
 COMBUSTOR

Pin = 145.2 PSIA
 CASE =

REACTANT	WT FRACTION (SEE NOTE)	ENERGY KJ/KG-MOL	TEMP K
FUEL H2	1.000000	53.359	300.000
OXIDANT Air	1.000000	-71.689	300.000

O/F= 34.29623 %FUEL= 2.833164 R, EQ.RATIO= 1.000000 PHI, EQ.RATIO= 1.000000

CHAMBER THROAT

Pinf/P	1.0000	1.7822
P, BAR	10.011	5.6172
T, K	2439.83	2216.83
RHO, KG/CU M	1.2087	0.74881-1
H, KJ/KG	-1.6550	-457.57
U, KJ/KG	-829.91	-1207.72

G, KJ/KG -25008.9 -23179.1
 S, KJ/(KG)(K) 10.2496 10.2496

M, (1/n) 24.492 24.571
 (dLV/dLP)_t -1.00215 -1.00104
 (dLV/dLT)_p 1.0572 1.0303
 Cp, KJ/(KG)(K) 2.2601 2.0142
 GAMMA_s 1.1986 1.2155
 SON VEL,M/SEC 996.4 954.9
 MACH NUMBER 0.000 1.000

PERFORMANCE PARAMETERS

Ae/At 1.0000
 CSTAR, M/SEC 1400.1
 CF 0.6820
 Ivac, M/SEC 1740.5
 Isp, M/SEC 954.9

MASS FRACTIONS

*Ar 0.01255 0.01255
 *CO 0.00004 0.00002
 *CO₂ 0.00040 0.00044
 *H 0.00002 0.00001
 *H₂ 0.00076 0.00039
 H₂O 0.24456 0.24886
 *NO 0.00250 0.00119
 *N₂ 0.73262 0.73323
 *O 0.00011 0.00003
 *OH 0.00311 0.00142
 *O₂ 0.00331 0.00186

* THERMODYNAMIC PROPERTIES FITTED TO 20000.K

NOTE. WEIGHT FRACTION OF FUEL IN TOTAL FUELS AND OF OXIDANT IN TOTAL OXIDANTS

NASA-GLENN CHEMICAL EQUILIBRIUM PROGRAM CEA2, MAY 21, 2004
 BY BONNIE MCBRIDE AND SANFORD GORDON
 REFS: NASA RP-1311, PART I, 1994 AND NASA RP-1311, PART II, 1996

```

prob
phi,eq.ratio=1 rocket equilibrium tcest,k=38
00 p,atm=10
react
  fuel=C2H4 wt=100 t,k=300
  oxid=Air wt=100 t,k=300
output
  siunits short
end
  
```

THEORETICAL ROCKET PERFORMANCE ASSUMING EQUILIBRIUM

COMPOSITION DURING EXPANSION FROM INFINITE AREA
 COMBUSTOR

Pin = 147.0 PSIA
 CASE =

REACTANT		WT FRACTION (SEE NOTE)	ENERGY KJ/KG-MOL	TEMP K
FUEL	C2H4	1.000000	52579.505	300.000
OXIDANT	Air	1.000000	-71.689	300.000

O/F= 14.78701 %FUEL= 6.334320 R, EQ.RATIO= 1.000000 PHI, EQ.RATIO= 1.000000

CHAMBER THROAT

Pinf/P	1.0000	1.7744
P, BAR	10.133	5.7102
T, K	2440.96	2233.26
RHO, KG/CU M	1.4301	0.8471-1
H, KJ/KG	116.40	-271.76
U, KJ/KG	-592.11	-917.20
G, KJ/KG	-21742.5	-20270.7
S, KJ/(KG)(K)	8.9551	8.9551

M, (1/n)	28.645	28.769
(dLV/dLP)t	-1.00288	-1.00153
(dLV/dLT)p	1.0801	1.0466
Cp, KJ/(KG)(K)	2.1169	1.8608
GAMMA _s	1.1864	1.2028
SON VEL,M/SEC	916.8	881.1
MACH NUMBER	0.000	1.000

PERFORMANCE PARAMETERS

Ae/At	1.0000
CSTAR, M/SEC	1299.8
CF	0.6779
Ivac, M/SEC	1613.6
Isp, M/SEC	881.1

MOLE FRACTIONS

*Ar	0.00867	0.00871
*CO	0.01331	0.00707
*CO ₂	0.11635	0.12315
*H	0.00030	0.00010
*H ₂	0.00238	0.00136
H ₂ O	0.12517	0.12770
*NO	0.00317	0.00156
*N ₂	0.72171	0.72564
*O	0.00025	0.00008
*OH	0.00332	0.00161
*O ₂	0.00538	0.00302

* THERMODYNAMIC PROPERTIES FITTED TO 20000.K

NOTE. WEIGHT FRACTION OF FUEL IN TOTAL FUELS AND OF OXIDANT IN TOTAL OXIDANTS

LIST OF REFERENCES

- [1] P. J. Ellsworth, "Performance testing of a low-loss high performance lobed-injector for rotating detonation engines," M.S. thesis, Dept. Mech. Eng., Naval Postgraduate School, Monterey, CA, 2016.
- [2] D. A. Schwer and K. Kailasanath, "Rotating detonation-wave engines," NRL, 2011 Naval Research Laboratory Review, Washington DC, 2011, pp. 88–94.
- [3] K. Kailasanath, "The rotating-detonation-wave engine concept: A brief status report," in *49th AIAA Aerospace Sciences Meeting including the New Horizons Forum and Aerospace Exposition*, Orlando, FL, 2011, pp. 1–8.
- [4] J. D. Giesemann, "Computational study of low-loss non-premixed injection manifolds for rotating detonation engines," M.S. thesis, Dept. Mech. Eng., Naval Postgraduate School, Monterey, CA, 2014.
- [5] K. Kailasanath, "Research on pulse detonation combustion systems—A status report," in *47th AIAA Aerospace Sciences Meeting Including the New Horizons Forum and Aerospace Exposition*, Orlando, FL, 2009.
- [6] A. D. Chaves, "Effect of combustion chamber length and annulus width on rotating detonation wave combustor operation and performance," M.S. thesis, Dept. Mech. Eng., Naval Postgraduate School, Monterey, CA, 2014.
- [7] C. A. Khol, "Characterization of detonation wave structure in an optically accessible rotational detonation engine," M.S. thesis, Dept. Mech. Eng., Naval Postgraduate School, Monterey, CA, 2015.
- [8] J. Crane, "Characterization of ignition and stability of an optically accessible rotational detonation engine," M.S. thesis, Dept. Mech. Eng., Naval Postgraduate School, Monterey, CA, 2012.
- [9] L. H. Thomason, "Performance measurement of a rotating detonation engine," M.S. thesis, Dept. Mech. Eng., Naval Postgraduate School, Monterey, CA, 2013.
- [10] G. P. Sutton, *Rocket Propulsion Elements*, 8th ed. Hoboken, NJ: John Wiley & Sons, 2010, pp. 33,35,75,76,79,84.
- [11] P. G. Hill and C. R. Peterson, *Mechanics and Thermodynamics of Propulsion*, 2nd ed. Reading, MA: Addison-Wesley, 1992, pp. 145,146, 521.
- [12] T. Benson. (2015, October 22). Nozzle Design. [Online]. Available: <https://spaceflightsystems.grc.nasa.gov/education/rocket/nozzle.html>

- [13] G. V. R. Rao, "Exhaust nozzle contour for optimum thrust," *Journal of Jet Propulsion*, vol. 28, no. 6, pp. 377-382, 1968.
- [14] R. A. O'Leary and J. E. Beck. (1992). Nozzle Design. *Pratt & Whitney Rocketdyne's Engineering Journal of Power Technology*, 1992. [Online]. Available: http://www.k-makris.gr/RocketTechnology/Nozzle_Design/Pics/nozzle4.jpg. Accessed: March 27, 2017.
- [15] W. J. Bannink, E. M. Houtman, and M. M. J. Schoones, "On the interaction between a linear plug nozzle exhaust flow and supersonic external flow," in *Third European Symposium on Aerodynamics for Space Vehicles*, Noordwijk, The Netherlands, 1998.
- [16] T. J. Mueller and W. P. Sule, "Base Flow Characteristics of a Linear Aerospoke Nozzle Segment," *J. of Engineering for Industry*, 1973.
- [17] M. Nazarinia, A. Naghib-Lahouti, and E. Tolouei, "Design and numerical analysis of aerospoke nozzles with different plug shapes to compare their performance with a conventional nozzle," in *Eleventh Australian International Aerospace Congress*, Melbourne, Australia, 2005.
- [18] C. Thomas. (2004, April 16). A closeup of one of the Cesaroni Technology, Inc.—constructed aerospoke nozzles used in the Dryden Aerospoke Rocket Test. [Online]. Available: https://www.dfrc.nasa.gov/Gallery/Photo/Aerospoke_Rocket/HTML/EC04-0113-146.html
- [19] "Linear aerospoke engine—propulsion for the X-33 vehicle," NASA, Huntsville, AL, Fact Sheet FS-2000-09-174-MSFC, 2000.
- [20] K. Berman and F. W. Crimp, "Performance of plug-type rocket exhaust nozzles," *ARS J.*, pp. 18-23, Jan. 1961.
- [21] M. Onofri, "Plug nozzles: summary of flow features and engine performance," in *40th AIAA Aerospace Sciences Meeting*, Reno, NV, 2002.
- [22] E. Besnard, H. H. Chen, and T. Mueller, "Design, manufacturing, and test of a plug nozzle rocket engine," in *38th AIAA/ASME/SAE/ASEE Joint Propulsion Conference & Exhibit, Joint Propulsion Conferences*, Indianapolis, IN, 2002.
- [23] J. E. Jackson, E. Espenschied, and J. Klop, "The Control System for the X-33 Linear Aerospoke Engine," NASA, Huntsville, AL, Tech. Rep. CR-1998-207923, Jan. 1998.
- [24] M. Easter. (2015, October 21). It Really is Rocket Science: Firefly Space System designs rocket with Stampede supercomputer. [Online]. Available: <https://www.tacc.utexas.edu/firefly/>

- [25] E. D. Flinn, "Aerospike Engine Powers RLV Savings," *Aerospace America*, vol. 34, no. 11, pp. 18-19, Nov. 1996.
- [26] (2010, July 17). *Twin Linear Aerospike XRS-2200 Engine*. [Online]. Available: https://en.wikipedia.org/wiki/File:Twin_Linear_Aerospike_XRS-2200_Engine.jpg
- [27] F. Nasuti and M. Onofri, "Prediction of open and closed wake in plug nozzles," in *Proceedings of the 4th European Symposium on Aerothermodynamics for Space Applications*, Capua, 2002, pp. 585-592.
- [28] G. Angelino, "Approximate method for plug nozzle design," *AIAA J.*, vol. 2, no. 10, 1964.
- [29] G. Hagemann, I. Immich, T. Van Nguyen, and G. E. Dumnov, "Advanced rocket nozzles," *J. of Propulsion and Power*, vol. 14, no. 5, pp. 620-634, 1998.
- [30] C. Wang, Y. Liu, and L. Qin, "Aerospike nozzle contour design and its performance validation," *Acta Astronautica*, vol. 64, no. 11, pp. 1264-1275, 2009.
- [31] A. Martinez, "Interim report aerodynamic nozzle study: volume 2," NASA, Huntsville, AL, Tech. Rep. CR-68910, 1965.
- [32] R. Silver, "Final report: advanced aerodynamic spike configurations: analytical and cold flow studies," Rockwell International Corporation, Tech. Rep. AFRPL-TR-67-246, 1971.
- [33] K. Chutkey, B. Vasudevan, and N. Balakrishnan, "Flowfield analysis of linear plug nozzle," *J. of Spacecraft and Rockets*, vol. 49, no. 6, pp. 1109-1119, 2012.
- [34] K. Chutkey, B. Vasudevan, and N. Balakrishnan, "Analysis of annular plug nozzle flowfield," *J. of Spacecraft and Rockets*, vol. 51, no. 2, pp. 478-490, 2014.
- [35] K. Chutkey, B. Vasudevan, and N. Balakrishnan, "Flow and performance analysis of annular cluster truncated plug nozzle," *J. of Propulsion and Power*, vol. 32, no. 6, pp. 1442-1453, 2016.
- [36] J. Ruf and P. McConnaughey, "The plume physics behind aerospike nozzle altitude compensation and slipstream effect," in *33rd Joint Propulsion Conference and Exhibit*, Seattle, WA, 1997.
- [37] F. Nasuti and M. Onofri, "Theoretical analysis and engineering modeling of flowfields in clustered module plug nozzles," *J. of Propulsion and Power*, vol. 15, no. 4, pp. 544-551, 1999.

- [38] T. Ito, K. Fujii, and A. K. Hayashi, "Computations of the axisymmetric plug nozzle flowfields: flow structures and thrust performance," *J. of Propulsion and Power*, vol. 18, no. 2, pp. 254–260, 2002.
- [39] D. M. Davidenko, Y. Eude, and F. Falempin, "Optimization of supersonic axisymmetric nozzles with a center body for aerospace propulsion," *Progress in Propulsion Physics*, vol. 2, pp. 675-692, 2011.
- [40] G. Hagemann and H. Immich, "Critical assessment of the linear plug nozzle concept," in *37th Joint Propulsion Conference and Exhibit*, Salt Lake City, UT, 2001.
- [41] T. Tomita, H. Tamura, M. Takahashi, "An experimental evaluation of plug nozzle flow field," in *AIAA, ASME, SAE, and ASEE, Joint Propulsion Conference and Exhibit*, Lake Buena Vista, FL, 1996.
- [42] A. H. Shapiro, *The Dynamics and Thermodynamics of Compressible Fluid Flow*, vol. 1 and 2, pp. 294-295, 694-695.
- [43] B. L. Denton, "Design and analysis of rocket nozzle contours for launching Pico-Satellites," M.S. thesis, Rochester Institute of Technology, Rochester, NY, 2008.
- [44] L. V. Kumar and K. S. Reddy, "Design and flow simulation of truncated aerospike nozzle," *International J. of Research in Engineering and Technology*, vol. 3, no. 11, pp. 122-131, Nov. 2014.
- [45] D. J. Choudhari and U. V. Asolekar, "Efficiency analysis of an aerospike nozzle," *International J. of Engineering Research and Applications*, ISSN: 2248-9622, pp. 146-150, 2012.
- [46] J. J. Korte, "Parametric model of an aerospike rocket engine," in *38th Aerospace Sciences Meeting & Exhibit*, Reno, NV, 2000.
- [47] T. Tomita, M. Takahashi, and H. Tamura, "Flow field of clustered plug nozzles," AIAA paper 97-3219, 1997.
- [48] H. Immich and M. Caporicci, "Status of the FESTIP rocket propulsion technology program," in *33rd Joint Propulsion Conference and Exhibit*, Seattle, WA, 1997.
- [49] D. A. Schwer and K. Kailasanath, "Numerical investigation of rotating detonation engines," in *46th AIAA/ASME/SAE/ASEE Joint Propulsion Conference & Exhibit*, Nashville, TN, 2010, pp. 1–15.
- [50] S. Gordon, and B. J. McBride. (1996). *Computer Program for Calculation of Complex Chemical Equilibrium Compositions and Applications*. [Online]. Available: <https://www.grc.nasa.gov/www/CEAWeb/>. Accessed May 26, 2017.

INITIAL DISTRIBUTION LIST

1. Defense Technical Information Center
Ft. Belvoir, Virginia
2. Dudley Knox Library
Naval Postgraduate School
Monterey, California